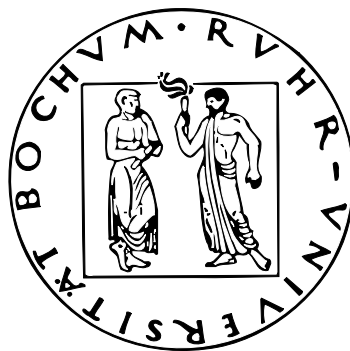


INVESTIGATION
OF THE
DWARF GALAXY POPULATION IN
HICKSON COMPACT GROUPS



Dissertation
zur
Erlangung des Grades
“Doktor der Naturwissenschaften”
der Fakultät für Physik und Astronomie
an der Ruhr–Universität Bochum

vorgelegt von
Elvira Krusch
Bochum, Oktober 2003

Erster Gutachter: Prof. Dr. Ralf-Jürgen Dettmar (Institut für Astronomie, AIRUB)
Zweiter Gutachter: HD Dr. Susanne Hüttemeister (Institut für Astronomie, AIRUB)

Contents

1	Introduction	1
1.1	Compact Groups of Galaxies	1
1.1.1	Definition of Compact Groups	2
1.1.2	Nature of Compact Groups	4
1.2	Dwarf galaxies and their environment	9
1.2.1	Classification of Dwarf Galaxies	9
1.2.2	Dwarf galaxies in Hickson Compact Groups	11
2	Data and data reduction	15
2.1	The HCG sample	15
2.2	The data	15
2.2.1	The Wide Field Imager observations	16
2.2.2	Filter characteristics	17
2.3	Reduction of the mosaic data	19
2.3.1	Bias correction	21
2.3.2	Flat field correction	23
2.3.3	Sky subtraction on each CCD-image	24
2.3.4	Coordinate calibration	27
2.3.5	Creating individual images	30
2.3.6	Adjusting intensity scales	30
2.3.7	Final mosaic image	31
2.4	Photometry	32
2.5	Detection of dwarf galaxies	39
2.5.1	The Source Extractor program	39
2.5.2	Selection criteria	41
2.5.3	Radial light profiles and isophotal fits	43
3	Analysis and results	45
3.1	Selection criteria for group membership	45
3.1.1	Dwarf galaxies and the Color Magnitude Diagram	45
3.1.2	Extraction of dwarf galaxies	48
3.2	Results from the selection process	49
3.2.1	Results HCG 16	49

CONTENTS

3.2.2	Results HCG 19	53
3.2.3	Results HCG 30	53
3.2.4	Results HCG 31	54
3.2.5	Results HCG 42	54
3.3	Spatial distribution	55
3.4	Density distribution	59
3.5	Galaxy counts	60
3.6	The Luminosity Function of HCGs	66
3.7	Zero-velocity surface R_0	68
4	Discussion and conclusions	73
4.1	Dwarf galaxies in CGs	74
4.2	The Luminosity Function	76
4.3	Density and spatial distribution	79
4.4	Mass and radius	83
5	Outlook	87
	Appendix	i
A	Selection examples for dwarf galaxies	i
B	Selected dwarf galaxies	vii
C	Velocities of HCG member galaxies	xiii
	List of Figures	xvii
	List of Tables	xix
	Bibliography	xxi

Chapter 1

Introduction

1.1 Compact Groups of Galaxies

Investigating the distribution of galaxies in the Universe it became apparent, that they are not uniformly distributed. Galaxies are found in different environments: in the field, in groups, and rich clusters. Filaments are observed with huge voids between them showing no galaxies and the cross over points are dominated by galaxy groups and clusters. These environments can have significant effects on galaxy properties such as morphology and stellar, gas, and dark matter (DM) content. Various astrophysical processes occur in the different environments, for example interactions and mergers, harassment, accretion of companion galaxies, infall of gas and ram pressure stripping. Galaxies in turn have feedback effects on their environment via outflows of mass, energy, and enriched material. Approximately 50% of the galaxies in the Universe are not isolated but found in groups or clusters. These two systems differ particularly in the number of member galaxies, the mass, radius, the observed line of sight velocity dispersion of member galaxies, and the mass-to-light ratios (M/L)^[1].

Galaxy clusters are conglomerations of hundreds or thousands of galaxies. They have masses of $\approx 10^{14}$ to $2 \cdot 10^{15} h^{-1} M_{\odot}$ ^[2] and radii of 1 to $2 h^{-1}$ Mpc and the observed line of sight velocity dispersion lies between 400 and 1400 km/s (Cox 2000). The nearest large galaxy cluster (at a redshift of $z = 0.004$) is the Virgo Cluster, which contains approximately 2500 member galaxies and shows a diameter of $\approx 1 h^{-1}$ Mpc. Galaxy clusters are dominated by DM ($\approx 90\%$). Modern analyses (Carlberg et al. 1996) determined cluster M/L ratios to $\approx 300 h M_{\odot}/L_{\odot}$. All clusters of galaxies produce extended X-ray emission due to thermal radiation from hot intra cluster gas. The X-ray temperature for galaxy clusters is $2 \cdot 10^7 - 10^8$ K (or 2 – 14 keV).

In contrast, galaxy groups have less than 100 member galaxies. They have masses between $10^{12.5}$ and $10^{14} h^{-1} M_{\odot}$, and radii between 0.1 and $1 h^{-1}$ Mpc so that they are smaller

¹ always in solar units M_{\odot}/L_{\odot} ; $M_{\odot} = 1.99 \cdot 10^{30}$ kg; $L_{\odot} = 3.85 \cdot 10^{26}$ W

² here and throughout this work $h = H_0/(100 \text{ km s}^{-1} \text{ Mpc}^{-1})$ with $0.5 \leq h \leq 1.0$, new measurements determined $h = 0.71$, and H_0 the Hubble constant; $1 \text{ pc} = 3.08 \cdot 10^{16}$ m)

than galaxy clusters. They are also DM dominated like galaxy clusters with M/L ratio of $\approx 200 h M_{\odot}/L_{\odot}$. The observed line of sight velocity dispersion is also smaller for galaxy groups and lies between 100 and 500 km/s (Cox 2000). The Milky Way, for example is a part of a galaxy group, the Local Group, which contains ≈ 30 galaxies.

Galaxy groups are divided into Loose Groups (LGs) and Compact Groups (CGs), which are the subject of this work.

LGs consist of 10 – 100 galaxies with large separations between the member galaxies (in the order of 1 – 10 galaxy diameters). In contrast CGs are conglomerations of less than five galaxies, which are separated by few diameters. All these systems are virialized systems where a dynamical equilibrium evolved between the disordered motion of galaxies and the mutual gravitative attraction ($E_{kin} = -1/2 E_{pot}$). It is assumed, that clusters and groups represent a key to the variety in the morphology of galaxies and the galaxy evolution. With a number density of $10^{-5} - 10^{-6} h^3 \text{Mpc}^{-3}$ CGs are the densest systems in the Universe and thus they are excellent laboratories for the study of galaxy interactions, the influence of the environment on member galaxies where internal evolution can transform the galaxy content.

CGs are also dominated by DM like galaxy clusters. A large fraction of CGs contain galaxies with kinematical and morphological peculiarities. Further a huge fraction of these galaxies have strong infrared (IR) emission and nuclear radio emission, show star-burst activity and strong interactions and merging between the member galaxies is observed. Like galaxy clusters CGs also contain a large fraction of X-ray-emitting gas within the gravitational potential well. The X-ray temperature for galaxy groups is smaller than $2 \cdot 10^7 \text{K}$ (or 2 keV) (Cox 2000).

Lot of information is available about the large CG member galaxies, but the nature of CGs is not clarified yet. They could be chance configurations of individual galaxies or physically bound systems in LGs. If CGs are physically bound systems, the role of CGs in the clustering hierarchy is still a key question. It is not clear, if CGs represent a transient evolutionary state of otherwise LGs or if they form a distinct class of objects.

This work deals with the investigation of the nature of CGs using dwarf galaxies.

1.1.1 Definition of Compact Groups

In general CGs are conglomerations of three to five spiral or elliptical galaxies (Hickson 1982) with small projected separations and thus very high spatial densities but very low velocity dispersions. Table 1.1 lists all compact galaxy groups known.

The first investigations of galaxy groups and galaxies showing signs of interaction are published in two catalogs the “Atlas of Interacting Galaxies” by Vorontsov-Vel’Yaminov (1977) and the “Atlas of Peculiar Galaxies” by Arp (1966). Shakhbazian (1973) and others allocated 376 CGs investigating 18% of the sky. Rose (1977) and Hickson (1982) were the first who made systematic searches for dense systems on the sky.

Hickson (1982) was the first, who defined selection criteria for CGs. He visually investigated the red prints of the first Palomar Observatory Sky Survey (POSS) covering 67% of the sky using three selection criteria - the **population criterion**, the **compactness**



Figure 1.1: HCG 79 (also known as Seyfert’s Sextet, left image) and HCG 87 (right image) observed with the Hubble Space Telescope (HST). HCG 79 is the most compact galaxy group with a median galaxy separation of 6.8 kpc and a radial velocity dispersion of 138 km/s between the four accordant galaxies. The spiral galaxy in the center has a much higher redshift compared to the other galaxies and thus does not belong to the CG. HCG 87 consists of three galaxies and a discordant redshift galaxy in the center. The median galaxy separation is 39.9 kpc and the median radial velocity dispersion averages to 120.2 km/s.

criterion, and the **isolation criterion**.

The population criterion defines groups to be small relatively isolated systems of typically three to five bright spiral or elliptical galaxies, which are located in close proximity to one another. Further, these galaxies have to be in a 3 mag range ($|m_{min} - m_{max}| \leq 3.0$ mag) of the brightest galaxy m_{max} .

The compactness criterion defines the mean surface brightness of the groups calculated by distributing the total magnitude of the bright suggested group members over the smallest circular area containing the geometric centers of the galaxies to be smaller than 26 mag/arcsec².

In order to ensure the isolation of the group it’s surrounding has to be considered. Therefore a group has to be rejected, if a galaxy lying in the 3 mag interval ($m \leq m_{max} + 3$)

appears within three radii of the inner circle (defined in the compactness criterion). Using these selection criteria Hickson (1982) visually identified 100 CGs, which were summarized as Hickson Compact Groups (HCGs).

As an example of HCGs, Figure 1.1 illustrates HCG 79 and HCG 87 observed with the Hubble Space Telescope (HST). Interactions, which are taking place between the member galaxies can be seen in the tidal arms. They were formed due to gravitational interactions and suggest that this group is a true physical association. It is the most compact galaxy group with a median galaxy separation of 6.8 kpc between the four accordant galaxies and a radial velocity dispersion of 138 km/s. This HCG is so dense that it would fit within the Milky Way (Hickson 1994). The discordant spiral galaxy in the center has a much higher redshift compared to the other galaxies and thus can be excluded as a background galaxy. This represents a very good example how one can fail with the membership neglecting radial velocity information.

HCG 87 consists of three galaxies and a discordant redshift galaxy in the center. The median galaxy separation is only 30.9 kpc and the median radial velocity dispersion averages to 120.2 km/s, which is approximately as dense as HCG 79.

Later, Hickson et al. (1992) determined the radial velocities of all (large) galaxies in HCGs and excluded all galaxies larger than 1000 km/s of the median group velocity to be non member galaxies. This had to be done, because galaxies with velocities larger than 1000 km/s could not belong to the virialized system ($E_{kin} = -1/2 E_{pot}$) as their escape velocity is too high – they would fly apart. Thus they are assumed not to be associated with the group. After determining the velocities of HCG galaxies 92 HCGs remained. In general, redshift information is necessary in order to reveal if these groups are physically bound systems or just projection effects.

Up to now other catalogs (Table 1.1) are available including for example the Shakhbazian CGs, Southern CGs (SCGs), Redshift Selected CGs (RSCGs), and the Updated Zwicky Catalog CGs (UZCCGs). Prandoni et al. (1994) developed an algorithm for an automated search of compact galaxy groups, which accords to Hickson’s selection criteria in order to produce a new sample of CGs in the southern sky and further to reach fainter magnitude limits than HCGs. With this method they identified 59 new SCG candidates around the South Galactic Pole. Iovino (2002) used a similar method but considered a larger area identifying 121 SCGs. The confirmation of CGs on the sky unavoidably requires velocity information of the group member candidates. Barton et al. (1996) selected HCG-like systems from a complete, magnitude limited redshift survey and identified 89 RSCGs.

Up to now hundreds of CGs (e.g. Shakhbazian CGs, HCGs, SCGs, RSCGs, UZCCGs) are known, but HCGs are the most widely studied of them.

1.1.2 Nature of Compact Groups

There are a lot of unsolved questions concerning CGs, especially concerning their nature. It is not clear, whether CGs are chance configurations of individual galaxies in higher density

name (1)	number (2)	field/survey (3)	references (4)
Shakhbazian CG	376	200 POSS ^a prints 18 % of the sky	e.g. Shakhbazian (1973)
Hickson CG (HCG)	92	POSS prints 67 % of the sky	Hickson (1982, 1994)
Southern CG (SCG)	59	digitized galaxy catalog produced at the Royal Observatory of Edinburgh $\approx 1300 \text{ deg}^2$ around the South Galactic Pole	Prandoni et al. (1994)
	121	“ $\approx 5200 \text{ deg}^2$ (25 % of the southern sky)	Iovino (2000, 2002)
Redshift Selected CG (RSCG)	89	CfA2 ^b + SSRS2 ^c	Barton et al. (1996)
UZC CG	291	3D UZC galaxy catalog ^d includes ≈ 20000 galaxy redshifts	Focardi & Kelm (2002)

^a Palomar Observatory Sky Survey

^b Center for Astrophysics Redshift Survey (CfA2)

^c Southern Sky Redshift Survey

^d Falco et al. (1999)

Table 1.1: Compact galaxy group (CG) catalogs; column (1): the name of the CG, column (2): number of identified CGs, column (3): catalog or field, from which the CGs were extracted, column (4): references

regions like LGs, or if they are physically bound systems. This section describes what is known about the nature of CGs from the observational and the theoretical point of view. Comprising proximity in redshift space and in projection remain the most important tracers of associations between galaxies in CGs (Diaferio et al. 1995, 1994, Moore et al. 1993) while interaction features between member galaxies represent a first probe of physical associations. Ostriker & Tremaine (1975) and Press & Schechter (1974) addressed the importance of merging concerning the evolution of galaxies for the first time. If CGs are physically bound systems, gravitational interaction can occur and they can play an important role concerning the dynamical evolution and structure of a huge fraction of galaxies. The environment has effects on galaxy properties such as morphology, gas, and stellar content. Features of merging and interaction like e.g. distortions in the morphology of (spiral) galaxies are a very good indicator for gravitationally bound systems.

Further various astrophysical processes occur in different environments. In dense ones the accretion of companion galaxies and the infall of gas are possible. Galaxies also have feedback effects on their environment like outflows of gas and enriched material. Examining galaxies in CGs concerning signs of interaction, merging, and further searching for galaxy outflows and inter group material gives important clues to the nature of the CG.

The argument for CGs being chance configurations is mainly based on the absence of facts showing that the processes of interaction and merging are extensively taking place in CGs. Few observations pointing to chance configurations exist, such as the absence of strong radio and far IR (FIR) sources (Sulentic & de Mello Rabaca 1993, Hickson et al. 1989b). Sanders & Mirabel (1996), Kormendy & Sanders (1992), Campos-Aguilar & Moles (1991) and Maccagni et al. (1990) showed that tidal interactions of galaxies are very important concerning star-burst activity in galaxies and therefore the absence of strong FIR sources can rule out merging events. Investigating FIR emission and optical signs of merging like tidal arms Zepf (1993) found, that only 7% of the galaxies in CGs are actually undergoing a merger.

A larger fraction of spiral galaxies and a lack of blue elliptical galaxies (Pildis 1995, Zepf & Whitmore 1993, 1991) are some observational indicators that CGs can be chance configurations.

Another argument concerning the opinion that CGs are chance configurations of individual galaxies is concluded from theory. Hickson et al. (1992) calculated the crossing times t_c (Table 2.1) of HCGs and found that $t_c \approx 0.02 H_0^{-1}$, which is much smaller than the Hubble time (inverse Hubble constant H_0 , giving an estimate of the age of the Universe). The crossing time of a system can be calculated by $t_c = d_m/v$ where d_m represents the linear size of the system and v the internal velocity. Numerical simulations indicate that the system would collapse due to the small velocity dispersion (≈ 250 km/s in HCGs) and the member galaxies would merge forming a large elliptical galaxy on timescales, which are typical to the crossing times t_c of the groups (Diaferio et al. 1994, Bode et al. 1993, Governato et al. 1991, Kodaira et al. 1991, Barnes 1989, 1985, Navarro et al. 1987, and Mamon 1986). Since the crossing times t_c of HCGs are $\approx 1/100$ of the Hubble time, they should be very rare or even not existing. However, the observed frequency of HCGs

is in contradiction to the small crossing time calculated (see section 1.1.1) thus Walke & Mamon (1989) and Mamon (1986) suggested that HCGs are chance alignments of galaxies.

In the following the arguments are summarized, which strengthen the second model that CGs are physically bound systems.

The previous argument, that the small crossing time leads to a chance configuration of galaxies, can be debilitated with another theoretical assumption. As mentioned before the high abundance of HCGs does not comply with the short lifetimes predicted by merger simulations (e.g. Barnes 1989), but it can be solved by considering a massive, not excessively concentrated DM halo (Athanasoula et al. 1997). With such a massive DM halo the life time of CGs can be lengthened, which would fit with the observed frequency of CGs.

The existence of a common DM halo is a good indicator for a physically bound system. Although the first hints concerning a common DM halo arose from numerical simulations, later also observational indicators were found for its existence. X-ray emission from hot intra group gas is a very good indicator if a system is physically bound or not. Observations of X-ray emission in a large number of CGs showed that gas is more extended and not implicitly related to the galaxies. Most of the intra cluster gas is diffuse and very hot, especially in dense and massive clusters. A diffuse emission of hot gas suggests that the gas is distributed throughout the cluster, but still gravitationally bound to it (Ponman & Bertram 1993). The temperature of the gas correlates with the velocity dispersion of the cluster's member galaxies and allows an alternative probe of the gravitational potential of clusters.

Schwartz et al. (1980) first investigated X-ray emission from compact poor galaxy clusters. They found that the X-ray properties are similar to X-ray properties of rich galaxy clusters. Bahcall et al. (1984) were the first, who investigated Stephan's quintet, a famous HCG concerning X-ray emission. Their results revealed a diffuse emission and no concentration of the hot gas to the galaxies. Ponman et al. (1996) investigated X-ray properties of 85 HCGs and detected diffuse X-ray emission from 22 groups. Mulchaey & Zabludoff (1998) found the existence of diffuse X-ray emission from hot intra group gas in 75 % of HCGs. The investigations of Ponman et al. (1996), Mulchaey (2000) and Helsdon & Ponman (2000) showed that the diffuse X-ray emission seems to be associated with CGs, which are embedded in LGs containing at least one elliptical galaxy.

The observation of bright galaxies in CGs also offers evidence for these groups being physically bound systems. The existence of elliptical galaxies, which were formed due to gravitational interactions between gas rich galaxies, like spiral galaxies, points to a physically bound system. Galaxy clusters for example are dominated by elliptical galaxies. Examining the fraction of spiral galaxies to elliptical galaxies, fewer late type galaxies than early type galaxies were found in groups compared to the field. Prandoni et al. (1994), Rood & Williams (1989), Hickson et al. (1988a), Sulentic (1987), and Hickson (1982) studied the morphology of the CG galaxy population and revealed that the fraction of spiral galaxies is smaller in CGs than in the field. Analysing spiral galaxies in CGs it was discovered that a large fraction of these galaxies show irregularities, asymmetries and distortions in the

spiral arms (Mendes de Oliveira & Hickson 1994, Rubin et al. 1991), which give evidence for strong gravitational interaction.

If merging occurs in CGs it would be expected to find a large fraction of elliptical galaxies in CGs. From theory it was found that elliptical galaxies, which were formed by mergers of gas rich galaxies, should show bluer colors compared to normal galaxies. Moles et al. (1994) and Zepf & Whitmore (1993) examined elliptical galaxies in HCGs and found a very small enrichment of elliptical galaxies, which show blue colors. Further a large number of blue galaxies in Shakhbazian CGs was discovered. Thus it was suggested, that CGs are similar to clusters, which are dominated by elliptical galaxies.

Interactions and mergers do not only change the morphology of the galaxies in a cluster or a group but provide also a mechanism of redistributing gas from the galaxies into regions where the gas is only weakly gravitationally bound to a specific galaxy. Observations of the neutral hydrogen (HI) at 21 cm can reveal the mass distribution of cool galactic and intergalactic gas. Williams & Rood (1987) were the first, who examined CGs and determined the median HI mass of $2.2 \times 10^{10} M_{\odot}$. They concluded, that CGs have a deficit of HI compared to LGs. Williams et al. (1991) and Williams & van Gorkom (1988) obtained high resolution studies of CGs and found that the gas is not confined to individual galaxies. They found e.g. radio continuum from a common envelope, which surrounds the group. This result strengthens that these groups are not chance alignments, because gas, which belonged to individual galaxies was distributed throughout the CG. The studies of Menon (1992, 1991) showed a deficit concerning the radio emission in the disks of CG spiral galaxies suggesting that the interactions taking place in CGs have removed a huge fraction of the gas from the galaxies.

Further IR observations can be used to estimate the amount of star-formation activity in CGs. Up to now the data are mainly based on data derived from the IRAS satellite. From a search of the Point Source Catalog Hickson et al. (1989b) identified IR sources in 40 HCGs. They found that the FIR to optical luminosity is greater in CGs than in isolated galaxies, which gives an argument that the star-formation in HCG galaxies is triggered by gravitational interaction. However, Venugopal (1995) and Sulentic & de Mello Rabaca (1993) argued that the low resolution of the IR data makes it difficult to assign the IR flux to the individual galaxies.

The investigation of the spatial distribution of HCG member galaxies and the environment in which HCGs are found can give insight into the question if the formation of HCGs implies a dense environment and if therefore HCGs are embedded in larger systems e.g. LGs. Studying that aspect Hickson & Rood (1988b) found that CG galaxies are not random distributed, but subjected to an elongated distribution. Montoya et al. (1996) investigated light profiles of 42 HCGs containing the large group members and found a core radius, which would not be expected, if CGs would be chance alignments within LGs. Tovmassian et al. (1999) showed that radial velocity dispersions of HCGs correlate with the elongation of groups. The dependence of the radial velocity dispersions of HCG galaxies on their elongation suggests that the members rotate around the gravitational center of the group. Furthermore Tovmassian & Chavushyan (2000) evidenced that the accordant red-shift galaxies in the environment of a dozen studied HCGs and poor groups of galaxies are

distributed in narrow strips of a few hundred kpc in width. Examining the surrounding of HCGs, it was found that most of these groups are not isolated systems. Rood & Struble (1994) revealed that roughly 70% of HCGs lie in the boundaries of LGs. Studying the distribution of galaxies in redshift space in order to explore the embedding of these groups into large systems Barton et al. (1996), Garcia (1995), Ramella et al. (1994), Sakai et al. (1994), and Vennik et al. (1993) indicated that CGs are not isolated, but condensed within LGs. Focardi & Kelm (2002) derived from observations that multiplets, which contain between 3 and 5 galaxies, are associated with high velocity dispersion systems and are typically embedded in larger structures. From these results Ramella et al. (1994) concluded that we see HCGs, because they are being continually formed in collapsing LGs. This was also predicted by N-body simulations of rich groups of galaxies (Diaferio et al. 1994).

After modifying the original HCG catalog concerning misidentifications like discordant redshift galaxies, the interpretation of the 'truly' CGs poses several problems. Some conglomerations of galaxies identified as CGs may be the result of chance configurations of individual galaxies in higher density regions like LGs, but a huge number of CGs may be physically bound systems. The examination of the literature concerning that question showed, that the arguments for CGs being chance configurations are weak. In most of the cases these arguments could be debilitated by observations using new techniques. A huge number of arguments exists for CGs being physically bound systems. It was found that these groups are not isolated, but embedded into larger systems like LGs. It is therefore very likely that CGs are formed as sub-condensations in LGs.

The main goal of this work is the search for dwarf galaxies in the surrounding of HCGs. This is performed here for the first time. If dwarf galaxies are found in the HCG environment, they will give clues to the nature of HCGs.

1.2 Dwarf galaxies and their environment

The investigation of galaxy populations in different environments can provide insight into the evolution of galaxies. Dwarf galaxies are the most common galaxies in the Universe, e.g. more than 60% of the objects in the Local Group are dwarf galaxies. They are therefore very important for the understanding of evolution and formation of galaxies. Dwarf galaxies are also of cosmological interest as their spatial distribution constraints the primordial density fluctuations.

1.2.1 Classification of Dwarf Galaxies

The strict definition of dwarf galaxies is still under debate but the general accepted properties characterizing them are: small size (sometimes adopted not to exceed 10 kpc), morphology, and low luminosity. They are roughly divided into two morphological types – early and late types. Late type dwarfs, consisting of dwarf irregulars (dIrrs) and a smaller amount of dwarf spirals, are analogous to giant galaxies: they are gas rich, have blue colors

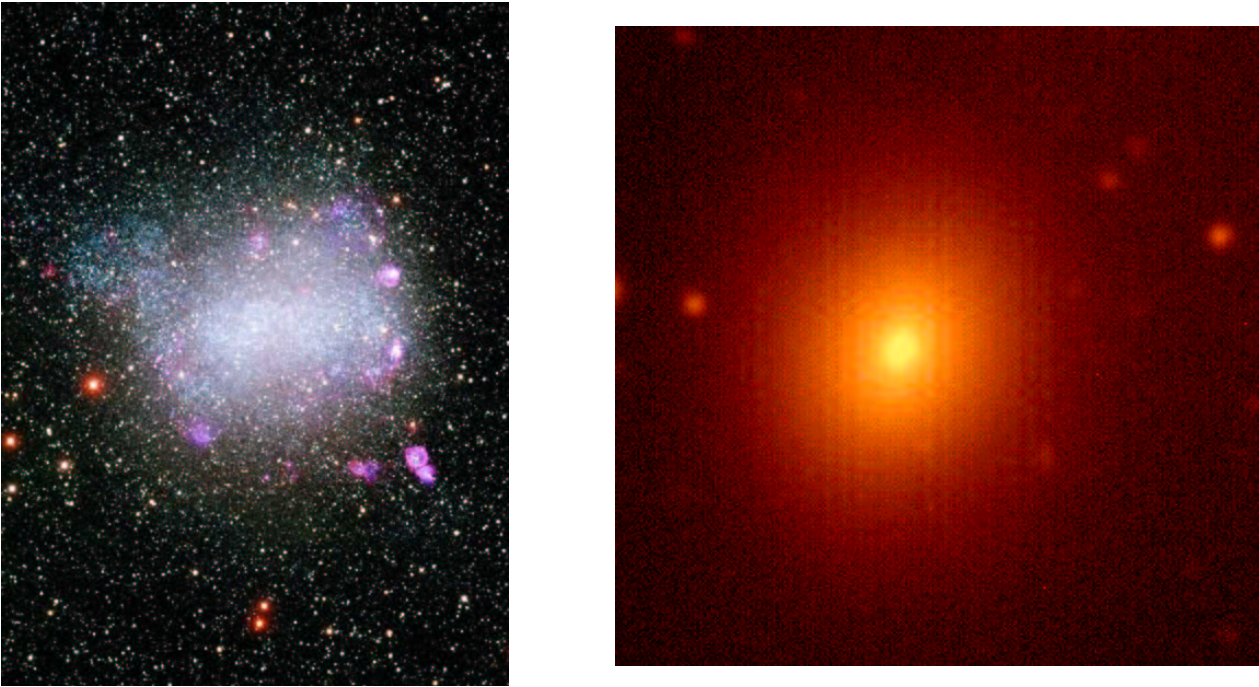


Figure 1.2: Two dwarf galaxies as examples for a dIrr and a dE galaxy. The dIrr galaxy NGC 6822 (also known as Barnard's Galaxy) in the left image has a distance of 460 kpc and is located in the Local Group. Due to its spatial stellar distribution the galaxy is classified as dIrr. It further possesses an unusually high abundance of HII (ionized hydrogen) regions, which are found surrounding young stars. Larger HII regions are visible surrounding the small galaxy. The picture of NGC 6822 was taken by the Local Group Galaxies Survey Team, NOAO, AURA, NSF (Astronomy Picture of the Day, 2002 January 23). On the right M 32, a dE galaxy of the Local Group, is shown. This galaxy is the companion galaxy of M 31, the Andromeda galaxy, which is the largest galaxy of the Local Group. dEs like M 32 have little or no measurable gas or dust and are completely composed out of stars and appear redder than spiral galaxies. The picture was taken by Bill Keel (U. Alabama) using the 1.1 Meter Hall Telescope, Lowell Observatory (Astronomy Picture of the Day, 1996 January 06).

and irregular isophotes. They are predominantly found in regions of low galaxy density like in the field or in the outer parts of clusters (Schombert et al. 1995). The described group also comprises the subgroup of tidal dwarfs, formed by interactions between large galaxies, and showing a marked irregular morphology. The left picture of Figure 1.2 shows the dIrr galaxy NGC 6822 as an example.

In contrast early type dwarfs, classified as dwarf ellipticals (dEs), have red colors, smooth elliptical isophotes, and are principally found in areas of high galaxy density like cluster centers or as close companions to giant galaxies (Binggeli et al. 1987). The prototype dE is a centrally concentrated galaxy with a smooth surface-brightness profile fainter than

22 mag/arcsec², which can be fitted by a single or modified exponential profile (e.g. Jerjen & Binggeli 1997, Cellone et al. 1994, and Ferguson & Binggeli 1994). This is in strong contrast to regular elliptical galaxies whose light distribution can be described best by a de Vaucouleurs $R^{1/4}$ law. Thus it is possible to distinguish between dEs and bright elliptical galaxies in regard to the surface brightness profiles. Furthermore it is established that dEs show a stellar population which is completely different from bright elliptical galaxies (Jerjen & Binggeli 1997). It is therefore assumed, that the history of low-mass elliptical systems is very different from that of the giant elliptical galaxies (e.g. Conselice et al. 2001). Figure 1.2 shows M 32 as an example of a dE galaxy of the Local Group.

Apart from the general classification of early type systems into dEs Gallagher & Wyse (1994) made a further distinction for the faintest dE galaxies classifying them as dwarf spheroidals (dSph) based on their total magnitude. Further Sandage and Binggeli (1984) introduced the dS0 class of galaxies for some dwarf member galaxies of the Virgo Cluster to mark their similarity with regular S0 galaxies. The dividing lines among these subclasses are fuzzy and may differ between individual studies.

The morphological classification of dwarf galaxies identified in the HCG sample is described in more detail in chapter 3. dE galaxies will be defined due to their morphology, radial light profile, and low-surface-brightness.

1.2.2 Dwarf galaxies in Hickson Compact Groups

It has become apparent that CGs are more likely physically bound systems, but it is not proven yet. In this thesis for the first time dwarf galaxies are used in order to determine the nature of HCGs. This is possible, because the evolution of dwarf galaxies is strongly influenced by their environment. As described in section 1.2.1 a distinction can be observed between the dominant type of dwarf galaxies in dense galaxy environments like galaxy cluster centers (dEs and dSphs) and low density ones as in the outer parts of galaxy groups (dIrrs). Dwarf galaxies are not only segregated by morphology within clusters, but their relative numbers also depend upon environment. Binggeli et al. (1990) have found that dEs are more common in clusters than dIrrs, while the reverse is true in the field population. Concerning the relative fraction of dwarfs to giants, Ferguson & Sandage (1991) have found that galaxy clusters and rich groups have higher dwarf-to-giant ratios than poor LGs.

Since the goal of this thesis is the characterization of the nature of HCGs, the dwarf galaxy content in HCGs (16, 19, 30, 31, 42) which were selected from the catalog of HCGs (Hickson 1994) is identified and examined. Particularly the distribution and fraction of dE galaxies compared to dIrr galaxies in the CGs is investigated. CGs are ideal objects for investigations, because they contain a small number of galaxies, but have densities similar to or greater than cluster centers. Due to their high density CGs are expected to be similar to clusters, with even more dEs per unit mass than in clusters.

In the following an overview of the existing data and the results of their analysis concerning the (dwarf) galaxy content in dense environments is given. Large data sets exist focusing on the photometric properties of bright and faint galaxies in clusters, LGs, and in the

field (Conselice et al. 2003, 2002, 2001, Secker & Harris 1997, Binggeli et al. 1987), but in CGs up to now only the bright galaxies are well studied. De Carvalho et al. (1997, 1994) obtained photometry (in an area of $0.5^\circ \times 0.5^\circ$ on digitized photographic plates) and spectroscopy of the nearest CGs and found that the groups have on average eight members. Although the data are complete down to $M_B = -16$ mag, a level which only reaches the bright end of the dwarf galaxy range, they found evidence of faint galaxies in CGs. Hunsberger et al. (1996) used short exposure CCD images to obtain luminosity functions of CGs down to $M_R = -14$ mag and identified tidal dwarf candidates in seven groups. However, their field of view is limited to $13' \times 13'$ and they only have data in the R band. Zabludoff & Mulchaey (1998b) obtained photometry and spectroscopy of two HCGs and found that CGs have a large number of group members (> 30), which are concentrated in the group centers. Although CGs were believed to lack faint galaxies, the studies of de Carvalho et al. (1997, 1994) and Zabludoff & Mulchaey (1998b) detected a considerable number of dwarf galaxies showing that the population is larger than assumed before. However, the data only reach the bright end of the dwarf galaxy range, because the initial study of dwarf galaxy segregation and fractionation in different environments is based on photographic data from Schmidt telescopes or the observed area is limited to the central region. The outer regions are unstudied.

With the spatial distribution of dwarf galaxies it is possible to determine the extension of CGs, if they are limited to the compact area of the defined original HCG galaxies, or if HCGs are much more elongated. While dEs are found in cluster centers it is assumed that these galaxies are a good indicators for their environment. It is possible to determine the nature of CGs whether they are chance configurations or physically bound systems in regard to the distribution and fraction of dEs especially in the amount of dE galaxies compared to dIrr galaxies. Finding dEs in HCGs will suggest, that these systems are physically bound.

An aim of this work consists in the detection of dwarf galaxies in HCGs especially in their outer regions. To reach the needed levels of surface brightness very deep data are necessary covering a large field. Due to their small size and their low surface brightness, dwarf galaxies are difficult to observe. Only recently it has become possible to obtain deep, wide-field CCD photometry of significant numbers of these galaxies, mostly in clusters. For the purposes wide-field mosaic data with fainter limits and much improved photometry were obtained for a sample of HCGs (see section 2.1). The lack of velocity information makes it impossible to establish directly membership for probable dwarf galaxy member candidates. Therefore the fields covering the sample HCGs were observed in the B - and R -band in order to create colour maps. On the base of the colour maps a Color Magnitude Diagram (CMD) for the dwarf galaxies will be generated. This work makes use of the fact, that dE member galaxies of galaxy clusters show a well defined sequence - the red sequence in the CMD. Thus it is expected to find such a sequence in the CMD diagram of galaxies identified in the large field around HCGs. All the galaxies in the red-sequence area are high probability dE candidates, which will be investigated due to their morphology, surface brightness, and radial light profile in order to exclude background galaxies.

If dwarf galaxies are found, it will be possible to determine the Luminosity Function (LF)

of HCGs, which defines the number density of galaxies per unit luminosity L . The LF is a description of the galaxy content of an environment and thus an adequate method to determine the nature of these groups. With the LF the nature of HCGs can be further investigated, whether they are more similar to galaxy clusters or to the field by comparing the LFs of these different environments. The LFs of e.g. Coma and Virgo Cluster are very well studied and also the LFs of field galaxies. Previous studies investigating LFs of CGs gave contradictory results since they did not reach the faint-end (all galaxies fainter than -15 mag) of the LF, missing a large part of dwarf galaxies. Heiligman & Turner (1980) were the first who determined the LF of CGs. Investigating a sample consisting of 10 CGs, they found that CGs contain fewer faint galaxies than a field galaxy sample does. Hickson (1982) determined the LF in HCGs and Kodaira et al. (1991) determined the LF in some Shakhbazian groups finding similar results. The LF of HCGs derived in this work is the most complete LF of HCGs up to now determined.

Finally the existence of dwarf galaxies can be used to proof cosmological models for structure formation. One of the outstanding questions in cosmology is the evolution of structure on different mass scales. The hierarchical model, whose basic concept was first noted by White & Rees (1978), explains very successfully the spatial distribution of galaxies – large structures and clustering on all scales as well as the extent of individual galaxies. Within that model first small objects are formed evolving then through accretion or merging to larger systems. Spiral galaxies can keep their morphology when diffuse matter or small dwarf galaxies are accreted. Thus structure formation is a continuous and dynamical process. In the case of merging between spiral galaxies of similar size the stellar disc will be destroyed and an elliptical galaxy can be formed. Nevertheless, it is also possible that elliptical galaxies were formed in a single collapse of primordial material.

It is assumed, that galaxy clusters evolve from the accretion of smaller groups (Zabludoff & Zaritsky 1995, Binggeli et al. 1993, White et al. 1993, Briel et al. 1992, and Mellier et al. 1988). However, it is still not clear, if poor groups evolve hierarchically, too. The study of dwarf galaxies in CGs will bring more light into this field by examining the distribution of dwarf galaxies.

Chapter 2

Data and data reduction

For the investigation of dwarf galaxies at large distances CCD detectors with high quantum efficiency are necessary. In order to assess the dwarf galaxy content in the surroundings of CGs a large field of view is required. In the end of the 1990's Wide Field Imager (WFI) cameras, which are array CCD cameras, consisting of several CCD chips were developed. Thus the surroundings of HCGs can now be observed in one single pointing.

2.1 The HCG sample

The need for obtaining a new data sample of HCGs grew from the demands concerning the investigation of dwarf galaxies in the environment of these groups. There were some constraints which influenced the selection of candidate HCGs since photometric data were needed. Most important, the CGs should be close by in order to resolve the morphology of dwarf galaxies reasonably. This requirement could be accomplished for dwarf galaxies with an apparent diameter larger than $2''$.

Furthermore, HCGs were chosen because the catalog of HCGs is by far the most studied catalog of CGs. Thus, the sample consists of close-by HCGs. Since the data were obtained at the ESO observatory, the last requirement was the visibility from Chile. Five HCGs have been observed, which are listed in Table 2.1.

2.2 The data

A large field of view together with a high quantum efficiency is necessary in order to establish the dwarf galaxy content in the surroundings of CGs. Normal CCD detectors provide images with a high quantum efficiency, but with a small field of view (typically $7' \times 7'$). The Wide Field Imager (WFI) is an array CCD camera, consisting of $8 \times (2046 \times 4098)$ chips. It acquires a large field of view ($0.54^\circ \times 0.57^\circ$). Figure 2.1 shows the design of the detector head of the WFI and the arrangement of the CCD chips.

HCG	α_{2000} [hh mm ss]	δ_{2000} [° ' "]	z_m	D_m [$h^{-1} \cdot \text{Mpc}$]	N	d_m [kpc]	Δv [km/s]	t_c [$H_0 c_t$]
16	02 09 32	-10 09 00	0.0132	39.6	4	44.6	123	0.0275
19	02 42 43	-12 25 25	0.0142	42.3	3	-	-	-
30	04 36 27	-02 50 07	0.0154	46.2	4	51.3	72.4	0.0603
31	05 01 40	-04 15 24	0.0136	40.9	3	49.0	85.1	0.0479
42	10 00 18	-19 38 54	0.0133	39.9	4	44.7	213.8	0.0155

Table 2.1: Sample of HCGs observed in this project; α_{2000} & δ_{2000} = coordinates, z_m = mean redshift of the group, D_m = distance of the group along the line of sight in units of h , N = number of accordant galaxies, d_m = median galaxy separation, Δv = radial velocity dispersion, t_c = crossing time defined as $4v/\pi d_m$ (v : 3-dim. velocity dispersion; all data were taken from Hickson (1994))

Using the ESO¹/MPIA² 2.2 m telescope with the WFI it was possible to image the CGs in single pointings.

The HCGs were observed while splitting the integration time into four sub exposures. The telescope was spatially offset among the sub exposures in order to cover the gaps between the individual CCD images. The observations were carried out in the period from 1999 December 15 to December 18 by Dr. D. Bomans and Dr. R. Tüllmann (Astronomisches Institut, Ruhr-Universität Bochum). Table 2.2 shows the characteristics from the observing log of the WFI observations. Previous works studying dwarf galaxy segregation and decomposition in differing environments (e.g. Ferguson & Sandage 1991, Binggeli et al. 1990) is based upon photographic data from Schmidt telescopes, therefore the data obtained using the WFI on the 2.2 m telescope are of superior quality, with better resolution and fainter limits, even though the groups are at larger distances.

2.2.1 The Wide Field Imager observations

The WFI focal reducer-type camera is located at the Cassegrain focus of the 2.2 m Ritchey-Cretien telescope at La Silla. The detector is composed of eight (2k × 4k) CCD chips, which are arranged in two rows (Figure 2.1). The CCD chips are separated by a gap of 30 ± 2 pixel in vertical direction and 98 ± 2 pixel in horizontal direction. This results in a filling factor of 95.9% (Baade 1999). The image scale amounts $0''.238$ per $15 \mu\text{m}$ pixel which results in a field of view of $0.54^\circ \times 0.57^\circ$. The small pixel scale fully samples the seeing disk under conditions typical for La Silla. Across the focal plane the scale is constant to better than 0.08%, which means that without correction for this variations surface photometry is accurate to $\approx 2 \cdot 10^{-3}$ mag. A typical desideration of focal reducers is the sky concentration which amounts to less than 2%. All CCDs show a high quantum efficiency of about 90% at

¹ European Southern Observatory

² Max-Planck-Institut für Astronomie

HCG	filter	t_{exp} [s]	seeing ["]	date [dd:mm:yy]
16	B/99	1×1980	1.38	15:12:99
		3×1140		
19	Rc/162	4×675	1.15	16:12:99
	B/99	4×1350	1.61	17:12:99
30	Rc/162	4×675	0.92	17:12:99
	B/99	4×1350	1.65	18:12:99
31	Rc/162	4×675	1.34	18:12:99
	B/99	4×1350	1.15	16:12:99
42	B/99	4×675	0.97	15:12:99
		1×1217	1.53	16:12:99
		1×1350		
	1×1231			
Rc/162	4×675	1.07	15:12:99	

Table 2.2: Observing log for the WFI observations giving information about the used filter, the exposure time (t_{exp}), the seeing and the date of the observation

500 nm but they also show a non linearity of 0.2% to 0.8% (Baade 1999). However, as can be seen in the reduction section it was not necessary to correct for this low non-linearity of the CCD chips.

With this large field of view, which is unique among the current ESO telescope/detector combinations, the surrounding of the observed HCGs up to a distance of $\approx 200 h^{-1}$ kpc was covered.

The weather conditions during the observation run were good. The seeing over the five nights averaged out to $1''.3$. Just in the case of HCG 30 in the B band it was at $1''.65$ (Table 2.2). The exposure times for the B band images amount to 5400s and to 2700s in the R band resulting in good photometry for the group galaxies. Each of these exposures was split into four sub exposures. This was necessary in order to cover the gaps between the individual CCD chips but also in order to allow flexibility concerning weather changes. For calibration purposes standard stars from the Landolt (1992) sample were observed.

2.2.2 Filter characteristics

The data were obtained using the Johnson–Cousin B and R broad band filter (B/99, Rc/162). The filter transmission curves of the standard filter set are shown in Figure 2.2. More detailed information of the used B and R filters are given in Figures 2.3 and 2.4. The characteristics of the B-filter correspond to the Johnson & Morgan (1953) system, while the characteristics of the R-filter correspond to the Cousins (1976) system. The wavelength of maximal transmission lies at 472 nm for the B filter and at 668 nm for the R filter.

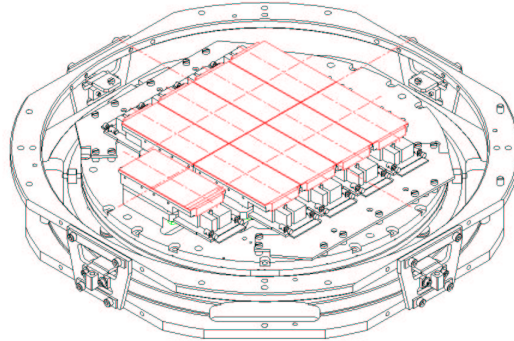


Figure 2.1: Design of the detector head of the WFI. The eight rectangles represent the 8 CCD chips from the mosaic, the additional CCD chip on the left is the tracker chip used for auto-guiding (Baade 1999).

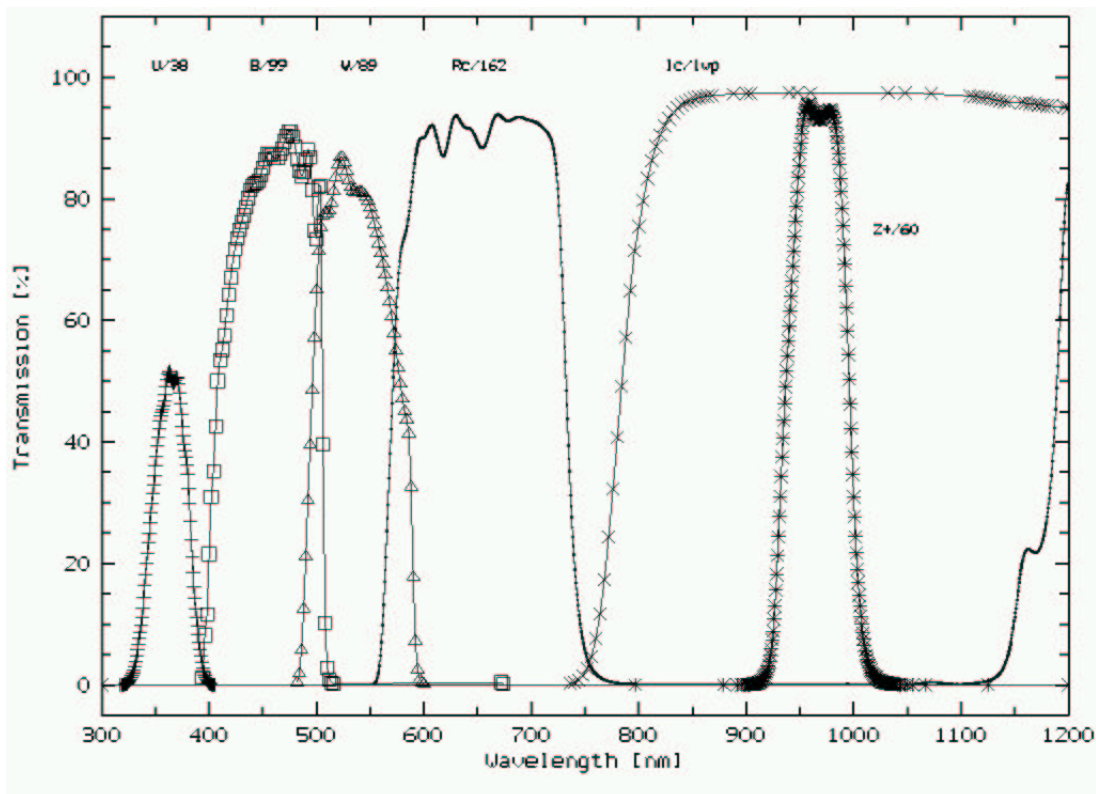


Figure 2.2: Transmission curves of the WFI broad band filter set (Baade 2002), the horizontal axis denotes the wavelength and the the vertical axis represents the transmission (in %) of the corresponding filter.

Wavelength nm	Transmission %	Wavelength nm	Transmission %	Wavelength nm	Transmission %
394	1.2	436	80.1	480	88.6
396	8.2	438	81.4	482	86.5
398	11.6	440	82.2	484	84.6
400	21.5	442	82.5	486	83.7
402	30.9	444	82.7	488	84.4
404	35.2	446	83.0	490	86.4
406	42.5	448	83.9	492	88.2
408	50.0	450	85.1	494	86.9
410	53.5	452	86.5	496	81.4
412	55.1	454	87.3	498	74.8
414	57.6	456	87.5	500	73.4
416	60.9	458	87.2	502	82.0
418	64.2	460	86.8	504	82.1
420	67.1	464	86.7	506	39.6
422	69.6	466	87.4	508	10.2
424	71.8	468	88.3	510	2.8
426	73.6	470	89.4	512	0.9
428	75.0	472	90.5	514	0.4
430	76.1	474	91.1	516	0.2
432	77.3	476	91.1	672	0.4
434	78.6	478	90.2	674	0.2

Figure 2.3: Transmission data for the broad band filter B/99 (Baade 1999)

2.3 Reduction of the mosaic data

In order to create deep mosaic images several individual pointings of the telescope were spatially offset to cover the gaps between the individual CCD images and any defects. WFI images are more complex than single CCD frames, since they comprise a total of eight individual images. The data from each exposure are stored into a single Multi Extension Fits (MEF) file. The raw data format is 142 Mbyte per MEF file. Storing the eight individual images into a MEF file means that a header with corresponding image data exists for each individual exposure. Furthermore there is a superior header for all eight extensions, where an extension is synonymous to the image file of one of the chips. These images can be activated separately using the extension number. This is very useful for the investigation of artefacts and applying solutions for specific reduction problems. In general, the eight CCD images were reduced as a MEF file in order to use as many of the standard routines as possible. The data were reduced using IRAF (Image Reduction and Analysis Facility), and specifically MSCRED³ Version 2.0 (Valdes 1998), which was originally developed for handling and reducing data from the NOAO⁴ CCD Mosaic Imager.

³ MoSaiC REDuction (Mosaic Data Handling Software)

⁴ National Optical Astronomy Observatories

Wavelength nm	Transmission %	Wavelength nm	Transmission %	Wavelength nm	Transmission %
556	0.9	676	92.9	1060	0.2
560	5.9	680	92.9	1064	0.3
564	18.9	684	93.2	1068	0.4
568	36.1	688	93.4	1080	0.3
572	52.7	692	93.3	1084	0.3
576	66.6	696	93.1	1096	0.2
580	72.6	700	92.8	1104	0.2
584	75.1	704	92.6	1112	0.3
588	80.3	708	92.1	1120	0.5
592	86.5	712	91.4	1124	0.6
596	89.7	716	90.6	1128	0.8
600	90.2	720	88.7	1132	1.2
604	91.4	724	82.9	1136	1.9
608	92.1	728	69.5	1140	3.0
612	90.0	732	50.8	1144	5.1
616	87.4	736	33.1	1148	8.7
620	87.8	740	20.2	1152	14.0
624	91.0	744	12.2	1156	19.4
628	93.5	748	7.3	1160	22.1
632	93.3	752	4.4	1164	22.2
636	92.1	756	2.8	1168	21.8
640	91.7	760	1.8	1172	22.1
644	91.4	764	1.2	1176	23.9
648	90.2	768	0.9	1180	27.7
652	88.7	772	0.6	1184	34.5
656	88.6	776	0.4	1188	45.4
660	90.3	780	0.3	1192	60.5
664	92.7	792	0.2	1196	76.1
668	93.9	804	0.1	1200	82.5
672	93.6	1056	0.1		

Figure 2.4: Transmission data for the broad band filter R/162 (Baade 1999)

During the course of the reduction it became apparent that the standard software was incapable to produce images of the quality needed. Thus new reduction solutions had to be developed, especially concerning the flattening of the strong variations in the background values of the individual CCD images, which is very important while stacking the dithered mosaic images.

The reduction of the WFI data can be divided into two steps. First a separate calibration of the eight individual CCD chips is performed. This process is similar to the reduction of regular CCD images. The basic reduction steps consist of correcting each CCD for electronic bias levels, zero exposure patterns, dark counts, pixel sensitivities, and a replacement of bad pixels. Another issue which is not typical for CCD data with smaller fields of view is the variable pixel scale due to variations in transparency and sky brightness in combi-

nation with the appropriate optics of the WFI. Thus, the standard flat field calibration operation will cause the photometric zero point to vary. Most significant artefacts are the gain variations between the CCDs and within each CCD image. Since it is intended to do photometry, the calibration to correct for the variable pixel scale across the field of view was necessary.

In a second step, the data reduction deals with the combination of the separate CCD images into a single image. The images have been obtained with a spatial offset to cover the gaps between the individual CCDs and enable correction of CCD defects.

The steps required to produce a single image from dithered exposures consist of accurately mosaicing the individual frames into single images with a homogeneous spatial sampling. In the following sections, the reduction is described in more detail. For a general overview of the use of the IRAF packages see Valdes (1998).

The aim of the reduction is the extraction of the source flux, which is one fraction of the measured detector voltage $V(x, y)$. How the main components contribute to the measured voltage at each pixel for a measurement on target can be seen in the following equation:

$$V(x, y)_{meas} = (G(x, y) \cdot (F(x, y)_{gal} + F_{sky}) + I_{dark}) \cdot t \quad (2.1)$$

where $G(x, y)$ is the photometric gain (e^-/photon) of each pixel, $F(x, y)_{gal}$ is the flux of the extended source that should be isolated, F_{sky} is the flux of the sky (photons/s), I_{dark} is the dark current (e^-/s) and t is the integration time. The main components, which contribute to the measured voltage $V(x, y)_{sky}$ at each pixel for a sky background measurement are:

$$V(x, y)_{sky} = (G(x, y) \cdot F_{sky} + I_{dark}) \cdot t \quad (2.2)$$

In general the sky frames are not free of sources, they very often contain stars in the field of view. The final flat field frame (described in detail in section 2.3.2) was determined by calculating the median of a set of many scaled sky frames in order to eliminate contamination from the background. While $C = F_{sky} \cdot t$ is a constant which normalizes the flat field frame, equation (2.2) gives:

$$G(x, y) = (V(x, y)_{sky} - I_{dark} \cdot t) / C \quad (2.3)$$

Accomplishing this procedure the object flux per unit time is determined. In order to transform this result to astrophysical magnitudes, calibration measurements are necessary. Some standard stars (objects with known magnitudes) were observed during the observation run. This final calibration step is described in section 2.4.

2.3.1 Bias correction

Before the data reduction can be started, the ESO image headers have to be modified so that the **mscred** package on WFI data can be used. The task **esohdr** in the **esowfi** package performs this transformation. It includes adding keywords used by **mscred**, setting all

CCD	im	ext [e ⁻]	Read Out Noise [e ⁻ /ADU ^a]	Gain
50	1	[1]	4.078 ± 0.082	2.020 ± 0.013
51	2	[2]	4.026 ± 0.067	2.067 ± 0.018
52	3	[3]	3.619 ± 0.083	2.285 ± 0.060
53	4	[4]	3.962 ± 0.074	2.000 ± 0.022
54	8	[5]	4.045 ± 0.090	2.043 ± 0.023
55	7	[6]	4.247 ± 0.061	2.102 ± 0.024
56	6	[7]	3.624 ± 0.070	2.230 ± 0.015
57	5	[8]	3.600 ± 0.074	2.212 ± 0.017

^a Astronomical Data Unit

Table 2.3: Read Out Noise and Gain values of each CCD Chip; the first column denotes the chip ID, the second column denotes the extension number in the header, the third column denotes the number of the MEF

geometry keywords and setting a first astrometric solution. The parameter **wcsdb** of the task **esohdr** contains the world coordinate system (WCS) database.

The headers do not contain any information concerning the **gain** and **readoutnoise** values. However, as these parameters are necessary for the reduction, they had to be added to each file. In doing so, one has to consider that different values are dedicated to each CCD Chip (1-8) of a file. The Gain and Read Out Noise values in table 2.3 were determined by calculating the average of online (WFI webpage⁵) accessible measurement report data during the time the observations were performed. These information were added using an IRAF script.

Starting the reduction first of all the exposures (objects, flats, and bias) were overscan corrected. The overscan is a region on the CCD chips along the long side in vertical direction with a width of ≈ 48 pixel. The overscan correction leads to the zero level calibration to subtract any details of line-by-line structure. The overscan subtraction and the trimming was done in one run using the task **ccdproc**.

The determination of the overscan averages the overscan along the readout direction and creates an overscan vector, then fits a smoothing function to the vector and finally evaluates the function at each readout column.

As recommended by Massey (1997) one should not take higher orders than **1** if it is intended to subtract a bias afterwards, thus a Legendre polynomial of first order was fitted along the column direction.

After the overscan correction there is still a zero level bias which is additive and had to be subtracted from all science and calibration exposures. The zero level bias is due to a base voltage, which was electronically added to the actual response of the CCD chips to the infall light in order to avoid the exposure's read noise leading to negative numbers of

⁵ <http://www.lis.eso.org/lasilla/Telescopes/2p2T/CCDs/WFI/> (as seen 2000 Dec.)

electrons. This level was measured by taking exposures of zero seconds (bias exposures) by reading out without opening the shutter of the instrument. It is sufficient to average at least ten bias exposures in order to avoid adding noise to the bias corrected files. During the observation run, 20 bias frames were obtained. Two frames were excluded from the further examination because they had a higher average count level.

In the first step the Master Bias was created by averaging zero level images (bias images) in order to weight all exposures identically using the IRAF task **zerocombine**. The **combine** parameter of the task **zerocombine**, which was set to **average**, defines the combining operation performed on the final set of pixels. The **reject** parameter, which was set to **minmax**, defines the rejection operation. The **minmax** value rejects the highest and lowest value for a given combination. With the parameter **nhigh** set to **1** and **nlow** set to **0**, only the highest and lowest values were rejected. Finally the master bias was subtracted from all frames (object, flats) using the task **ccdproc**.

2.3.2 Flat field correction

Since for sky flat exposures the light path is the same as for the science exposures at night sky flat exposures were useful to correct for multiplicative effects on small scale such as pixel variations in sensitivity and for effects on large scale like illumination inhomogeneities in the sky background and diffuse light. In practice flats are obtained by exposure to a spatially uniform source of light like the twilight sky. These twilight flats are obtained in dithered mode in order to remove stars. The counts of the flats must lie in the linearity range of the CCD chip (20000 – 50000 counts/pixel, Baade 1999) in order to receive high count values for a high Signal to Noise relation (SNR) for the Master Flat. After excluding the skyflats with values that do not lie in the linearity range, 34 skyflats in the *B* band and 25 skyflats in the *R* band remained.

The Master Flat frames were created by averaging the individual sky flat exposures using the task **flatcombine**. Cosmics were eliminated by setting the parameter **reject** to **crreject**, which ignores low pixels and rejects only high pixels.

In order to monitor the night-to-night variations of the flat field, two different Master Flats were created, one of the Skyflats of each night and a Master Flat including all Skyflats, from the four observing runs.

In order to examine the quality of the Master Flats, the Master Flat of each individual night (n1 to n4) was divided by the Master Flat of all nights. This was done using the task **mscarith**. The statistic of the result showed deviations of $\approx 0.03\%$. Thus for the Flatfield Correction of the object images the Master Flats were chosen, which were created using the Skyflats of all nights, which was very preferable due to a high SNR.

Using the task **ccdproc** the flat field correction of the object exposures got accomplished by a division by the Master Flat.

All CCD chips show hot and cold columns and punctual defects. Before continuing the reduction a bad column correction had to be performed. Bad lines and columns were replaced by linear interpolation from neighboring lines and columns. It is recommended that this was done to avoid possible arithmetic problems in the processing.

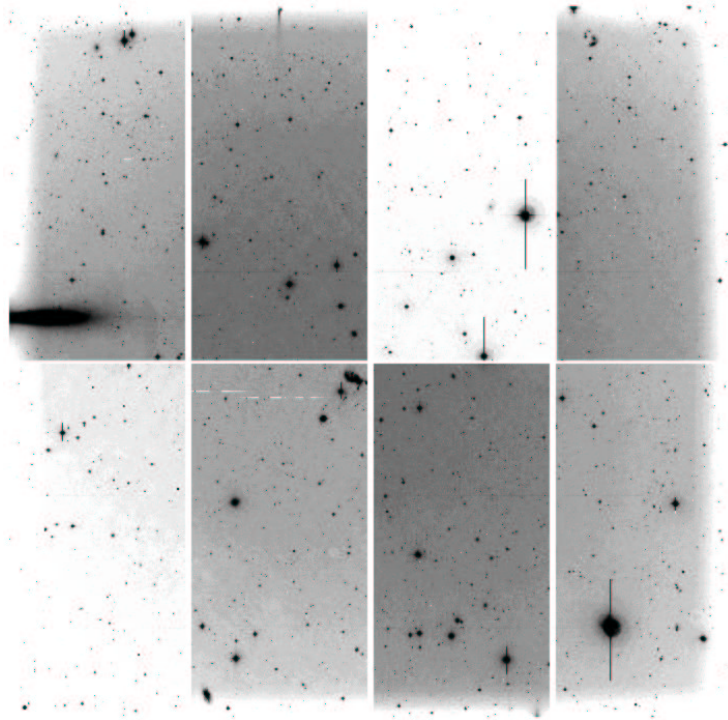


Figure 2.5: Flatfield corrected image of HCG 31

2.3.3 Sky subtraction on each CCD-image

As can be seen in Figure 2.5, the background values of each extension of a flat field corrected mosaic image are very different. The average background values differ by about 20%. This offset may be due to several amplifiers used. It further may be due to the arrangement of the CCD chips in the WFI instrument where it is not possible to arrange the chips at a perfect plane. The main reason may be the variation of the sky brightness in combination with the appropriate optics of the WFI.

The correction of gradients in the sky background is very important for mosaic data. If the sky is not flat (Figure 2.5) inhomogeneities in the combined images were received. In the following steps the background values of each extension have to be adjusted. The sky subtraction can be performed in two different ways, either using the common task `mcsksysub` or using `superflats`. Here both possibilities were checked.

2.3.3.1 Mscsky subtraction

The common method for aligning background values is the use of the task `mcsksysub` (`imsurfit`) which is offered in the `mscred` package. The automatic sky subtraction routine

mcskysub fits a surface function to a selected area on the image or to the whole CCD extension choosing a polynomial and the order for the x and y direction. Then the fitted sky is subtracted from each individual chip on each exposure. The output image may be the result of the fitted image or the difference between the input and the fitted image (**residual**).

In order to fit the sky background of the CCD image with **mcskysub**, with the aim to maintain gradients in the images in order not to eliminate the diffuse light of the group, the parameter **regions** had to be set to **sections** instead of **regions = all**. In this case not the whole CCD image was regarded, but small sections, which were previously defined. By testing the different fitting orders (xorder, yorder) of **mcskysub** the best result was obtained for a tilted plane, which corresponds to order **2**. All higher orders produced larger scale variations.

After processing the CCD extensions a uniform constant was added to each pixel, which was acquired before starting **mcskysub** using the task **imstat** in order to maintain the statistics.

The task **mcskysub** was run, setting the **type_out** parameter to **residual**, where the difference between the input image and the fitted sky was calculated. The residual output is the subtracted frame, but with the mean counting rate restored to effectively remove the sky patterns without changing the statistics. The background is therefore not zero after subtraction. There was no possibility to switch off this restoring. In the next step the task **mcskysub** was run with the parameter setting **type_out = fit**, where only the fitted sky was calculated. Figure 2.6 shows the result of this processing. Finally Figure 2.7 shows the difference between the image in Figure 2.5 and the **fit** output, which is shown in Figure 2.6.

It is clear that the results are not satisfying. The background values between the individual extensions differ between 15% and 20%. The results are not acceptably independent of the chosen function. It was not possible to eliminate the distinct gradients using the task **mcskysub**.

2.3.3.2 Super Flat

Using the task **mscred** (section 2.3.3.1) provided no satisfying results. Therefore it was tried to obtain better results by subtracting Super Flats from the object images. One important question arose: Why didn't the flatfield correction yield flat backgrounds? As mentioned before there were some important differences between the WFI mosaic CCD images and normal CCD images.

In the images some artefacts exist, which are not typical for CCD data with smaller fields of view. The large field of view of the mosaic in addition with the special optics to provide the large field leads to significant variations in the pixel scale. Thus the standard flat field calibration leads to a variation of the zero point. As this section will show, a calibration step using Super Flats can remove this effect.

Super Flats were created by combining object frames of the nights, which do not contain too many extended objects and their field is not too crowded. In this case each detector

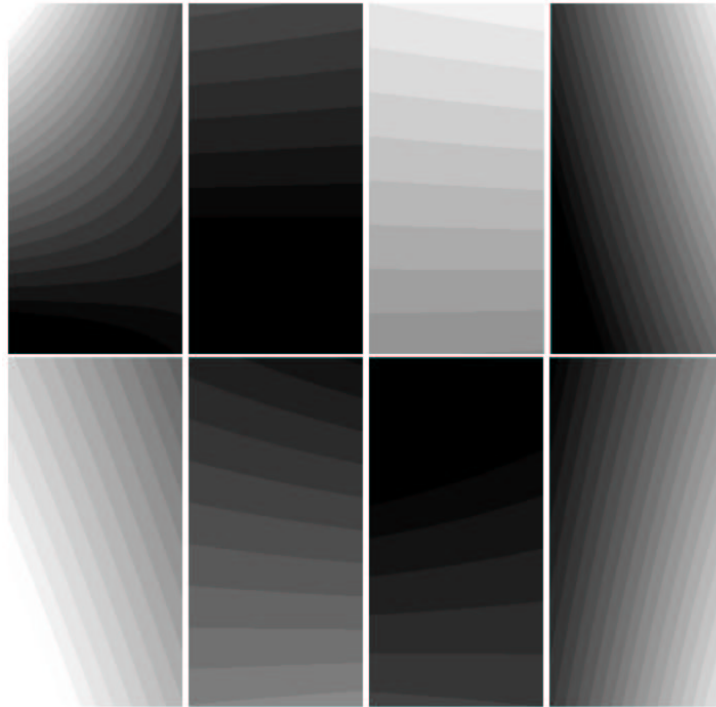


Figure 2.6: Result of the flat field corrected mosaic image (Figure 2.5) with `msc-skysub` and the output `fit`

pixel should map in most of the cases the sky background so that a combination of the images together with an appropriate clipping makes the extraction of the night sky possible using the median of the pixel values of the stack of object frames. This is done using the task `sflatcombine`, which is similar to the task `flatcombine`, which was used creating Master Flats but includes the parameter `grow`. The `grow` parameter of `sflatcombine` provides a rejection radius for all pixels that are thrown out of the combining process. All pixels around the pixels enclosed by the radius are rejected, too.

In this way scattered light from bright stars of the field or large extended objects was rejected. Figure 2.8 shows an example of such a derived Super Flat in the *B* band. As Super Flats were extracted from the science exposures they had to be scaled according to their mean values and applied as flat fields to the object frames. Figure 2.9 shows the object frame from Figure 2.5 corrected with the Super Flat.

The disadvantage of Super Flats is the poorer signal to noise ratio due to their appearance from object exposures. Hence, as many frames as possible were combined. The advantage of Super Flats is that they contain the true spectral characteristics of the nightsky thus errors concerning wavelength dependence of these effects could be avoided and Super Flats could be very well used for corrections concerning interference patterns due to night sky emission lines. To check the quality of the resulting images, the background levels of the eight CCD images of the extensions were averaged. The background values vary by less than 5%. Further the object frames corrected with Super Flats showed no gradients.

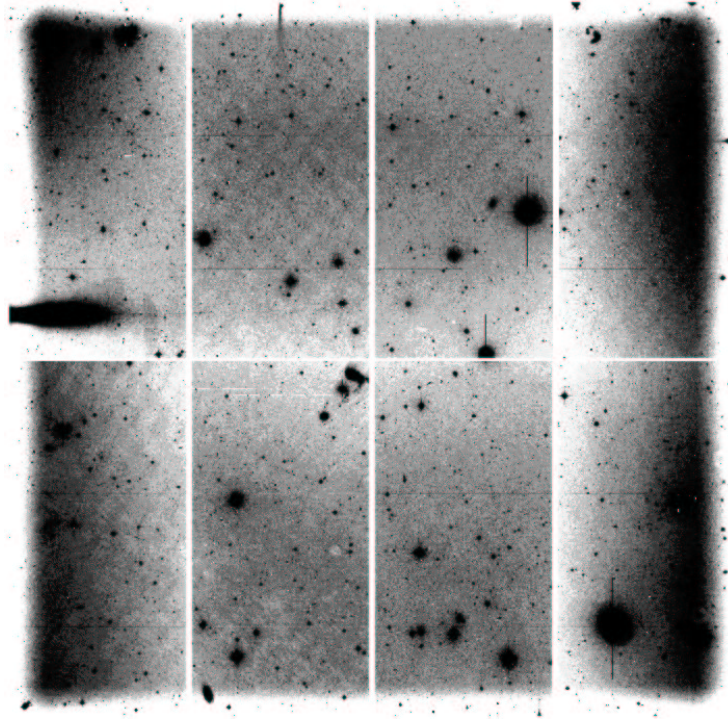


Figure 2.7: Difference between the flat field corrected image (Figure 2.5) and the fitted sky by `mcskysub` (Figure 2.6)

2.3.4 Coordinate calibration

While it is intended to combine multiple exposures of a dither set and while it is furthermore intended to obtain coordinate information, the celestial World Coordinate System (WCS) of the data has to be calibrated. This is necessary because the combination of the exposures refers to coordinates and not to the detector pixel.

First of all the coordinates had to be fixed to a zero point. A standard coordinate calibration is automatically inserted into the data during the observation which in general is accurately enough for many purposes. The astronomical calibration uses the WCS, which is registered in the header of each extension and transforms pixel coordinates of the mosaic data to celestial coordinates relative to a reference point on the sky. The reference point or zero point which is the same for all eight CCD images, is determined using the telescope pointing coordinates and lies on the optical axis of the telescope in the center of the detector area. In general the telescope's pointing is off by a small amount. The determination of coordinates of one star seen on each exposure of a dither set showed small but not negligible variations. Furthermore, atmospheric refraction can introduce axis scale changes and rotations, which are significant due to the large field of view of the mosaic. To compensate for these distortions the coordinate system was fixed to the stars in the frames. Fixing the coordinates in the dithered exposures first the zero point was checked and fixed for a set of screened exposures. In order to keep the error in the coordinate determination as

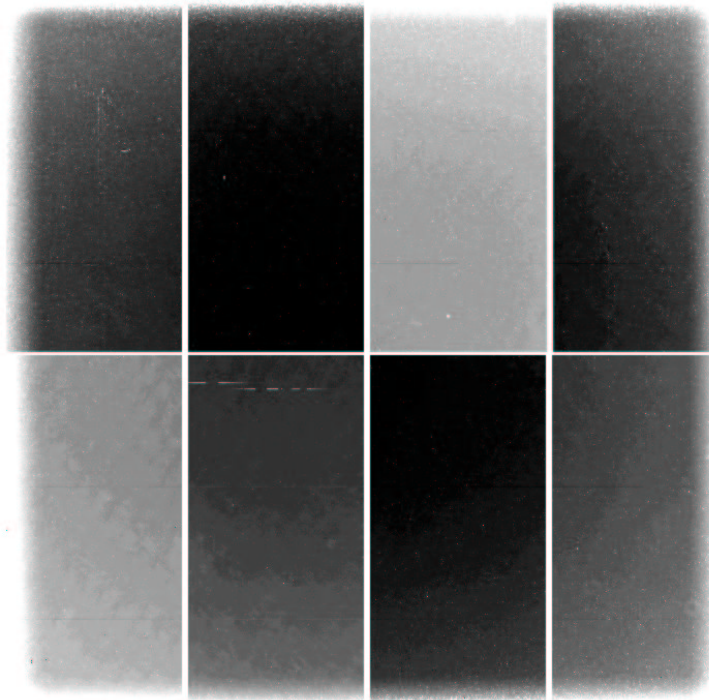


Figure 2.8: Super Flat in the B -band created out of all useful object images

small as possible, as reference exposure the one with the smallest seeing was chosen, if the seeing changes between the exposures in the dither set. By doing this, the task **msczero** was used to interactively fix the zero point of the coordinates system to a list of exposures. The zero points of all exposures of a screened set were all set to the same coordinates of a common reference star. Therefore a reasonable, bright, unsaturated star, which can be found in all exposures and whose coordinates are known by a catalog (e.g. Skycat⁶), were fixed.

Due to changes in the transparency of the sky, unequal intensity scales of the dithered exposures arose. Furthermore, the WCS in the dithered exposures may still not be registered across the whole field of view due to refraction effects. These two features are calibrated by matching stars throughout the field in position and brightness. This requires a list of coordinates tied to the reference exposures to which the other exposures were registered. The list should at least contain as many stars as possible from each CCD frame, desirably on the field edges. To be useful for intensity matching, stars should have an intermediate range of brightness and should be mostly isolated. Per mosaic image roughly 200 stars were chosen. Such a coordinate list was created using the task **msczero**. After choosing a star a centering algorithm starts and right ascension and declination of the calculated center is entered into the list.

Now the coordinate system could be aligned executing the task **mscmatch**, the geome-

⁶ ESO skycatalog tool

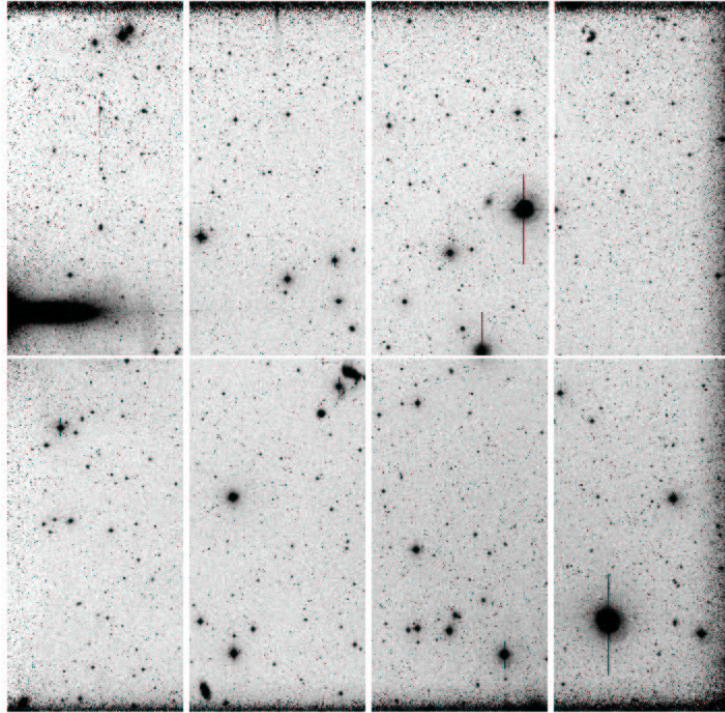


Figure 2.9: Flatfield corrected object image (Figure 2.5) corrected with the Super Flat (Figure 2.8)

try of the detector and optical distortions were considered while adjusting for changes in apparent sky position such as produced by atmospheric refraction and telescope position errors. The task matches the coordinate systems for all frames, which have to be combined. The input of **msscmatch** contains the list of mosaic exposures of a dither set and the file of reference celestial coordinates, which was created as described before.

The parameter **fitgeom** should be set to **rxyscale**, because the effects of atmospheric refraction actually do cause independent scale changes and rotations in the two axes. This parameter setting handles the x and y axis separately and they are changed linear. For an exposure it converts each input celestial coordinate to a pixel coordinate using the current WCS. In order to transfer the coordinates to the other frames an automated search looks for a good fit between the original celestial coordinates and the measured coordinates by shifting the zero point, scale changes in the right ascension and declination axis, stretching and rotation of the axes until enough star positions match. These parameters are then used to update the exposure WCS so that the adjusted measured coordinates best agree with the reference coordinates. Therefore the parameter **rms** gives the maximal fit RMS (Root Mean Square) to accept and represents a statistical measure for the deviation from zero. It is possible, that the fit fails, if the **rms** parameter is set too large, although the real shift is much smaller. Both values could be controlled interactively. In this case the coordinates needed a coordinate shift smaller than $2''$. In most cases the RMSs of the fits were below $0.2''$.

2.3.5 Creating individual images

After the coordinate transformation single images from each mosaic exposure were created by mapping all eight extensions from the MEF to a single fitsfile. Thus, one output image is created for each input mosaic exposure.

The pixels of each individual extension are joined to a consistent grid on the sky. In detail the multi extension mosaic exposures are resampled, based on the individual extension WCS with distortions and stored in a single image with a simple WCS, so that the images can be registered with integer pixel shifts. This includes a pixel mask, identifying regions of no data and pixels with contributions from bad pixels. The old pixels do not lie exactly on a pixel of the new image, thus it had to be defined how the light of an input pixel is distributed on the output pixel. This could be done by interpolating the light of the input pixel to the point, at which the center of the output pixel lies. This interpolation leads to a small smoothing of the images, because the output pixel are a combination of input pixel, which also implements negligible changes in the noise statistics.

The result is one mosaic image out of eight CCD images, which contains all information with the positions preserved.

This reduction step was necessary, because for combining multiple dithered exposures all images had to be registered to a common coordinate system and each exposure must be resampled to the same final coordinate system, so that they can be combined by simple integer shifts along the image axes (see section 2.3.7). Finally the header of the new images was modified by adding the new Read Out Noise and Gain, which were determined averaging the Read Out Noise and Gain values of the eight extensions automatically.

2.3.6 Adjusting intensity scales

When scaling dithered exposures to fill in the mosaic gaps and remove bad pixels and cosmic ray events, it is critical that the intensity scales of the images match. Using the task **mscismatch**, two scaling parameters were determined. The corrections for the sky brightness variations were calculated, which are due to differences in the illumination during the night and cause an additive offset. Additionally, the multiplicative scale change (the scale and zero offset) of the different images was determined, which is caused by transparency and exposure time variations. These parameters were defined by measuring the mean flux in some matching regions between each input image. For this reason **mscismatch** accomplishes a quick photometry using the coordinate list. Two quadratic boxes without a gap were defined. In the inner box the counts for the stars and in the outer box the counts of the background were determined. The measurement for i stars of two frames m_1 and m_2 are to satisfy the linear correlation:

$$I_{im_1} = a_{m_1m_2} \cdot I_{im_2} + b_{m_1m_2} \quad (2.4)$$

This relation ensures, that the scaling between two frames m_1 and m_2 corresponds to the scaling between the frames m_1 and m_3 . For all measurements the constant $a_{m_1m_2}$ and $b_{m_1m_2}$ were determined using a least square fit. In this way a linear fit between these values of the

reference image and a target image was computed. The task took measurements in all input images relative to a reference exposure and added the zero point offset and multiplicative scale factor to the image headers. These information were used when stacking the exposures (section 2.3.7). A variation of the extension of the boxes was relevant for a good fit and depended on the chosen star for the photometry. The errors were below 0.5%.

2.3.7 Final mosaic image

After single images of each of the dithered mosaic exposures were produced by the task **mscimage** (section 2.3.6), a final image was created using **mscstack**. This task combined the dithered images into a deep image excluding the gaps and artefacts, using integer pixel shifts based on the WCS and by averaging pixel values.

After the combination the header had to be modified concerning Read Out Noise and Gain, which was not done by **mscstack**. **mscstack** just chose the Read Out Noise and the Gain of the first exposure of a dither set. Thus these values had to be calculated and added to each header using IRAF scripts..

The effective Gain G_{eff} of the final mosaic images was determined as the product of the number of stacked exposures (N) and the average of the Gain values of the eight CCD images used:

$$G_{eff} = N \cdot Gain \quad (2.5)$$

and the effective Read Out Noise RON_{eff} was determined as the average of the Read Out Noise values of the eight CCD images used multiplied by the square root of N :

$$RON_{eff} = \sqrt{N} \cdot Gain \quad (2.6)$$

The header gives default information about the airmass at the beginning (“AIRMSTAR”) and at the end (“AIRMEND”) of the exposure, but the airmass at the mid-exposure of the stacked mosaic image is necessary. Thus the average of “AIRMSTAR” of the first exposure and “AIRMEND” of the last of the four stacked exposures was calculated.

Further the seeing was determined using the IRAF task **imexam**, which determines the Full Width at Half Maximum (FWHM) of the Point Spread Function (PSF) fitting Gaussian profiles to stars in the mosaic images. **imexam** yields to FWHM values in pixel thus these values were multiplied with the resolution of 0.238"/pixel and averaged. Table 2.2 shows the seeing values for all final mosaic images. The temporal spacing between the beginning and the end of a dither set was at least 100 minutes in the B band including the spacing between the subexposures which lay at about 3 min thus the seeing variations had to be checked. The seeing of the first and the last exposure of each dither set were compared and they showed variations of maximum 0.08" which could be neglected.

The following criteria determine the quality of the data. The data had to be flattened, the sky should be uniform and the WCS should be accurately registered. All these points were fulfilled for the data presented here.

To summarize, the data reduction had to cope with variable sky conditions, scattered light within a dither sequence and variable sky levels when combining dithered exposures. Variable sky levels arise from sky gradients, sky level differences between the CCDs and between the exposures. The flat field calibration removed most of the differences in sky levels between the CCDs. Best results were derived using Super Flats (section 2.3.3.2). The images in Figures 2.10 to 2.14 show the final mosaic images of HCG 16 in the B band and an exposure time of 5400s in total, HCG 19 in the R band and an exposure time of 2700s in total, HCG 30 in the B band and an exposure time of 5400s in total, HCG 31 in the B band and an exposure time of 5400s in total, HCG 42 in the R band and an exposure time of 2700s in total, composed of four sub exposures each.

In the center of each mosaic image the interacting original HCG galaxies can be seen.

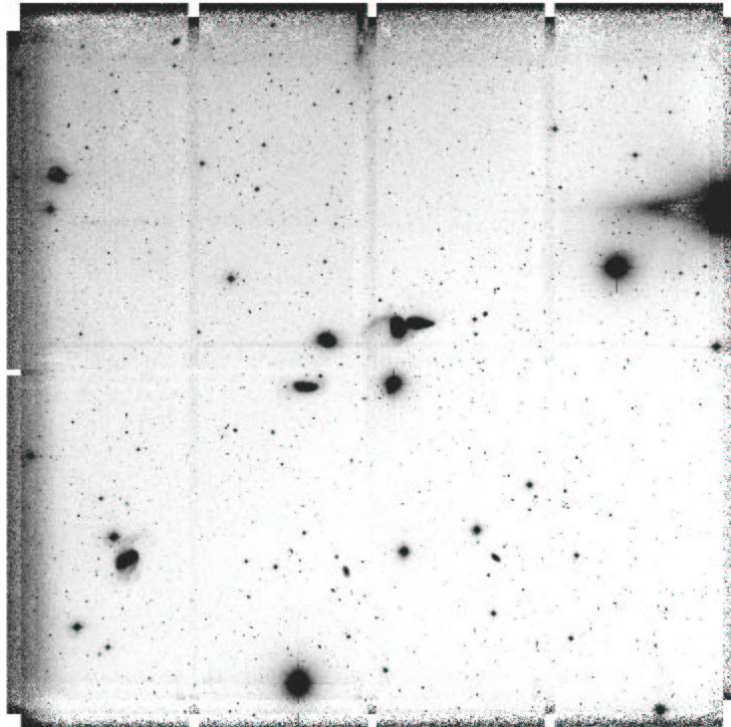


Figure 2.10: Final mosaic image of HCG 16 in the B band

2.4 Photometry

The described photometry in this section is applied to the study of dwarf galaxies. In the following the steps are described which were necessary to obtain instrumental magnitudes and to determine the transformations in order to calibrate magnitudes. The photometry is predominantly based on the 'User's Guide to Stellar CCD Photometry with IRAF' by Massey & Davis (1992). The **daophot** package under IRAF was mainly used. It is a package among the NOAO digiphot package, which was first developed by Stetson (1987)

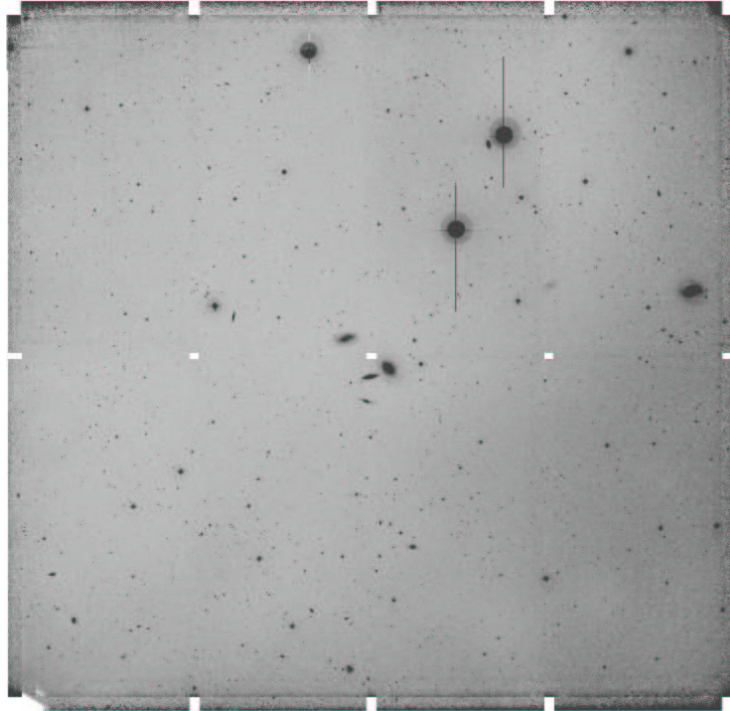


Figure 2.11: Final mosaic image of HCG 19 in the R band

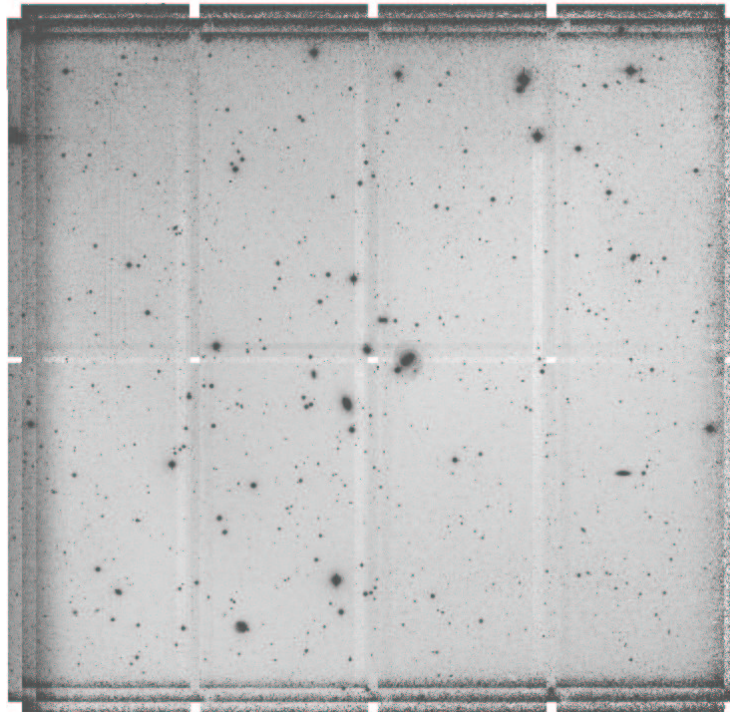


Figure 2.12: Final mosaic image of HCG 30 in the B band

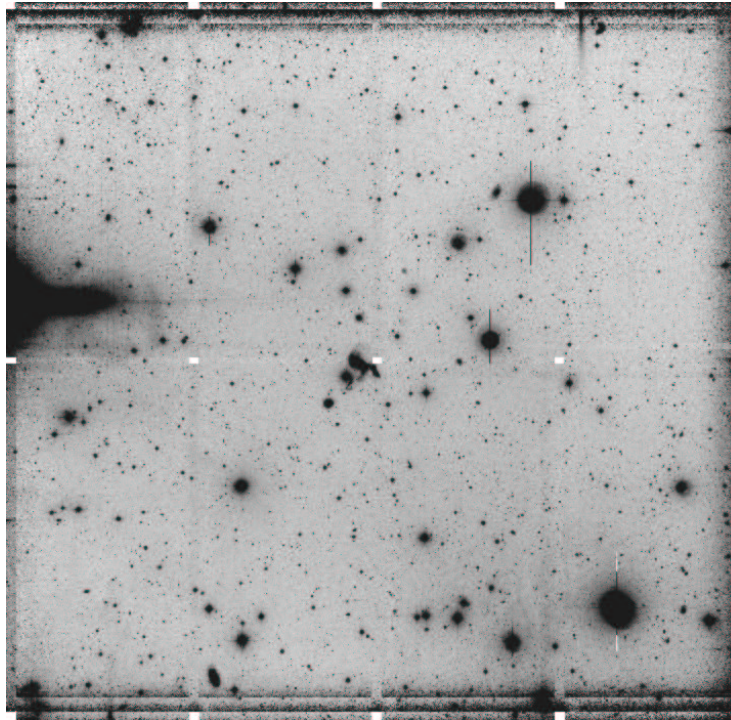


Figure 2.13: Final mosaic image of HCG 31 in the B band

at the Dominion Astrophysical Observatory (DAO). The instrumental magnitudes for all standard stars were obtained using aperture photometry. Next, the transformation from the instrumental to standard magnitudes were computed. After obtaining the instrumental magnitudes, the aperture correction for the program stars was determined. Finally, the transformation to program photometry was applied. Before using the task **phot**, which derives instrumental magnitudes for the standard stars, the parameter files **datapars**, **centerpars**, **fitskypars** and **photpars** had to be set. The task **datapars** specifies the properties of the data, which were necessary for the photometry. The most important parameters were the FWHM (**fw hm p s f**) of the stars and the information about the standard deviation of the background (**sigma**). Furthermore, the minimal (**datamin**) and maximal (**datamax**) data values have to be set. Except for the FWHM, all values were determined using the task **imexam**. The FWHM was determined by fitting a Gaussian to some star profiles and calculating the average of these values. As recommended by Massey & Davis (1992), **datamin** should be set to a negative value about three times the size of the Read Out Noise, in this case to -5. **datamax** should be set in order to use data which lie in the linearity range of the CCD. Furthermore, the Read Out Noise (**readnoise**) in electrons and the Gain (**epadu**) in photons per ADU, the exposure time keyword **exposure** to correct the results for the exposure time, and the keywords for **airmass** and **filter** had to be set. The task **centerpars** specifies the centering algorithm **calgorithm** to be used, which needs to be changed to **centroid**. If the FWHMs of the frames are usually large (≥ 4), one should rise the size of **cbox** to assure a well working centering ($2 \times \text{FWHM}$), as also recommended

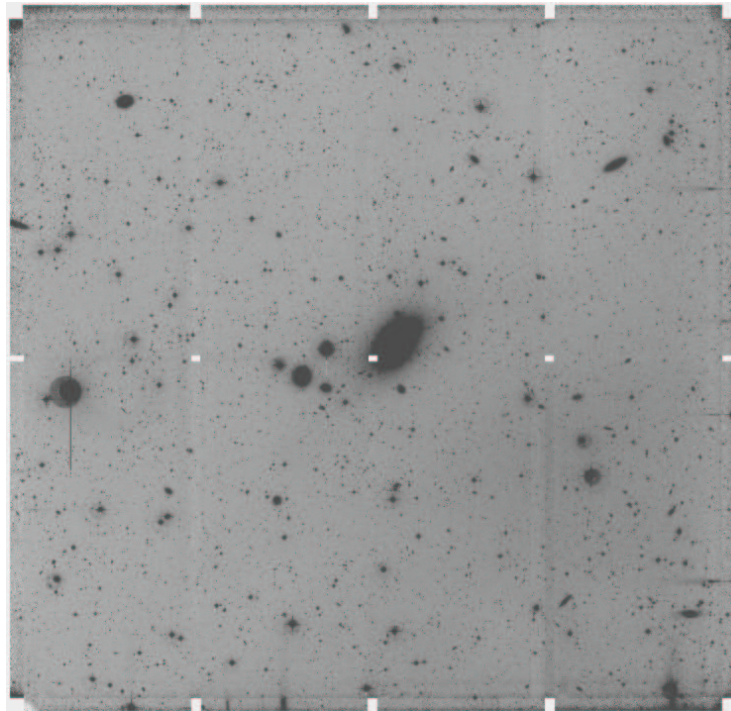


Figure 2.14: Final mosaic image of HCG 42 in the *R* band

by Massey & Davis (1992). Here the **cbox** was set to 8 pixel. **maxshift** should be set to 3. This is important while running **phot**, because this increases the allowable center of the shift by interactively selecting standard stars.

The task **fitskypars** contains e.g. the size and the location of the annulus and the radii of the annulus, in which the sky value was determined. The sky brightness was determined inside a circular area, which was limited by an inner and an outer radius, which were chosen not to include any light of the star. Therefore some star profiles were created and the radii at which the starlight disappears into the background noise were determined. A large width (5 pixel) of the annulus (**dannulus**) assures a good sampling as recommended by Massey & Davis (1992). Therefore the width of the ring was determined to be 5 pixel for all images.

The task **photpars** gives the size of the aperture within which the starlight was calculated using aperture photometry. The aperture should lie between 10 and 20 pixel. It should not be too small because then the seeing and guiding will play a role and it should not be too large, because then the probability of having a bad pixel rises. It was recommended by Massey & Davis (1992) to choose the radius to be four to five times the FWHM of a stellar image. In the reduction a radius of 20 pixels for all standards from all nights was used.

Selecting standard stars, the aperture photometry program **phot** was run on each standard star frame. By determining standard stars from each frame interactively, one received

a file of information for each frame. This file contained information e.g. about the sky, the integration time, the airmass, the filter, the size of the measuring aperture, the total number of counts within the aperture, area of the aperture, output magnitude, and the photometric errors. After obtaining the instrumental magnitudes for the standard stars the transformation equations that allow to put the observations on the standard system were determined. In this work the catalog of standard stars **nlandolt.dat** was used, which is based on the standard stars determined by Landolt (1992) and which is available in the IRAF package. It contains information about the magnitudes and the color indices. Per night on average two standard fields in each filter were available. On each field more than 15 standard stars could be found. In some cases two of the eight CCDs could not be covered by standard stars. However, the offset between the standard star field could solve this problem, so that all CCDs were covered by standard stars. In the next step a standard star observation file was created using the task **mknobsfile** that consists of the airmass, instrumental magnitudes, and errors of each set of observations. Therefore the parameters **photfile**, **idfilter**, **imsets**, and the **shifts** had to be set. The parameter **photfile** represents the output files of the previous task **phot**, where a file containing all the instrumental magnitudes was created. The parameter **imsets** represents the created file which includes the matched set of observations (in the B and R band). In the parameter **shifts** the shifts between the B and the R band image had to be defined.

There were two files created while running **mknobsfile**, one containing the data and one containing the format of the file.

The output file, which was defined in the parameter **observat**, created a datafile that gave consecutive enumerated names for each star which was found within the photometry file corresponding to the images listed. Here it was important to use the editor to change the real name of the standard star, so that the correct standard indices could be found in the catalog (**nlandolt**) during the next step of solving the transformation equation.

The second file, which was generated while the task **mknobsfile** ran, describes the format

night	z_B	k_B	z_R	k_R
n ₁	-26.943 ± 0.176	2.026 ± 0.140	-27.303 ± 0.152	2.518 ± 0.121
n ₂	-12.434 ± 0.038	-9.864 ± 0.129	-12.249 ± 0.012	-9.860 ± 0.130
n ₃	-12.494 ± 0.018	-10.542 ± 0.21	-12.239 ± 0.008	-10.569 ± 0.127
n ₄	-26.575 ± 0.436	1.725 ± 0.368	-26.923 ± 0.285	2.175 ± 0.240

Table 2.4: Solution of the transformation equations (2.7, 2.8); z_B , z_R are the zero points in the B and R band; k_B , k_R are the extinction coefficients in the B and R band

of the observations file. The content of this file is needed in setting up the transformation equation. With the photometric determination of the magnitudes of the standard stars, which were taken throughout each night and the cataloged magnitudes, one could find solutions for the transformation equations. Accurate zero points and air masses for the

night	mosaic image	magzero _{B,R}	magzero _{totalB,R}
n1	HCG16_B	-24.322±0.135	32.148±0.127
n2	HCG16_R	-25.055±0.142	30.928±0.091
n3	HCG19_B	-26.489±0.112	32.15±0.111
n3	HCG19_R	-23.970±0.131	31.243±0.123
n4	HCG30_B	-24.256±0.098	32.082±0.098
n4	HCG30_R	-24.414±0.139	31.390±0.132
n2	HCG31_B	-23.939±0.122	31.870±0.121
n1	HCG31_R	-23.668±0.132	30.640±0.095
n2	HCG42_B	-22.585±0.104	31.860±0.125
n1	HCG42_R	-24.683±0.143	30.930±0.138

Table 2.5: Magzero_{B,R} and magzero_{totalB,R} (equation 2.9 to 2.10) for each mosaic image

nights could be fitted then. The magnitudes of the standard stars (Landolt 1992) are implemented in IRAF as the catalog **n(ew)landolt**. The transformations were defined using the task **mkconfig**. To solve the transformation equations, a text file (**configuration**) had to be generated, which contains a description of the standard star catalog and definition of the variables. Then a description of the observations (containing the standard star air masses, instrumental magnitudes, and errors) was given, which corresponds to the output of the task **mkobsfile**. Finally, the algebraic form of the transformation equation (2.7, 2.8) was defined in the parameter **transform**.

$$m_B = ((B - V) + V) + z_B + k_B \cdot X_B \quad (2.7)$$

$$m_R = (V - (V - R)) + z_R + k_R \cdot X_R \quad (2.8)$$

with:

m_B, m_R : instrumental magnitudes

B, V, R : magnitudes of standard stars out of the IRAF catalog

z_B, z_R : zero point offset

k_B, k_R : extinction coefficient

X_B, X_R : airmass of the observation

Finally the transformation equations (2.7, 2.8) were fitted using the task **fitparams**. A solution was found interactively using a least square fit. The results of the fit of the transformation equation are listed in Table 2.4. The magzeropoint of each mosaic image was calculated using equation (2.9) and the results are listed in Table 2.5.

$$\text{magzero}_{B,R} = z_{B,R} + k_{B,R} \cdot X_{B,R} \quad (2.9)$$

The zero values, which are listed in Table 2.5 have to be scaled to an integration time of 1s in order to determine the final zero points. The final zero points are calculated using

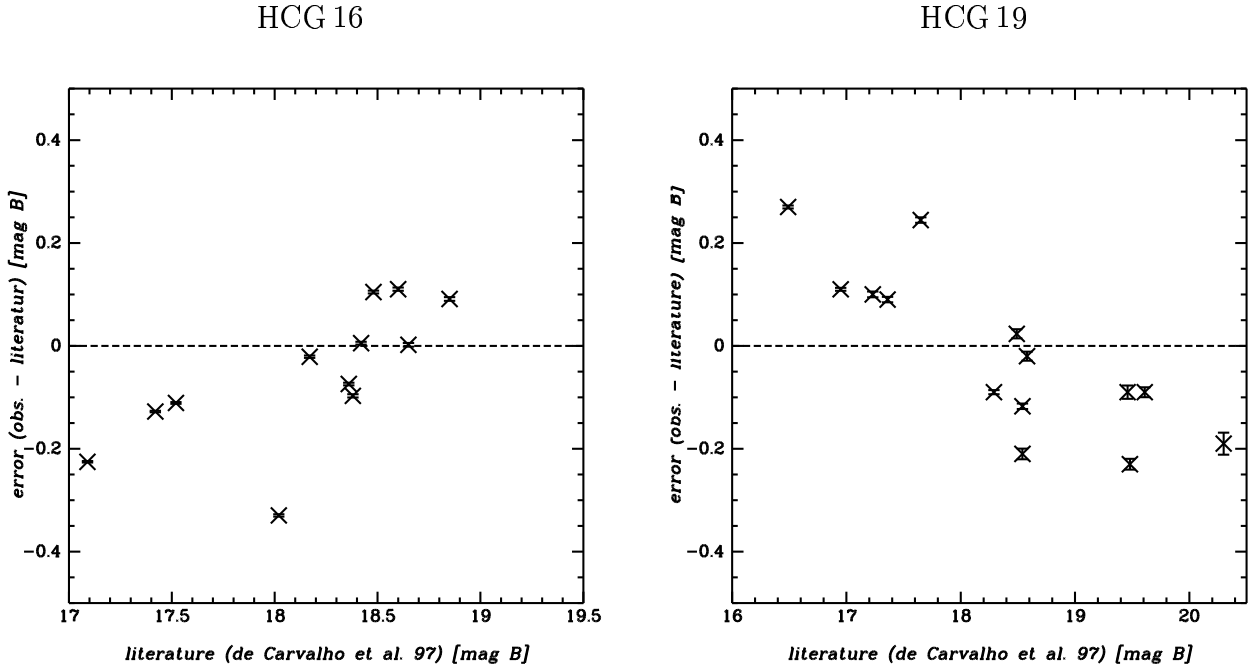


Figure 2.15: Comparison between literature and mosaic data for all galaxies of HCG 16 and 19 with known magnitudes from the literature

equation (2.10) and the results are listed in the last column of Table 2.5.

$$\text{magzero}_{\text{total } B,R} = -2.5\log(1/t) + z_{B,R} + k_{B,R} \cdot X_{B,R} = -2.5\log(1/t) + \text{magzero}_{B,R} \quad (2.10)$$

with t : total integration time of the mosaic image

The standard star calibration provided magnitudes with RMS random errors of $\delta \text{ mag} \sim 0.03$ in the B and $\delta \text{ mag} \sim 0.025$ in the R band. In order to check the quality of the photometry the literature values were compared with the magnitudes extracted from the mosaic images of all galaxies for which literature values were available. Figure 2.15 shows this comparison for all galaxies identified in HCG 16 and 19 for which literature data were available. The horizontal axis denotes the magnitude data of the galaxies and the vertical axis the difference between the literature data and the measured magnitudes. It can be seen that these values deviate by maximally 0.3 mag. In the next chapter it will be shown, that this difference will not influence the following data reduction, though the position of galaxies in the CMD is important. However, concerning further assumptions and calculations these differences are taken into account.

2.5 Detection of dwarf galaxies

For further investigation of the mosaic images (searching for dwarf galaxies using Source Extractor), the usefulness of the mosaic images had to be checked, which was done using **imexam**. Thereby the 'FLUX' and the 'PEAK' as well as the ellipticity 'E' and 'MOFFAT', which gives the information how good the point spread function can be fitted to the stars, were examined. Crucial is the study of the border areas of the mosaic images. In case stars show ellipticities this is due to the bow in the image area and maybe due to different levels of the CCDs. If these effects are too strong, this areas have to be excluded. From mosaic data presented here a sample of stars were selected especially in the outer regions and their ellipticity was determined. The stars showed ellipticities, which are smaller than 7%.

2.5.1 The Source Extractor program

The reduced mosaic images were examined concerning the content of dwarf galaxies using the program Source Extractor (Bertin 2001, Bertin & Arnouts 1996), which enables the reduction of large scale galaxy survey data by creating a catalog of objects from the images. The program works in three main detection steps. First the sky background is estimated by creating a model of the sky background and by subtracting the background from the image. The image is also filtered and thresholded. After that the detected objects are deblended, photometered, and classified. The star galaxy separation is performed and finally the detected objects are written to an output catalog. The most important advantage of the techniques used by Source Extractor is that the morphology of the objects is still defined. Before starting the program, two parameter files had to be edited (**default.sex** and **default.param**). The parameter file **default.sex** describes the configuration parameters and **default.param** gives the list of output options.

Some of the parameters of the configuration file **default.sex** were used with their default values. Some had to be optimized in order to find the maximum number of dwarf galaxies (low surface brightness and small objects). These are the DETECT_MINAREA, the DETECT_THRESHOLD, the BACK_SIZE and the BACK_FILTERSIZE parameters.

For the photometry the GAIN, PIXEL_SCALE and the MAG_ZEROPOINT were set. Except for aperture and isophotal magnitudes, Source Extractor has the possibility to determine total magnitudes of the objects. Two types of total magnitudes are possible, one using adaptive aperture and one using an isophotal correction (for detailed information see Bertin & Arnouts (1996)). The GAIN was set to 8.48 [e⁻/ADU]. The PIXEL_SCALE, which defines the size of the pixel in arcsec is 0.23 for the mosaic data. The values for the magnitude zero-point offset (MAG_ZEROPOINT), which had to be applied to the magnitudes was defined in section 2.4.

For the purpose in this work a good star/galaxy separation is very important. Therefore the seeing, which depends on the mosaic image had to be accurately determined and the SEEING_FWHM parameter had to be set. The FWHM of the stellar images, which is

necessary for the star/galaxy separation (see Table 2.2) was set in [arcsec].

In order to detect faintest objects, a very good background level is necessary. As in general no flat background level exists, one background map per object had to be created. Source Extractor makes a pass through the pixel data and computes the local background in each mesh of a grid, which covers the image frame. If the grid is accomplished, the median filter can operate on it with the aim to mask local overestimations.

For the background investigation the parameters `BACK_SIZE` and `BACK_FILTERSIZE` had to be set.

The `BACK_SIZE` defines the size of the background mash. As mentioned by Bertin (2001), the choice of the mesh size (`BACK_SIZE`) is important, because if it is too small, the background estimation is affected by the presence of object and random noise. In the background map part of the flux of the most extended objects can be absorbed in the background map. With mesh sizes too large, it is not possible to reproduce small scale variations of the background. Bertin (2001) recommends a size of 32 to 256 pixels. By varying the parameters, best results (most galaxies and the galaxies with the lowest surface brightness) were obtained by setting them to 64 pixel. The `BACK_FILTERSIZE` defines the size of the background filtering mask in background meshes. By specifying the size of the median filter (`BACK_FILTERSIZE`), the user has control over the background map. Setting the width and hight to one, no filtering will be applied to the background grid. As recommended by Bertin (2001), a size of 3×3 is usually enough, but it may be necessary to use larger dimensions, for example to compensate for small background mesh sizes. In this case it was necessary to use larger dimensions, a `BACK_FILTERSIZE` of 5 led to best results.

After the background map had been created the program searches for pixels, which are connected and which lie above a given threshold. The detectability is generally limited at the faintest flux level by the background noise. In order to receive ideal results, the parameters `DETECT_MINAREA` and `DETECT_THRESH` had to be specified: the `DETECT_MINAREA` defines the minimum number of connected pixels required, which lie above the threshold. Bertin (2001) recommended a `DETECT_MINAREA` of 5, but studies conducted best results using a `DETECT_MINAREA` of 10. As recommended by Bertin (2001), the typical values for the `DETECT_THRESH` lie between 1.0 and 2.0 mag/arcsec². The `DETECT_THRESH` was set at 1.1σ above the local background.

Using Source Extractor both stars and galaxies were detected. A detection threshold of 1.1σ above the sky was used to find modestly faint and low surface brightness galaxies. Due to the parameter settings the brightest galaxies were not detected.

Source Extractor offers a large fraction of useful output parameters, for more information see Bertin (2001). As mentioned by Bertin (2001), the automatic aperture magnitudes give the best total magnitudes at least for galaxies. The most important output parameters are `MAG_AUTO`, `MAG_ISOCOR` and `MAG_BEST`. As the aperture magnitudes are sensitive to crowding, the aperture magnitudes `MAG_AUTO` are replaced by the corrected isophotal magnitude `MAG_ISOCOR` when the object is too close to its neighbors. The program performs this automatically while using `MAG_BEST`. As recommended by Bertin (2001)

HCG	D [h^{-1} Mpc]	x [$''$]	R_G [pixel]
16	39.6	2.22	5
19	42.3	2.07	4
30	46.2	1.91	4
31	40.9	2.15	5
42	39.9	2.21	5

Table 2.6: Diameter (x) and Radius (R_G) of the smallest Local Group galaxy at the distance (D) of the corresponding HCG

very precise photometry with Source Extractor is possible. Purpose of Source Extractor magnitudes is to obtain photometry of faint sources with the lowest error. For bright objects, MAG_ISOCOR, MAG_AUTO and MAG_BEST magnitudes do not permit to go beyond $\approx 1\%$ in photometric accuracy. They contain a systematic offset compared to “true” total magnitudes of about 0.05 mag.

2.5.2 Selection criteria

After the sky was subtracted, all objects with a threshold $\geq 1.1\sigma$ in B (27 mag/arcsec²) and $\geq 1.1\sigma$ in R (26 mag/arcsec²) above the sky level were extracted. The photometry of all selected objects was done using elliptical apertures. The program Source Extractor lists all detections, stars and galaxies, large and small objects (number of detected objects see: Table 2.7; column (2)). As it was intended to search for dwarf galaxies in the fields, the following steps had to be acquired. The photometry was performed using elliptical apertures and as mentioned by Bertin & Arnouts (1996) the total magnitudes were obtained using Kron’s “first moment” algorithm $r_1 = \sum rI(r) / \sum I(r)$ Kron (1980).

The following selections have been accomplished:

First all objects in the B and R band were excluded, which have an magnitude error larger than 0.1 (MAGERR_BEST < 0.1; number of objects see Table 2.7; column (3)).

Then the galaxies were separated from the stars using the image morphology - starlike - non starlike. The seeing and the limited SNR make the distinction between faint point sources and extended objects difficult. Galaxies are defined with CLASS_STAR = 0 and stars are defined with CLASS_STAR = 1. By checking the classification results, all stars with CLASS_STAR larger than 0.1 were excluded (number of galaxies listed in Table 2.7; column (4)). Thus objects remained, which are galaxies at high probability. Therefore a stellarity index of ≤ 0.1 was used.

With the following selection criterion, all small galaxies were excluded which are smaller than the smallest identified dwarf galaxy (570 pc) of the Local Group (number of objects listed in Table 2.7, column(5)). Therefore first the radius (R_G) of this galaxy at the dis-

name	all identified obj.	MAG_ERR < 0.1	CLASS_STAR < 0.1	$\theta_{lim} \geq x''$	merged <i>B</i> & <i>R</i> images
(1)	(2)	(3)	(4)	(5)	(6)
HCG 16 <i>B</i>	177555	62438	1495	725	415
HCG 16 <i>R</i>	155912	43458	2860	904	
HCG 19 <i>B</i>	193733	63952	273	251	212
HCG 19 <i>R</i>	174900	50509	4911	1698	
HCG 30 <i>B</i>	202431	65464	303	288	219
HCG 30 <i>R</i>	149779	43811	672	626	
HCG 31 <i>B</i>	140513	49207	4788	1038	470
HCG 31 <i>R</i>	116736	38448	5161	1312	
HCG 42 <i>B</i>	178304	71588	500	313	252
HCG 42 <i>R</i>	132221	45864	4298	2701	

Table 2.7: Number of identified objects in the mosaic images; column (2) shows all identified objects (stars and galaxies); column (3) lists all objects (stars & galaxies) smaller than an error of 0.1 mag; column (4) shows all identified galaxies; column (5) shows all identified galaxies larger than the smallest local group galaxy; column (6) shows all galaxies, which were identified in both filter bands.

tance of the corresponding HCG was calculated (Table 2.6). The further selection was performed using θ_{lim} . At the distances of *D* dwarf galaxies, larger than the smallest dwarf galaxy represented in the Local Group, have apparent sizes larger than $2 R_G$ at the outer surface limit of $\mu_R \sim 26 \text{ mag/arcsec}^2$. Galaxies with a limiting angular diameter larger than $2 R_G$ at a given isophotal level were selected. The limiting parameter for constant luminosity and μ_{lim} is expressed by equation (2.11) (Allen & Shu, 1979) which gives a maximum value for $\mu_{lim} - \mu_0 = 2.17$ for the disks of spirals and dEs.

$$\theta_{lim} = 0.7349 \cdot (\mu_{lim} - \mu_0) \cdot 10^{0.2(\mu_0 - m_{tot})} \quad (2.11)$$

with $\mu_0 = \text{MU_MAX}$: extrapolated central surface brightness,
 $\mu_{lim} = \text{MU_THRESHOLD}$: surface brightness at the limiting isophote,
 $m_{tot} = \text{MAG_BEST}$: total magnitude of the object

The comparison between the CMDs prepared with galaxies selected by “A_IMAGE > R_G or B_IMAGE > R_G ” and galaxies selected by “ $\theta_{lim} \geq 2 R_G$ ” give identical results. If the limit given by $2 R_G$ is enlarged the faint galaxies were systematically excluded as expected. Finally the catalogs in both filters were matched in order to obtain color information for objects in both filters. The lists, which were received from Source Extractor are now merged in order to extract objects which were detected in the *B* and in the *R* band (number of dwarf galaxy candidates listed in Table 2.7; column(6)).

2.5.3 Radial light profiles and isophotal fits

This chapter describes how the galaxies, which were identified in the red sequence (chapter 3), were analyzed using the ELLIPSE routine in the STSDAS package inside IRAF. The task **ellipse** fits elliptical isophotes to galaxy images. For that purpose it reads two-dimensional image sections and produces a table with parameters for each fitted isophote. The image is measured by using the Fourier prescription, which is described by Jedrzejewski (1987). Each isophote is fitted at a defined and fixed major axis length. The task starts from an elliptical isophote, which was defined by approximate values for the x and y center coordinates, ellipticity and position angle. Using the values, the image is scanned along an elliptical path and produces an one-dimensional intensity distribution as function of the position angle α . The Fourier decomposition of the intensity distributions is

$$I(\alpha, r) = I_0 + \sum_{i=1}^4 (A_i \sin(i\alpha) + B_i \cos(i\alpha)) \quad (2.12)$$

α is the position angle at each fitted semi major length r . A_1, A_2, B_1, B_2 are the harmonic amplitudes, which are related to a specific ellipse geometric parameter and A_3, B_3, A_4, B_4 are the amplitudes, which are divided by the semi-major axis length and the local intensity gradient. They measure deviations of the isophotes from perfect ellipticity. The task **ellipse** measures the integrated intensity and the number of non-flagged pixels inside the elliptical isophote and also inside the corresponding circle with the same center and radius equal to the semi-major axis length. All parameters are written to the output table. After fitting the ellipse, which corresponds to a given value of the semi-major axis, the axis length is incremented or decremented. The starting ellipse parameters are taken from the previous ellipse, which has the closest semi-major axis to the current. The errors in intensity, magnitude, and local gradient are obtained from the RMS scatter of intensity data along the fitted ellipse. The errors of the ellipse geometry parameters are obtained from the internal errors in the harmonic fit after the first and second fitted harmonic had been removed. The errors of the harmonic amplitude were obtained from the fit error after all harmonics were removed. For more information see Busko (1996). The task **isomap** draws the image contours map and overlays ellipses on it according to intensity levels. The ellipse data are taken from the table which was created by the task **ellipse**. The ellipses created by the task **isomap** for each galaxy can be seen in column (2) of Figure A.1 to A.5.

The task **isoplot** shows the results from the isophote fitting task **ellipse**. The abscissa shows the semi-major axis length in pixel and the ordinate the total flux, which is enclosed by the ellipse. Column (3) in the images of Figure A.1 to A.5 shows the isoplots for the selected galaxies. The first column of Figures A.1 to A.5 shows the images of the galaxy candidates, each image has a size of 100×100 pixel ($23.3'' \times 23.3''$). Each galaxy is labeled with the name of the dwarf galaxy candidate, which was given by Source Extractor. In cases where it was not easy to distinguish between background galaxy and high probability member galaxy, all information were taken into account, especially the error information, which were offered by the task **isopall**.

Chapter 3

Analysis and results

3.1 Selection criteria for group membership

The determination of group membership is a common problem when studying the faint galaxy populations in clusters and groups. The most reliable method of taking spectra to determine redshifts for all candidates is a very telescope-time consuming task and is also limited to the brighter galaxies (Zabludoff & Mulchaey 1998b). All studies conducted up to now concerning dwarf galaxies in CGs have problems to distinguish between real dwarf galaxies and other unrelated background galaxies. The latter may be a significant contribution due to the relative sparseness inherent to the CGs. Also for this study of the population of dwarf galaxies in CGs, one is confronted with the difficult task of determining group membership in order to ensure that each sample contains only galaxies which belong to the respective group. Therefore a method was developed to determine the group membership of the galaxies from a preselection using a Color Magnitude Diagram (CMD) and from a following detailed inspection of the morphology, the isophotes, and the radial light profile of the individual galaxies. Furthermore, statistical methods involving the density distribution within the groups allowed further proof.

3.1.1 Dwarf galaxies and the Color Magnitude Diagram

This section gives a detailed description how it is possible to distinguish between dE belonging to the group and background galaxies in the absence of redshift information. In this work for the first time CMDs are used in order to preselect dwarf galaxy members in compact galaxy groups. The investigation of galaxy clusters shows that dE galaxies dominate a certain area in the CMD.

Secker & Harris (1997) plotted CMDs for 3723 objects of three fields of the Coma Cluster core added together (Figure 3.1 left diagram) and 1164 objects of a control field which is located 2 degrees east of the cluster center (Figure 3.1 right diagram). In the left diagram of Figure 3.1 the dE galaxy sequence (red sequence) is densely populated and it dominates the region restricted to $0.7 \leq B - R \leq 1.9$ mag (dotted vertical lines), which is absent in the CMD of the control field. 2526 objects lie within the restricted color range of the

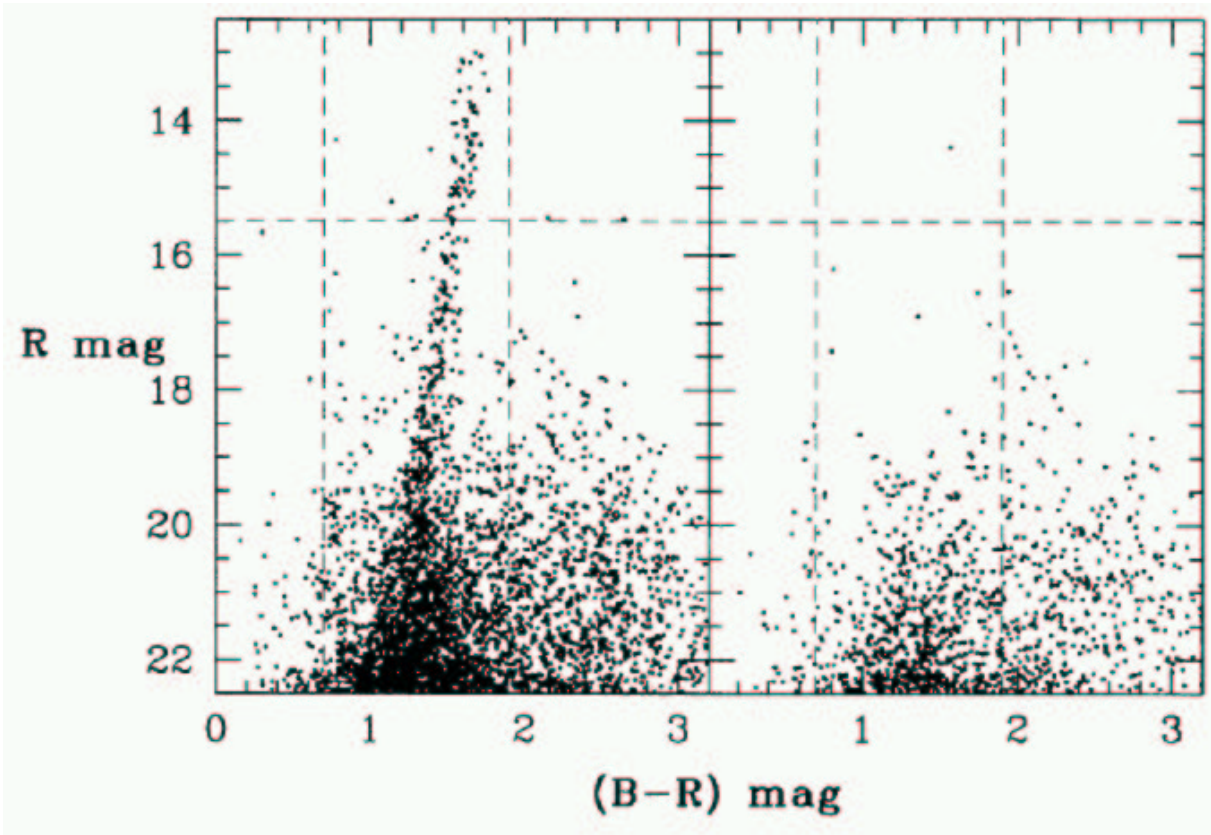


Figure 3.1: Left: CMD for 3723 objects identified on three fields of the Coma Cluster core; right: CMD for 1164 objects of a control field. The vertical dotted lines denote the restricted color range – the dE galaxy sequence. Within the restricted color range 2526 objects lie in the left diagram and 694 objects in the right CMD. The horizontal line at 15.5 mag denotes the beginning of the dE galaxy sequence. (Secker et al. 1997)

Coma Cluster core and 694 in the restricted color range of the control field.

The dE galaxy sequence starts at about 15.5 mag (horizontal line) with a mean color of $B - R \simeq 1.54$ mag (Secker & Harris 1997). The red sequence shows a trend to bluer colors for fainter dEs. Secker et al. (1997) determined a color–magnitude relation for the dE galaxies considering the bright part of the galaxy sequence and performing a least–square fit of a straight line to the median color values. The relation between apparent magnitude and color is:

$$(B - R) = (-0.056 \pm 0.002)R + (2.41 \pm 0.04) \quad (3.1)$$

Concelice et al. (2002) found this structure in the Perseus Cluster CMD, too, and they estimated the following relation between absolute magnitude and color:

$$(B - R)_0 = (-0.055 \pm 0.009)R_0 + (0.456 \pm 0.16) \quad (3.2)$$

For comparison Conselice et al. (2002) converted the relation found by Secker & Harris (1997) (equation 3.1) into an absolute magnitude relation:

$$(B - R)_0 = (-0.056)R_0 + 0.452 \quad (3.3)$$

They found that the two clusters have identical dE galaxy sequences within the errors. Also the photometry of bright elliptical galaxies in clusters reveals a very well defined correlation between magnitude and color, which varies just little between nearby clusters (e.g. Bower et al. 1992, Kormendy 1977). The color restrictions in the CMD Figure 3.1 represent the limits of the early-type galaxy sequence. High probability cluster members can be extracted while excluding red background galaxies from the sample. Furthermore the color of the dE sequence is in accordance with colors found for Coma cluster dEs (Thompson & Gregory 1993) and also with the integrated colors of globular star clusters (Hopp et al. 1995).

The $(B - R)$ color index is an estimator of the metallicity for old stellar populations (Held & Mould 1994, Couture et al. 1991, 1990, Geisler & Forte 1990). While age and metallicity influence absorption features in the spectra of stellar populations, the effect of metal abundance dominates over ages effects in the $(B - R)$ color of old populations like dEs. Thus the redder elliptical galaxies are more metal rich than the bluer galaxies (e.g. Vazdekis et al. 2001, Kauffmann & Charlot 1998, Larson 1974). The trend of color with magnitude that fainter dEs are bluer and presumably more metal poor was explained by Secker et al. (1997). They argued, that the brighter dE galaxies have deeper gravitational potentials and thus they are able to retain their interstellar gas, which became metal enriched and heated during star formation.

dE and nucleated dwarf elliptical (dE, N) galaxies are most numerous in the center of all rich clusters (Ferguson & Binggeli 1994, Ferguson & Sandage 1991, Dressler 1980). If a bound system exists, dEs dominate the red sequence of the CMD. However, compared to the CMD of dwarf galaxies in the Coma and Perseus Cluster no well defined sequence of dE galaxies is found in the sparse HCGs, which was expected to be seen in the color range between 1 and 2 mag. The missing red sequence may be the effect of small number statistics.

The CMDs of galaxies found in the $0.^{\circ}54 \times 0.^{\circ}57$ field around HCG 16, 19, 30, 31, and 42 are shown in Figure 3.2–3.6, the abscissa shows the $(B - R)$ color index and the ordinate the R brightness. All symbols except the pentagons represent the dwarf galaxy candidates. Some of them (red triangles) were identified as group members by their radial velocity and some (green triangles) were identified as background galaxies. The pentagons represent the original HCG galaxies. The dashed lines represent the red sequence defined by Conselice et al. (2002) and Secker et al. (1997) and its 1σ errors. The galaxies in the red-sequence (inside the dashed lines) are probable dEs of the HCGs. In this area a large number of galaxies (147 in HCG 16, 51 in HCG 19, 90 in HCG 30, 152 in HCG 31 and 132 in HCG 42) was found and also some spectroscopically (e.g. de Carvalho et al. 1997) identified background galaxies (green triangles).

Bluer than the red sequence are few galaxies. It is very unlikely, that these galaxies are background galaxies because if they are undergoing star formation at higher redshifts they

would not be as blue as these galaxies, because of the k corrections. These galaxies are also unlikely foreground galaxies, because then a lot of field dwarfs would exist. Therefore these galaxies represent dIrr candidates.

The fact that the red sequence is redshift dependent moving redwards for higher redshifted galaxy groups is taken into account. As the HCG sample is even closer than the Perseus and Coma Cluster for which the red sequence was determined (equation 3.2 and 3.3), a reliable method is used investigating all galaxies bluer than 1.9 mag (vertical line in Figure 3.1).

3.1.2 Extraction of dwarf galaxies

As a second step, the candidate galaxies' morphology, surface brightness, and the radial profile were examined for further information, since structural parameters can reveal a lot about the evolutionary state of a galaxy (e.g. Conselice et al. 2003, 2001, Conselice 1997, Abraham et al. 1994). This was possible due to the very good resolution, good pixel sampling and seeing in the ESO/MPIA 2.2 m WFI data (see chapter 2). As mentioned by Conselice et al. (2002) the morphological classification of galaxies is more reliable than one might think at the first sight. More than 90 % of galaxies, which were morphologically identified as cluster members, were afterwards spectroscopically confirmed as members (e.g. Drinkwater et al. 2000, Binggeli et al. 1993). Up to now no CGs exist for which velocities were determined for all galaxies including the faintest galaxies.

The following criteria, of which some were already successfully used to distinguish between cluster members and background galaxies (e.g. Conselice et al. 2003, 2002, 2001, Secker & Harris 1997), were used to distinguish between group members and background galaxies: First of all as described in section 2.5.2 a minimum size limit of 570 pc (extension of the smallest Local Group galaxy, Mateo 1998) was chosen at the distance of each compact group. Galaxies which are smaller than this limit are probably background galaxies.

All galaxies, which lie in the red sequence area (equation 3.1– 3.3 and its 1σ error) are high probability dwarf galaxy candidates. However, they need to be further investigated, since some spectroscopically identified background galaxies were also found in this area (green triangles in Figures 3.2, 3.3, 3.5 and 3.6). All galaxies, which are redder than the red sequence were excluded because they are very probably background galaxies, also very few spectroscopically identified member galaxies lie in this area (red triangles in Figure 3.2 3.3 and 3.6). Each galaxy in the red sequence of the CMD was examined concerning their morphology, isophotes, and radial light profiles and then they were separated into four morphological types: background bright elliptical galaxies, background spirals seen face-on, background spirals seen edge-on, and the member dE galaxies (selection examples: Figures A.1–A.5).

For this classification the galaxies' radial light profiles were examined and elliptical isophotes to each galaxy image of the red sequence were fitted using the Fourier prescription of Jedrzejewski (1987), which is implemented by the ELLIPSE routine in STSDAS as described in section 2.5.3. For each surface brightness profile $I(r)$ a general Sérsic profile of the form

$$I(r) = I_0 e^{-\kappa(r/r_e)^{1/n}} \quad (3.4)$$

can be used to describe the light distribution $I(r)$ which is the intensity of an isophote at r , I_0 is the central intensity, r_e is the effective or half light radius, and κ a parameter depending on n . The value of $n = 1$ is for pure exponential profiles and $n = 4$ is the de Vaucouleurs profile, which is more strongly peaked at the center than the exponential. Light profiles of giant ellipticals can be very well fitted by the $r^{1/4}$ de Vaucouleurs profile. Background giant elliptical galaxies are also characterized by a high surface brightness and they are mostly ellipsoidal. Figure A.1 shows typical examples of galaxies which were selected as background elliptical galaxies in HCG 16. The elliptical galaxy in the first row was identified by de Carvalho et al. (1997). The galaxy in the second row was identified in the red sequence of the CMD of HCG 16.

Spiral galaxies show disks or spiral patterns and their isophotes are twisted. Furthermore their radial profiles show a break from $r^{1/4}$ to an exponential law. Figure A.3 shows typical examples of spiral galaxies seen face-on. The first two rows show spiral galaxies which were identified spectroscopically by de Carvalho et al. (1997). The last two rows show spiral galaxies, which were identified in the red sequence of the CMD of HCG 16. Spiral features (first column), twisted isophotes (second column) and a break from a $r^{1/4}$ to an exponential law in the radial light profile (third column) can be seen in all images. Figure A.2 shows typical examples of spiral galaxies seen edge-on. All these galaxies were rejected from the candidates' sample.

Investigations of faint galaxies in galaxy clusters as well as the dSph galaxies in the Local Group found, that they show exponential light profiles. Conselice et al. (2003) could fit exponential profiles to the early type dwarf galaxies, which they selected by morphology and color as cluster members similar to dEs. If the galaxies showed elliptical, round, and symmetric shapes without any structures such as spiral arms, they were classified as dEs. The dEs have a low surface brightness and they show an exponential light profile. Thus dEs can be distinguished from giant elliptical galaxies. Figures A.4 and A.5 show some of the high probability member galaxies, which were selected due to their morphology (first column), their isophotes (second column), and their exponential light profile (third column). The isophotes of the high probability dwarf galaxies are elliptical/symmetric and show no signs of distortions. Due to cosmological dimming high z galaxies have low surface brightnesses, but they do not show smooth elliptical structures and they further have no exponential light profiles thus it was possible to distinguish faint group members from background galaxies. Objects, which did not meet any of these criteria were excluded as background galaxies.

3.2 Results from the selection process

3.2.1 Results HCG 16

HCG 16 was identified by its four late-type galaxies. These galaxies show signs of interaction and further have comparable luminosities. Two of these galaxies (NGC 835 and NGC 833) are very close showing prominent tidal distortions. Three of these galaxies have

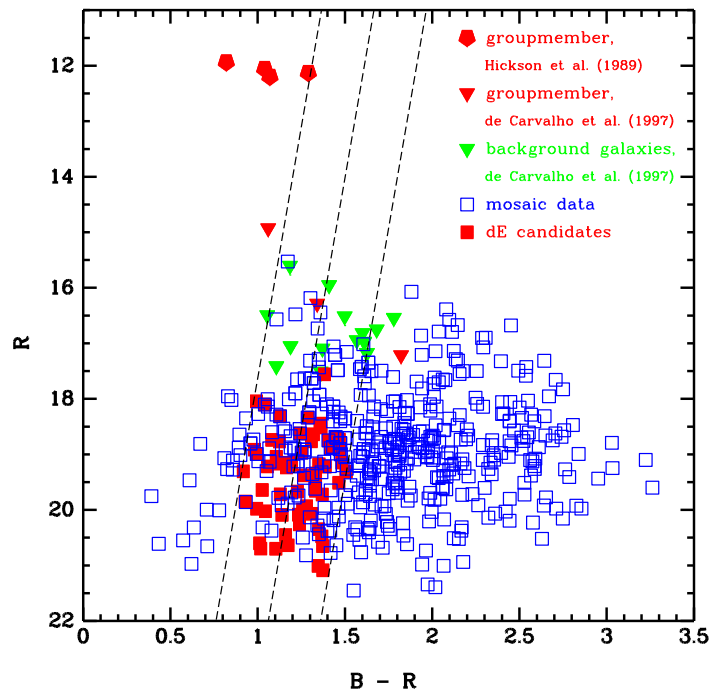


Figure 3.2: CMD of galaxies in HCG 16

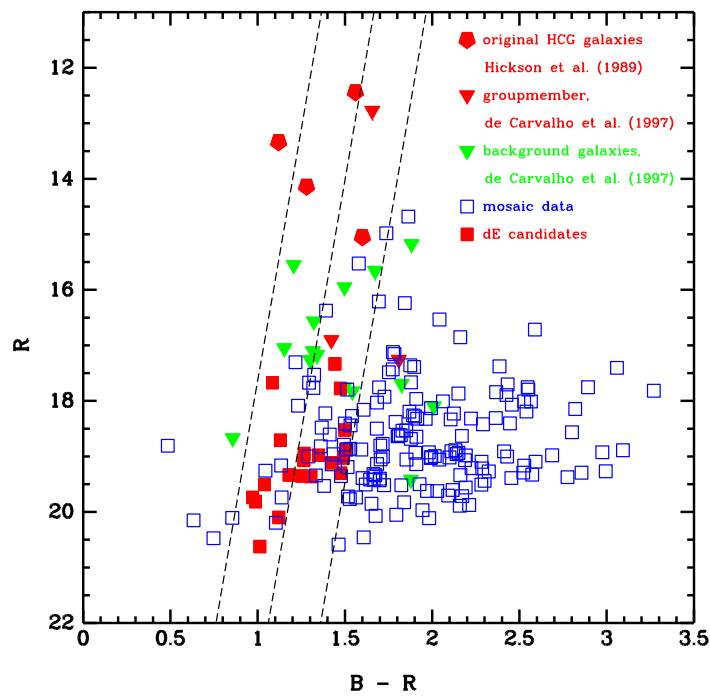


Figure 3.3: CMD of galaxies in HCG 19

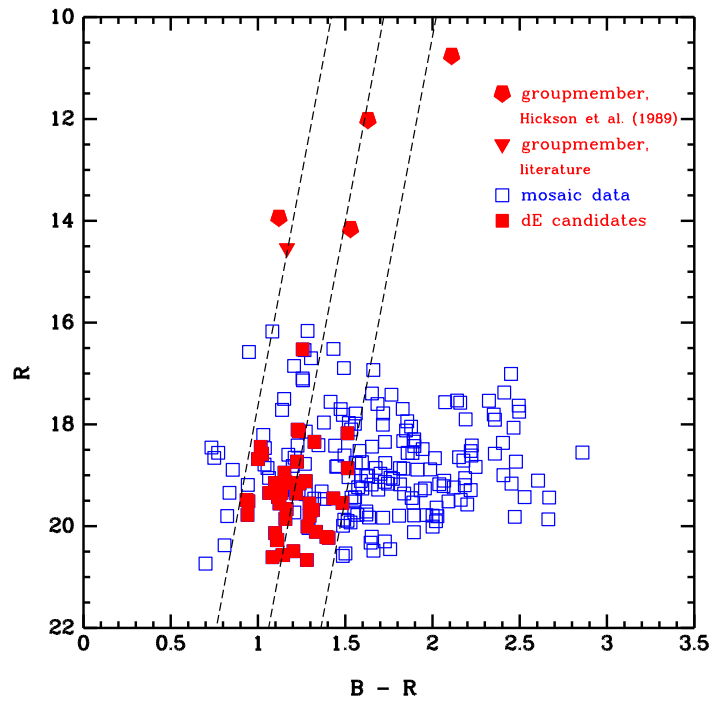


Figure 3.4: CMD of galaxies in HCG 30

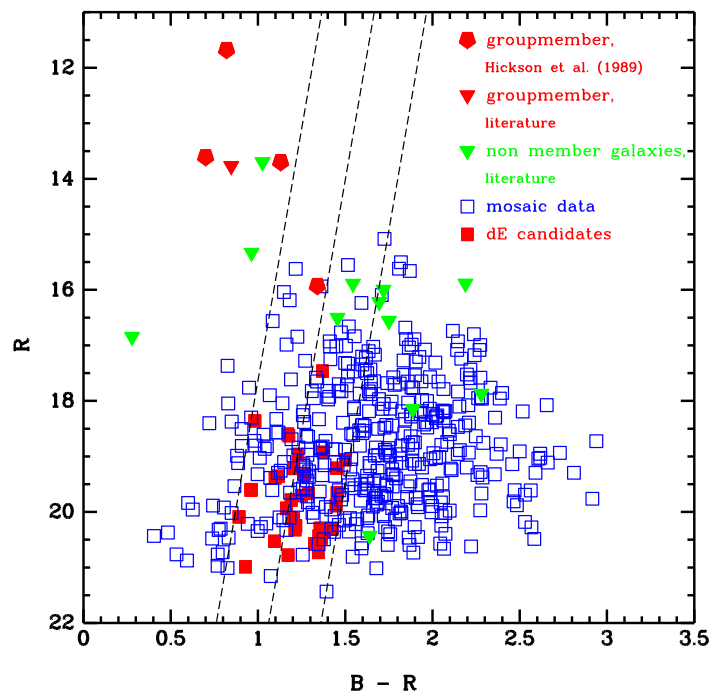


Figure 3.5: CMD of galaxies in HCG 31

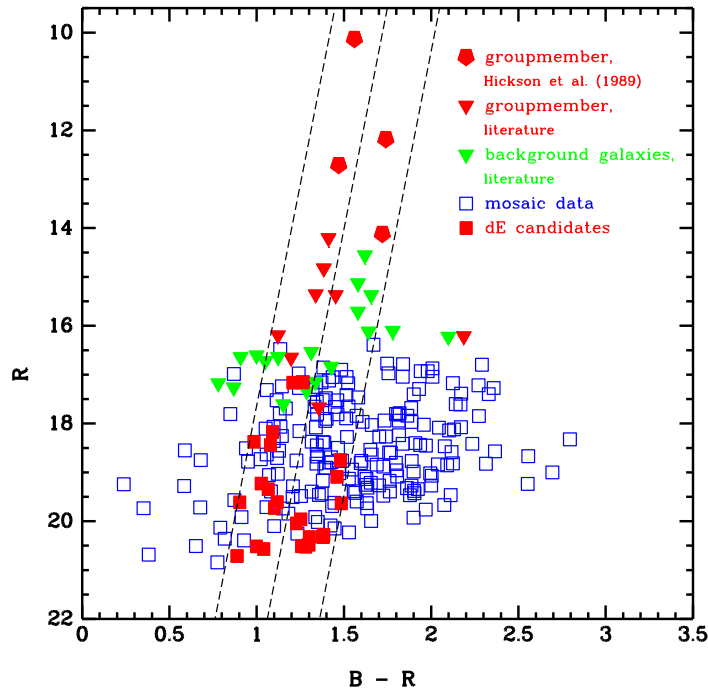


Figure 3.6: CMD of galaxies in HCG 42. The background galaxies and group members were spectroscopically identified by Zabludoff & Mulchaey (2000, 1998b) and de Carvalho et al. (1997).

strong radio and infrared emission (Hickson 1994).

Applying the selection criteria described in chapter 2.5 415 dwarf galaxy candidates in HCG 16 were found. 121 galaxies of this sample were photometrically (B_J) measured by the Automatic Plate Measuring (APM) galaxy survey (Maddox et al. 1990). The sample also includes the brightest 18 candidates in HCG 16, which were observed spectroscopically by de Carvalho et al. (1997). From the analysis of their redshifts 14 of the 18 galaxies can be excluded as background galaxies. However, there are still 397 dwarf galaxy candidates. Using the CMD and the red sequence of HCG 16 the number was reduced to 147 dE candidates. With the selection criteria described in section 3.1.2 59 high probability dE member galaxies according to their morphology, surface brightness, and radial profiles were identified. These galaxies are marked (filled squares) in the CMD (Figure 3.2). 13 of these 59 galaxies have APM magnitudes. Five background elliptical galaxies (some examples are shown in Figure A.1), 21 spiral edge on galaxies (some examples are shown in Figure A.2) and 48 spiral face on galaxies (some examples are shown in Figure A.3) and 14 undefinable galaxies were excluded from this sample. 20 dIrr candidates are found which are bluer than the red sequence of HCG 16. Using the same selection criteria nine high probability member dIrr were identified. Redwards from the red sequence most galaxies are background galaxies thus the objects in this area were not further investigated. Table B.1 lists the positions, the B and R magnitudes and the number (given by Source Extractor) of all 59

identified dE galaxies in HCG 16 and Table B.2 lists all positions, B and R magnitudes and numbers of the high probability dIrr member galaxies bluer than the red sequence.

3.2.2 Results HCG 19

HCG 19 consist of three galaxies and a discordant redshift galaxy in the center. One of the four galaxies is an elliptical and the others are distorted spiral galaxies. The brightest of the spiral galaxies is an infrared source (Hickson 1994).

212 candidates in HCG 19 were additionally found. Out of this sample the radial velocities of 17 galaxies were observed spectroscopically by de Carvalho et al. (1997). No radial velocities exist for the remaining 195 dwarf galaxy candidates. 81 of these 212 dwarf galaxy candidates were photographically (B_J) measured by the APM galaxy survey. The sample also includes the brightest 17 candidates, which were identified spectroscopically by de Carvalho et al. (1997). From their radial velocity at least 3 of these galaxies belong to the group and 14 are background galaxies. There are still 195 dwarf galaxy candidates. In the red sequence of HCG 19 51 high probability dE candidates are found. Using the selection criteria described above from their morphology, surface brightness, and radial profile 20 high probability dE member galaxies were identified, which are marked (filled squares) in the CMD (Figure 3.3). Seven of these 20 galaxies have APM magnitudes. Bluer than the red sequence four dIrr galaxy candidates were found. Using the same selection criteria four high probability member dIrr could be determined. Table B.3 represents the coordinates and magnitudes of all 20 identified dE galaxies in HCG 19 and Table B.4 represents all coordinates and magnitudes of the high probability dIrr member galaxies.

3.2.3 Results HCG 30

HCG 30 represents a quartet of galaxies. The velocity dispersion (72.4 km/s) is relatively low and also the mass-to-light ratio ($10.7 M_{\odot}/L_{\odot}$) (Hickson 1994).

219 dwarf galaxy candidates were identified in HCG 30 applying the selection criteria described in chapter 2.5. Two of these galaxies have additional detections from the 2MASS survey¹ and one galaxy was identified spectroscopically as group member by Tsvetkov & Bartunov (1993). From the red sequence of HCG 30 the number could be reduced to 90 dE candidates. Using the selection criteria described above 44 high probability dE member galaxies were identified from their morphology, surface brightness, and radial light profiles. These galaxies are marked (filled squares) in the CMD (Figure 3.4). None of these 44 galaxies have APM magnitudes. 9 dIrr galaxy candidates are bluer than the red sequence of HCG 30. Using the same selection criteria six high probability member dIrr galaxies were identified.

Table B.5 lists the coordinates and magnitudes of all 44 identified dE galaxies in HCG 30 and Table B.6 gives all coordinates and magnitudes from the high probability dIrr member galaxies bluer than the red sequence.

¹ Two Micron All Sky Survey

3.2.4 Results HCG 31

HCG 31 contains three galaxies and a discordant redshift galaxy. One of these galaxies, Markarian 1089 has strong emission lines and strong IR radiation, which arises from dust and gas heated by hot stars in star forming regions. As mentioned by Hickson (1994) it is very likely that this galaxy is undergoing a burst of star formation triggered by the interaction with NGC 1741, another CG galaxy and also a strong radio source.

Applying the selection criteria described in chapter 2.5 470 dwarf galaxy candidates in HCG 31 were found. 23 of these galaxies have detections which were found in NED². One galaxy was spectroscopically identified as group member, 12 galaxies were identified as non member galaxies (e.g Smith et al. 2000) and ten galaxies have photometric detections from the 2MASS survey. The spectroscopic information was taken from different literature data, there was not one survey like in the case of HCG 16, 19 and 42, which determined the velocities of the brighter galaxies in the field. Six of the twelve non member galaxies are foreground galaxies and six galaxies are background galaxies. From the red sequence of HCG 31 the number of dwarf galaxy candidates could be reduced to 152 dE candidates. Five of these galaxies have detections, two spectroscopically identified non member galaxies and three galaxies with photometric detections. Investigating these 152 dE candidates using the selection criteria described above 34 high probability dE member galaxies were identified from their morphology, surface brightness, and radial profiles. These galaxies are marked (filled squares) in the CMD (Figure 3.5). None of these galaxies has any detections in NED. 28 dIrr galaxy candidates are found bluer than the red sequence of HCG 31. Using the same selection criteria high probability member dIrr galaxies could be identified. Redwards from the red sequence most galaxies are background galaxies. The objects in this area were not further investigated.

Table B.7 lists the coordinates and magnitudes of all 34 identified dE galaxies in HCG 31 and Table B.8 gives all coordinates and magnitudes from the high probability dIrr member galaxies bluer than the red sequence.

3.2.5 Results HCG 42

HCG 42 contains four galaxies – a large elliptical radio galaxy (NGC 3091) and three smaller elliptical galaxies. One of these galaxies is very compact. It is very likely that its diffuse halo was stripped by the tidal forces of the massive neighbor galaxies (Hickson, 1994).

Applying the selection criteria described in chapter 2.5 252 dwarf galaxy candidates were found in HCG 42. 27 of these galaxies were spectroscopically measured. 18 of these galaxies are background galaxies and nine are group members due to their radial velocity (Zabludoff & Mulchaey 2000, 1998b, de Carvalho et al. 1997). The red sequence contains 132 dE candidates including eight member galaxies and 12 background galaxies. Investigating the new 112 dE candidates in the red sequence 25 high probability dE member galaxies were identified from their morphology, surface brightness, and radial profiles. These galaxies are marked (filled squares) in the CMD (Figure 3.6). None of these galaxies has any NED

² NASA/IPAC Extragalactic Database

detection. 19 galaxies are bluer than the red sequence of HCG 42. Using the same selection criteria four high probability member dIrr galaxies were identified. Redwards from the red sequence most galaxies are background galaxies thus the objects in this area were not further investigated.

Table B.9 lists the coordinates and magnitudes of all 25 identified dE galaxies in HCG 42 and Table B.10 gives all coordinates and magnitudes from the high probability dIrr member galaxies bluer than the red sequence. The B band image has half the integration time of images in the B band filter of the other HCGs, further the gaps between the CCD images could not be covered, because the final mosaic was formed out of two dithered images. Due to these facts 15 galaxies were not detected in these images, which have NED detections (Zabludoff & Mulchaey 2000, 1998b, de Carvahlo et al. 1997). Seven of these galaxies are group members and eight are background galaxies. As for these galaxies no B and R magnitudes exist, they are not shown in the CMD. Nevertheless these galaxies were included in the diagram showing the distribution of galaxies in the field (Figure 3.11) and the diagram showing the density distribution (Figure 3.17).

3.3 Spatial distribution

The spatial distributions of dEs and dIrrs provide a clue to the processes responsible for their differences. dIrrs are found in regions of low galaxy density - at the outer parts of clusters, in LGs and in the field. dEs are nearly exclusively found in areas of high galaxy density - as close companions to giant galaxies or they are found in cluster centers (Cote et al. 1997, Thompson & Gregory 1993, Binggeli et al. 1990, 1987, see also section 1.2.1). Examining the distribution of dwarf galaxies in the Coma Cluster (Thompson & Gregory 1993) and the Virgo cluster (Ferguson & Binggeli 1994, Binggeli et al. 1990, 1987) it was found, that dEs compose the largest number fraction of galaxies in the cluster core. Further Thompson & Gregory (1993) found, that the brighter dEs rise towards the cluster center following the distribution of the early-type galaxies. Investigating the outer regions they found, that the faint dEs are distributed in the same manner as the bright dEs. In the cluster center they found a deficit of faint dEs. This segregation suggests, that the environment plays a role in the evolution of dwarf galaxies.

Figures 3.7 to 3.11 show the spatial distribution of the original HCG galaxies (red diamonds), all spectroscopically identified group members (red triangles), all spectroscopically identified non member galaxies (blue triangles), high probability dE group members (red squares) selected from the red sequence and the high probability dIrr galaxies (red circles). The original CG galaxies can be seen in the center of each image. The plots' size covers the whole mosaic image size.

In cases where velocity information of some galaxies do exist some of the spectroscopically identified member galaxies at the borders of the mosaic images are found - far beyond the density centers of cataloged compact groups. Furthermore dE and dIrr candidates are found at the borders of the mosaic images. A well defined concentration of dEs to the center of the CGs like in clusters of galaxies cannot be identified but the data might not

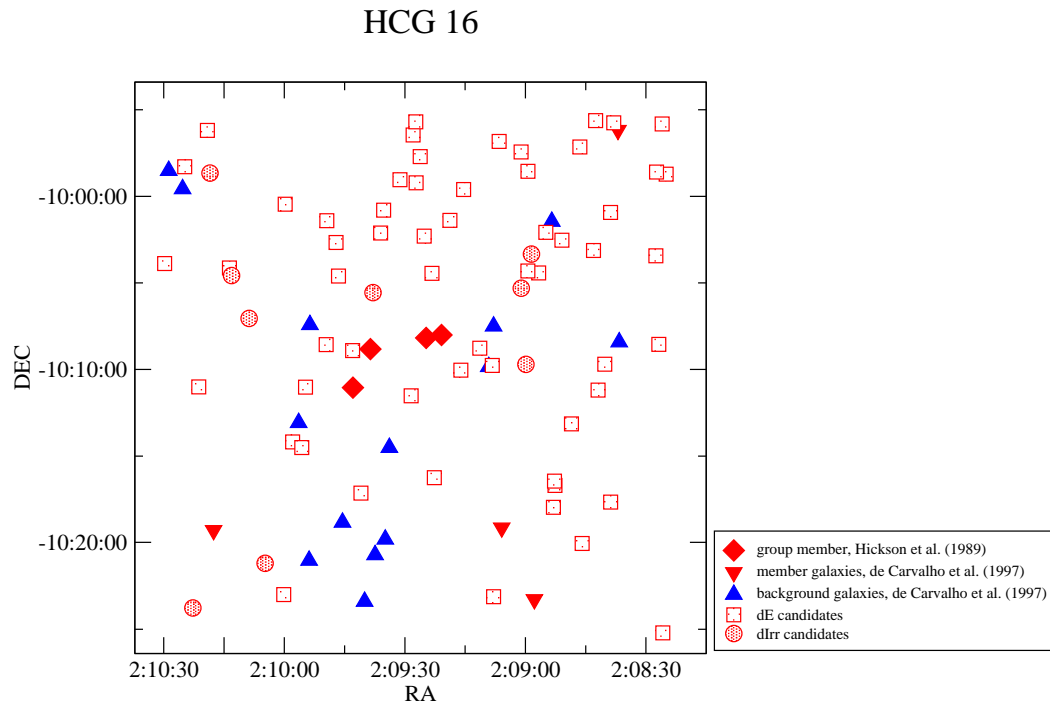


Figure 3.7: Distribution of galaxies within HCG 16

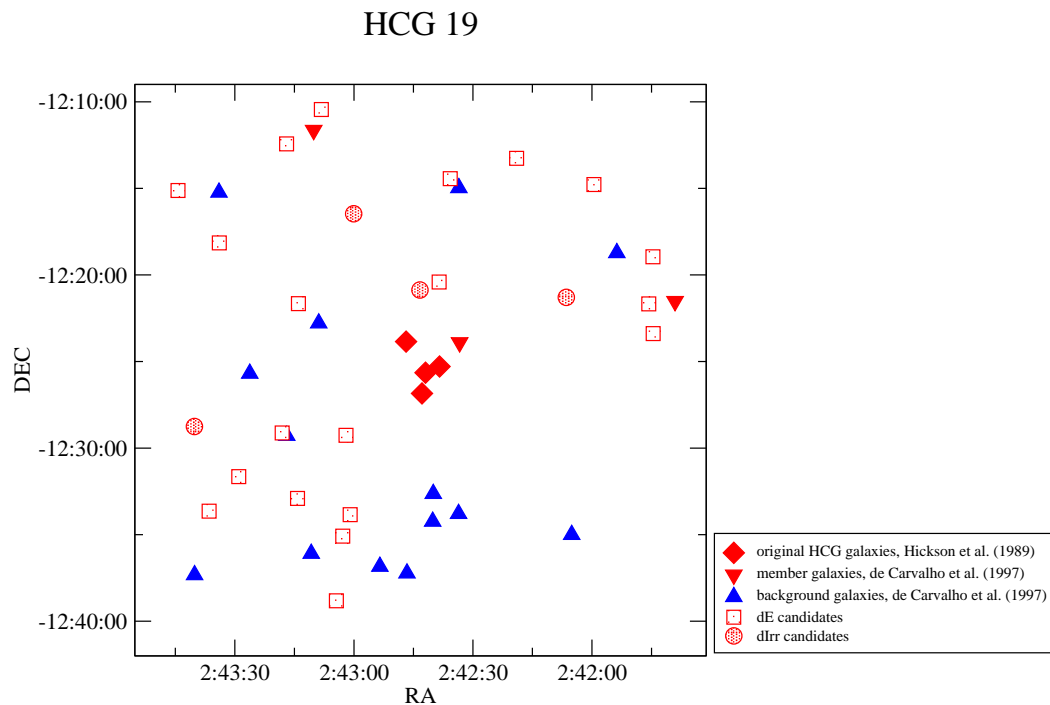


Figure 3.8: Distribution of galaxies within HCG 19

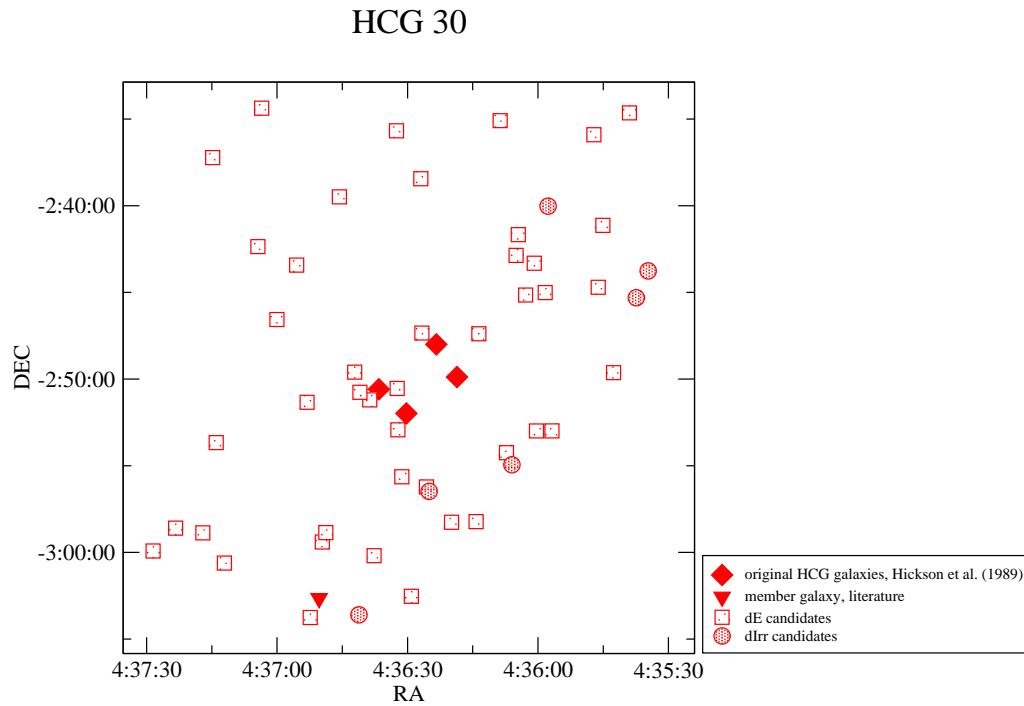


Figure 3.9: Distribution of galaxies within HCG 30

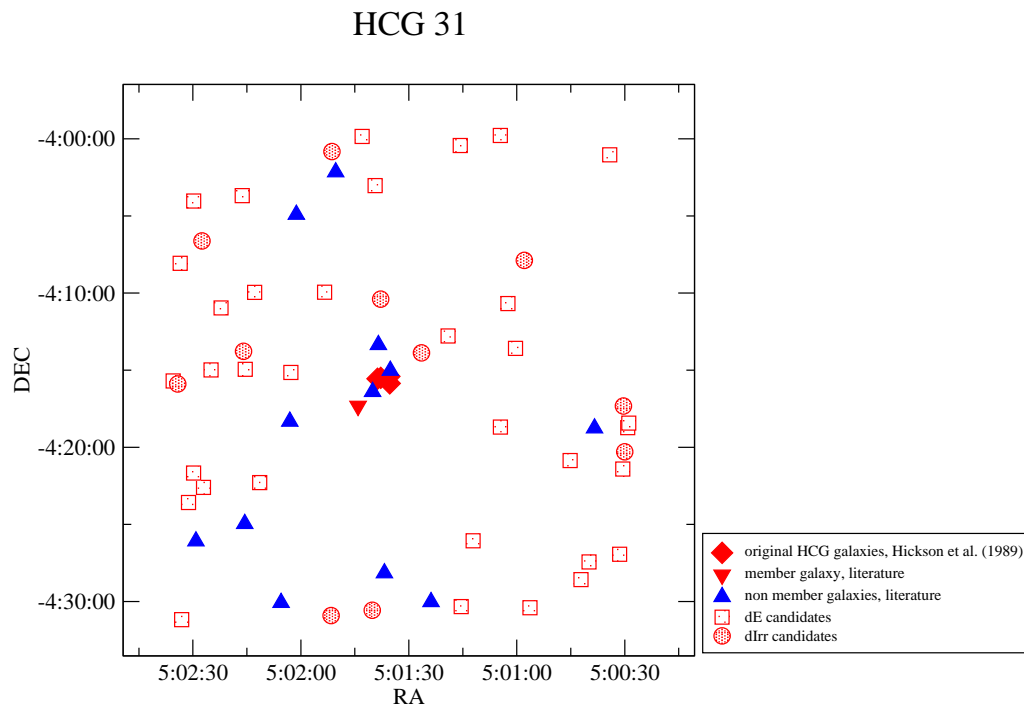


Figure 3.10: Distribution of galaxies within HCG 31

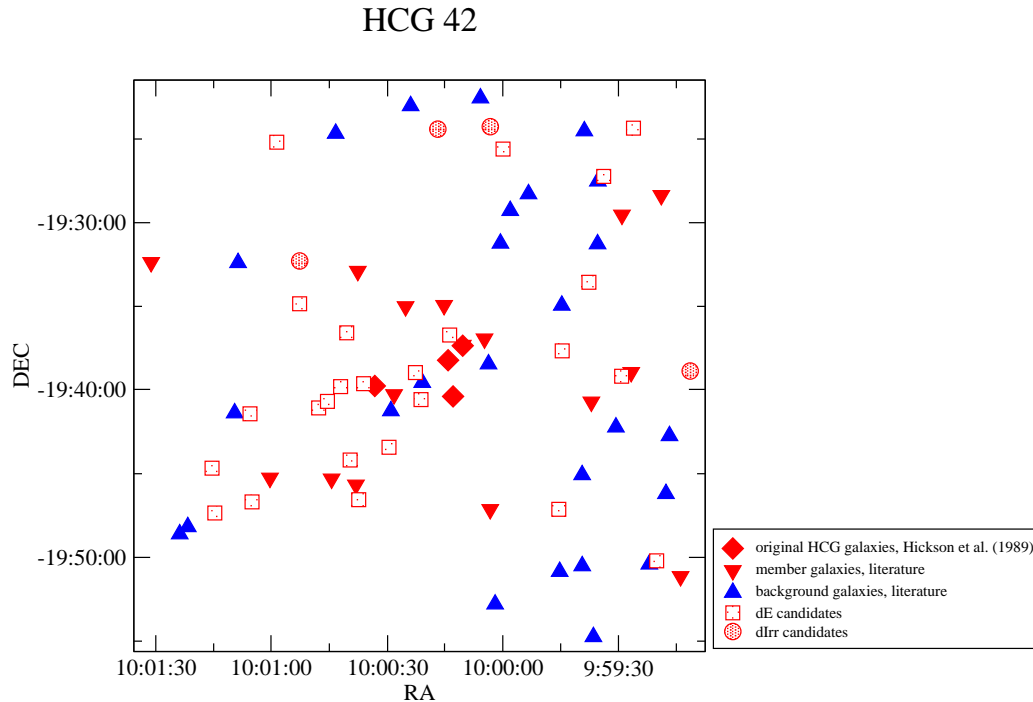


Figure 3.11: Distribution of galaxies within HCG 42

have reached the limit of the CGs yet. From these results it can be assumed, that the groups might be more extended than the limits of the mosaic data.

Mulchaey et al. (2003) searched for diffuse X-ray emission in 109 nearby galaxy groups and found evidence for hot intra group medium in about half of the groups using the ROSAT³ PSPC⁴. Three (HCG 16, 31 and 42) of the sample CGs are included in this sample. It should be mentioned that the nearby groups were only detected to a fraction of the virial radius with the ROSAT PSPC thus a significant amount of the gas mass may be found beyond the radius of the X-ray detection. Mulchaey et al. (2003) found diffuse emission in HCG 16 and HCG 42 with exposure times of 14000s for HCG 16 and 11799s for HCG 42, while HCG 31 was not detected in X-ray. The non detection of HCG 31 may be due to the short exposure time of 1584s. The morphology of the X-ray emission of HCG 16 is irregular and not centered on a particular galaxy, but it shows a slight alignment in diagonal direction across the CG center, which coincides with 50% of the dwarf galaxy candidates. The X-ray emission found in HCG 42 is nearly round and has a symmetrical morphology and is almost concentrated to the group center which implies that the group is virialized. Grebel et al. (2003) explored the gas-deficit of dSph galaxies in early- and late-type dwarf

³ X-ray satellite

⁴ Position Sensitive Proportional Counters (PSPC)

galaxies in the Local Group. It is surprising that these dSph galaxies are free of detectable interstellar material, although they experienced star formation during several time spans. Grebel et al. (2003) argued that the larger part of interstellar material from dSphs was removed by ram pressure stripping by gas in the galaxy halos and an inter group medium. It is therefore assumed as one possibility that the identified dE candidates were formed due to ram pressure stripping. It is found that 87% of the identified high probability group members in HCG 16 are dEs. 83% in HCG 19, 88% in HCG 30, 75% in HCG 31 and 86% in HCG 42 are dE candidates. This represents evidence for the group membership of the dwarf galaxy candidates. As there is any velocity information of the dwarf galaxy candidates there is no opportunity to verify this assumption, yet.

3.4 Density distribution

The diagram in Figure 3.12 shows the azimuthally averaged density distribution of galaxy members spectroscopically identified (predominantly by Zabludoff & Mulchaey (1998b) and from redshift surveys listed in NED) in HCG 16, HCG 42, and HCG 62. The dashed lines denote the density distribution including the original HCG galaxies. There is a density peak around $200 h^{-1}$ kpc from the center in all three diagrams (HCG 16, HCG 42 and 62).

Although the result may be subdued to small number statistics it is very surprising that the CGs have an area limit inside $200 h^{-1}$ kpc (\approx limit of the mosaic images), which means that the member galaxies are concentrated to the group center. However, the diagrams show that the compact groups might either have a larger extension or that there is a gap of group members between $150 h^{-1}$ kpc and $200 h^{-1}$ kpc. As the galaxy samples forming these density distributions were extracted from surveys which do not reach the faint dwarf galaxy population it is very important to focus on the area inside the $200 h^{-1}$ kpc radius in order to study the faint galaxies – the dwarf galaxy populations. The histograms in Figure 3.13 to 3.17 show the azimuthally averaged density distribution of galaxies identified in HCG 16, 19, 30, 31, and 42. The abscissa represents the radial distance from the center normalized to h and the ordinate represents the number of galaxies per unit area normalized to the central circular area with radius $30 h^{-1}$ kpc and the number of spectroscopically identified member galaxies therein. The radial number density profiles were derived by first summing the number counts of the galaxies within radial annuli of $30 h^{-1}$ kpc.

Plot a) shows the density distribution for all spectroscopically identified member galaxies (Figure 3.2 to 3.6, Figure 3.7 to 3.11 red triangles). Plot b) represents the density distribution of all dEs and dIrrs, which were identified as high probability group members (Figure 3.2 to 3.6 red squares, Figure 3.7 to Figure 3.11 red squares and red circles). The density distribution in plot c) is the sum of the density distribution of a) and b). The solid line in plot d) represents the density distribution of all spectroscopically identified background galaxies (Figure 3.2 to 3.6 green triangles, Figure 3.7 to 3.11 blue triangles). The dotted line represents the density distribution of all rest galaxies of the sample, which are neither spectroscopically member galaxies or dEs or dIrrs identified in the red sequence

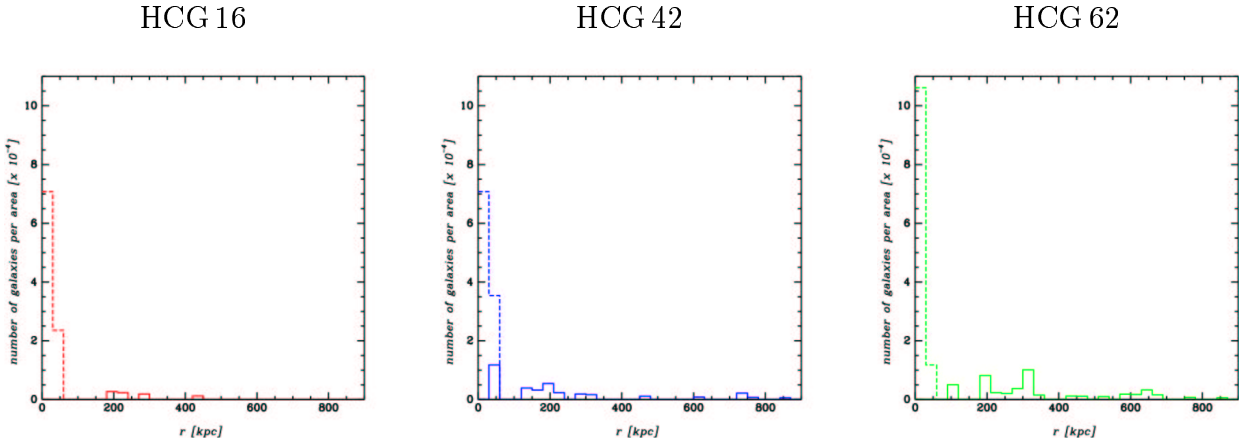


Figure 3.12: Density Distribution of galaxies in HCG 16, 42 and 62 spectroscopically identified as group members by Zabludoff & Mulchaey (1998b)

nor spectroscopically identified background galaxies (Figure 3.2 to 3.6 blue squares). These were normalized to the number of non member galaxies in the first circular area.

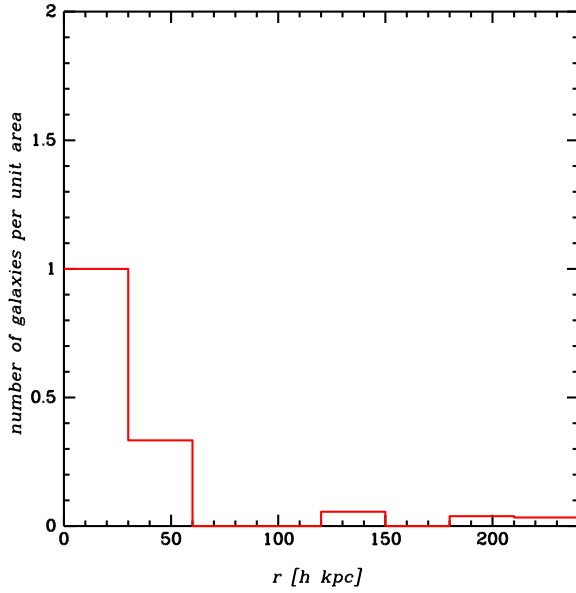
In all histograms a more or less distinct density peak in the center, which decreases up to the limit of the mosaic images can be seen. The density distribution of all galaxies neither spectroscopically member galaxies or dEs or dIrrs identified in the red sequence nor spectroscopically identified background galaxies is nearly flat, except for HCG 42. This suggests, that a large fraction of group members was not identified in HCG 42, yet. Assuming a flat density distribution of background galaxies, a statistical minimum number of 12 ± 3 additional group members could be determined.

As member galaxies at the limits of the mosaic images are found, it is very likely that the group is more extended. The whole dimensions of the CGs were not acquired yet. In all of the studied HCGs dwarf galaxy members are found far beyond the density centers of cataloged CGs.

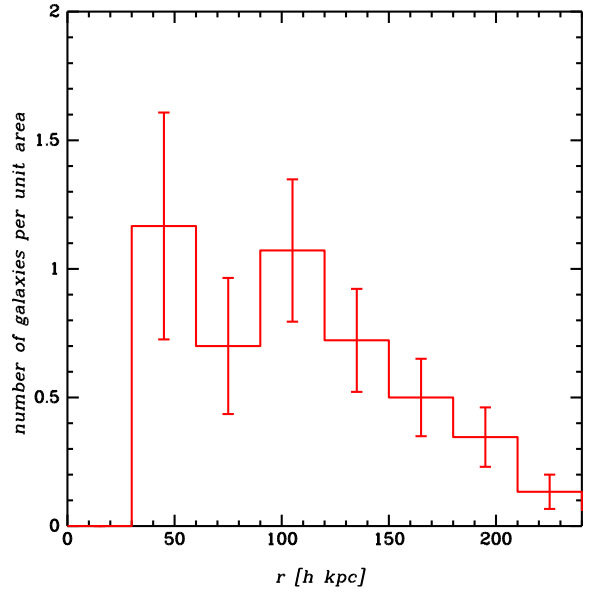
3.5 Galaxy counts

From the investigation of substructures in groups of galaxies it is possible to provide cosmological constraints if galaxy groups evolve hierarchically like galaxy clusters. Zabludoff and Mulchaey (1998b) analyzed six nearby poor groups of galaxies (including HCG 42 and 62) with more than 30 spectroscopically confirmed members each, X-ray halos extending out to radii of $\sim 200 - 300 h^{-1}$ kpc, and detected substructure in two cases (HCG 62 and NGC 741). The substructure is due to a subgroup which lies $\sim 0.3 - 0.4 h^{-1}$ Mpc outside of the center of the group. Determining this substructure they applied the method of Dressler & Shectman (1988). In short this method identifies a fixed number of neighbors on the sky around each galaxy. Then the mean velocity and the velocity dispersion of the subsample

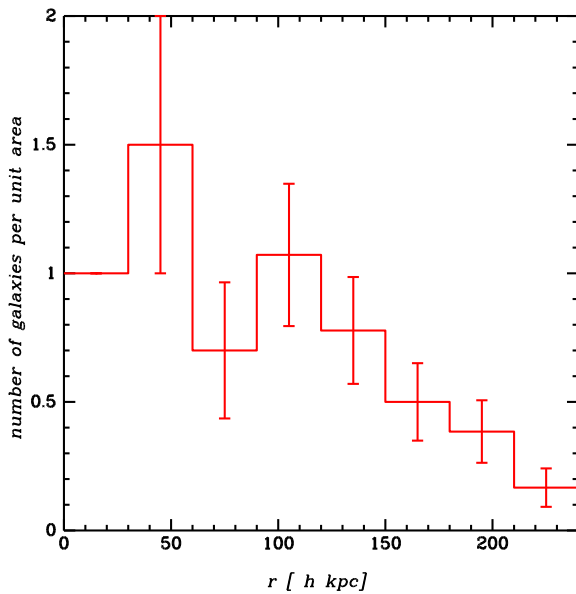
a) member galaxies



b) dE + dIrr galaxies



c) member galaxies + dEs + dIrr



d) background galaxies

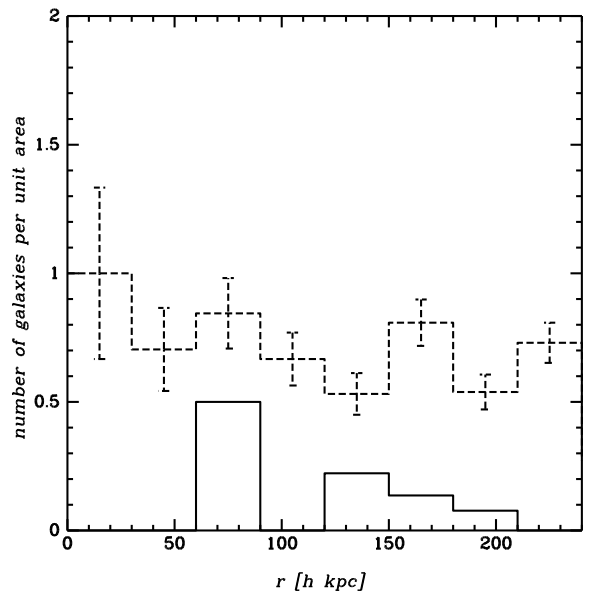
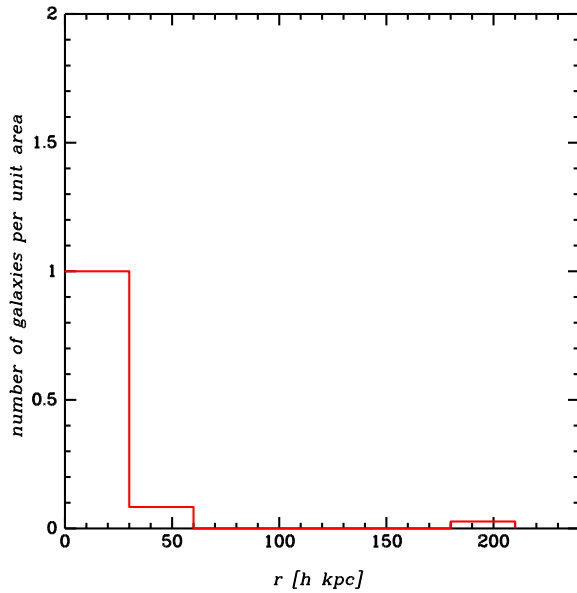
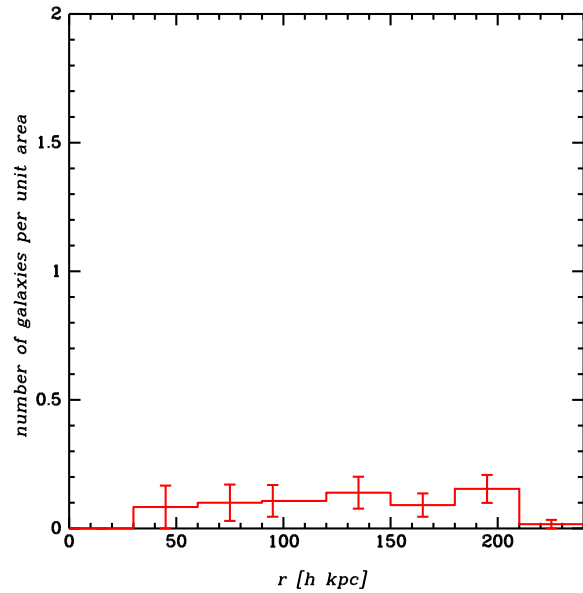


Figure 3.13: All plots (a – d) show the azimuthally averaged density distribution of all galaxies found in HCG 16. The abscissa represents the radial distance from the center normalized to h and the ordinate the number of galaxies per unit area. Plots a – c are normalized to the central circular area with radius $30 h^{-1}$ kpc and to the number of spectroscopically identified member galaxies therein. Plot d is normalized to the number of all background galaxies in the first circular area (dotted line). The solid line in plot d represents the spectroscopically identified background galaxies.

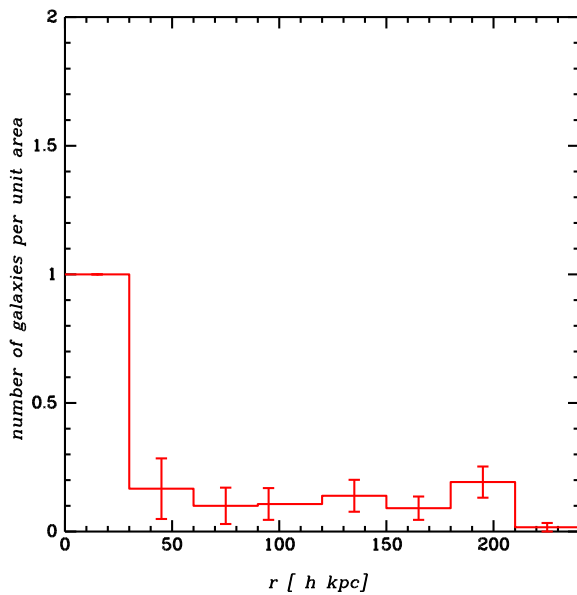
a) member galaxies



b) dE + dIrr galaxies



c) member galaxies + dEs + dIrr



d) background galaxies

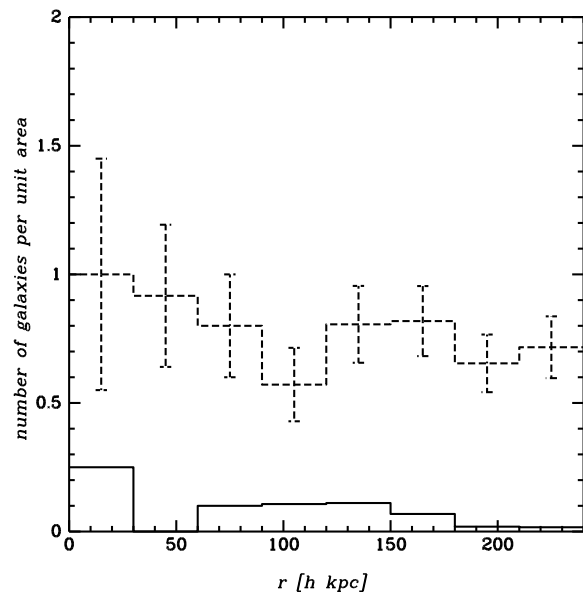
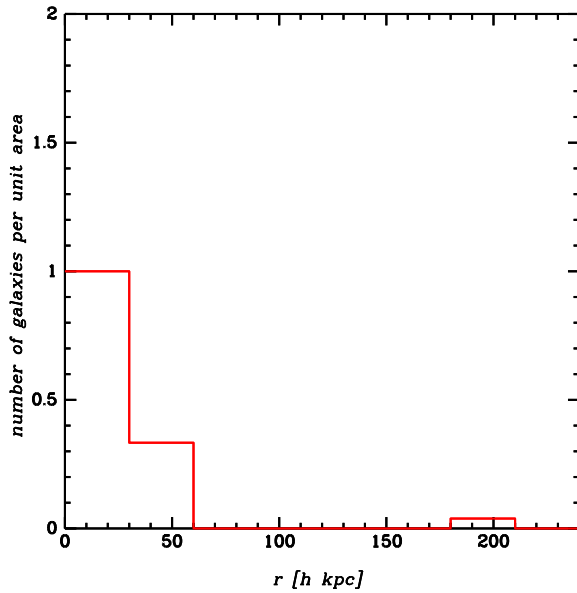
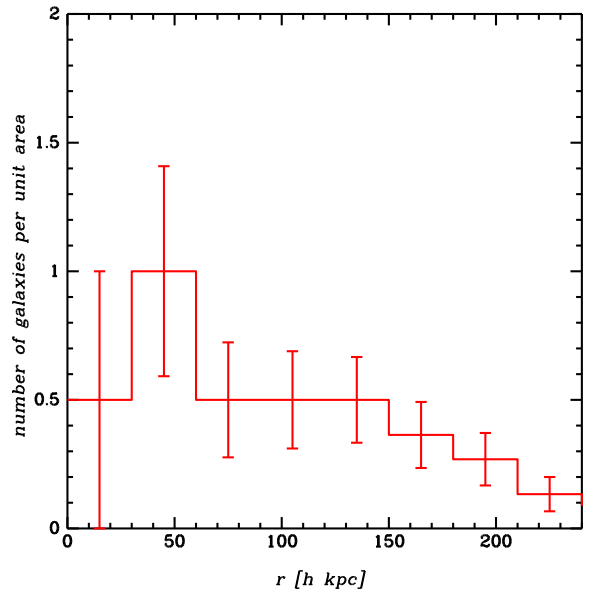


Figure 3.14: The same as Figure 3.13 for the azimuthally averaged density distribution of all galaxies found in HCG 19

a) member galaxies



b) dE + dIrr galaxies



c) member galaxies + dEs + dIrr

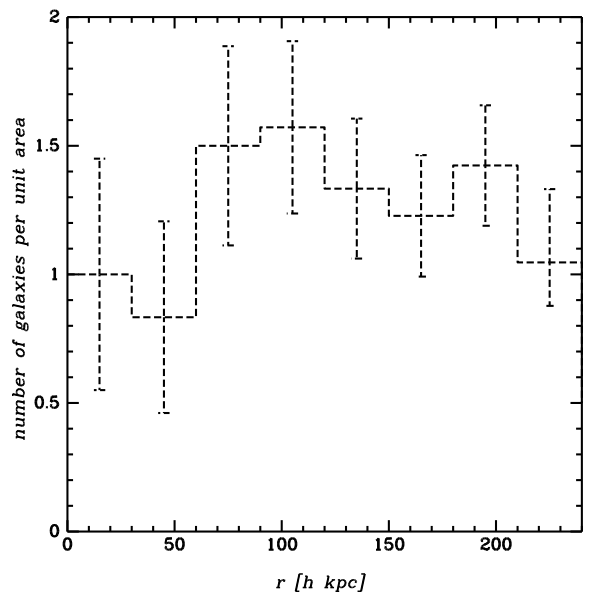
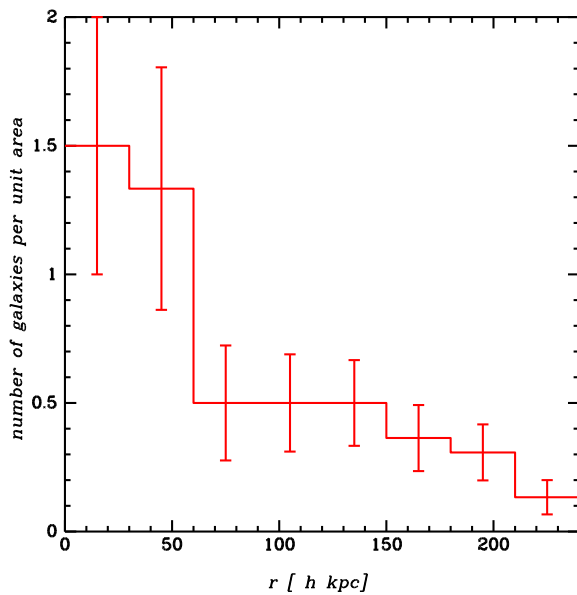
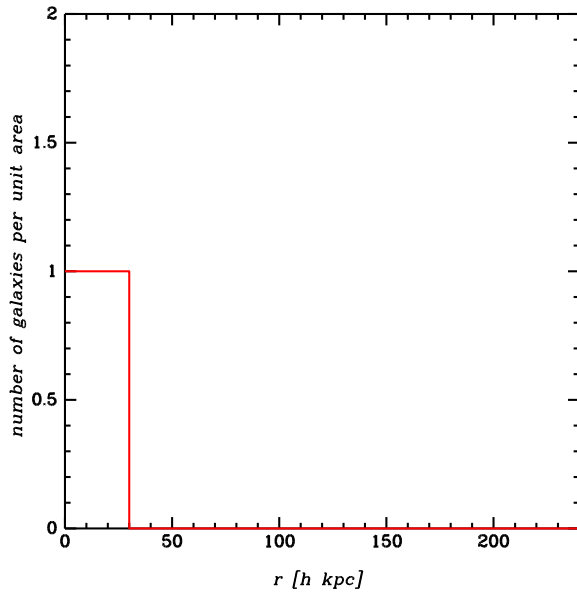
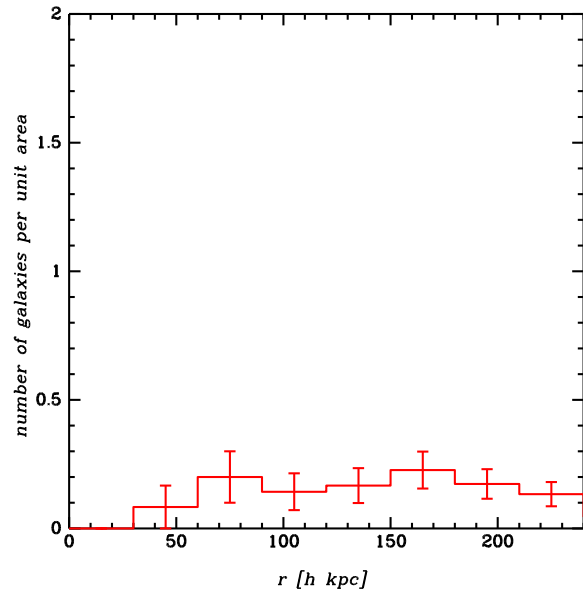


Figure 3.15: The same as Figure 3.13 for the azimuthally averaged density distribution of all galaxies found in HCG 30

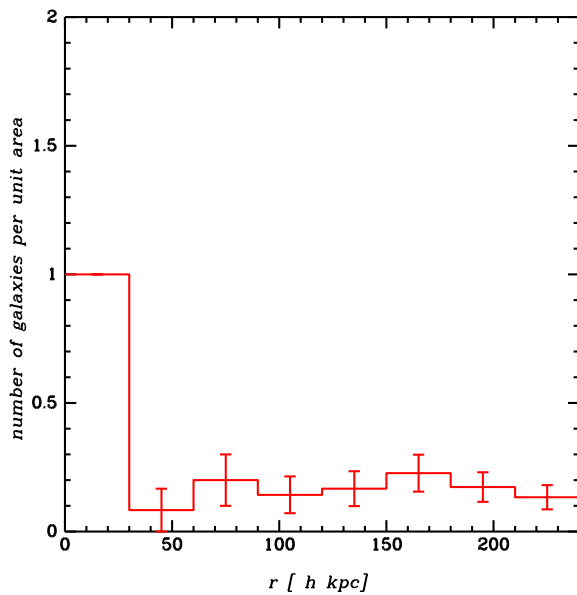
a) member galaxies



b) dE + dIrr galaxies



c) member galaxies + dEs + dIrr



d) background galaxies

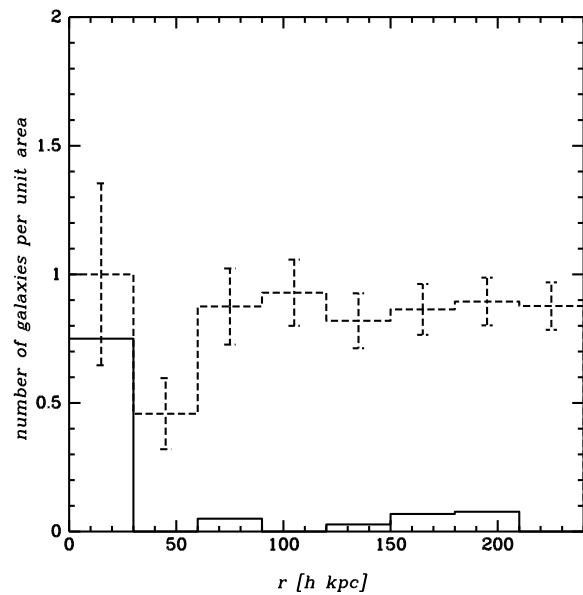
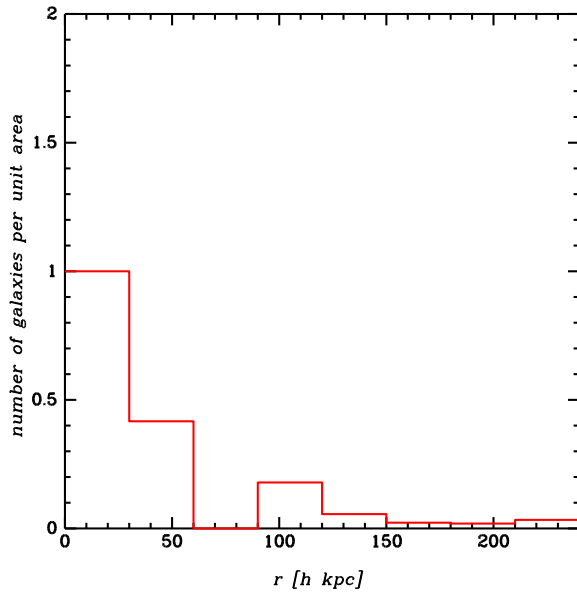
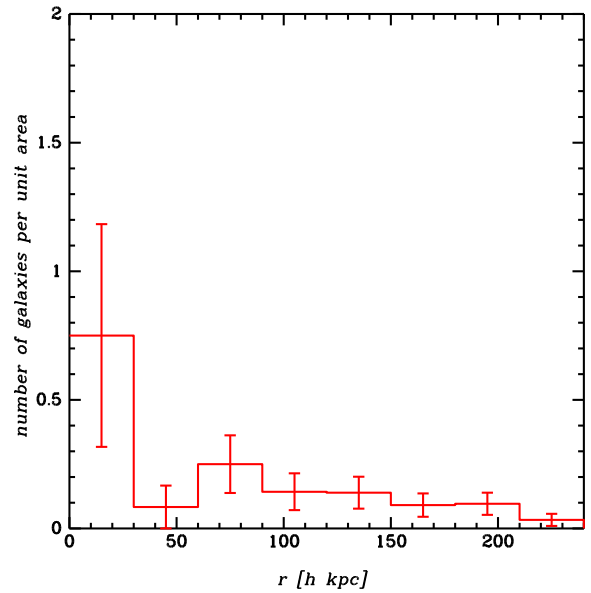


Figure 3.16: The same as Figure 3.13 for the azimuthally averaged density distribution of all galaxies found in HCG 31

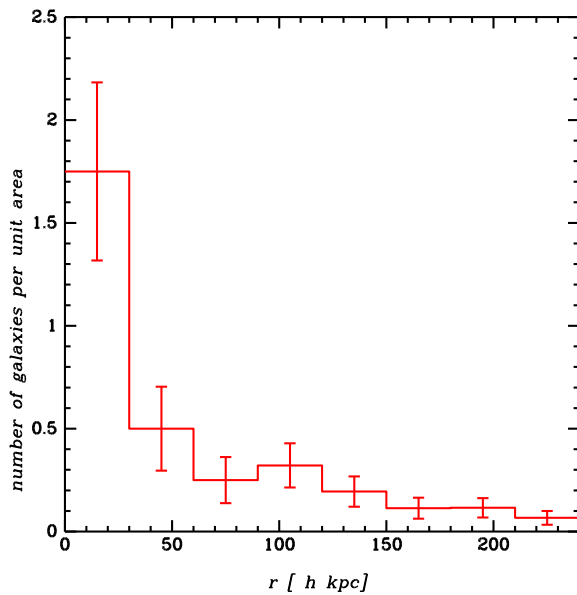
a) member galaxies



b) dE + dIrr galaxies



c) member galaxies + dEs + dIrr



d) background galaxies

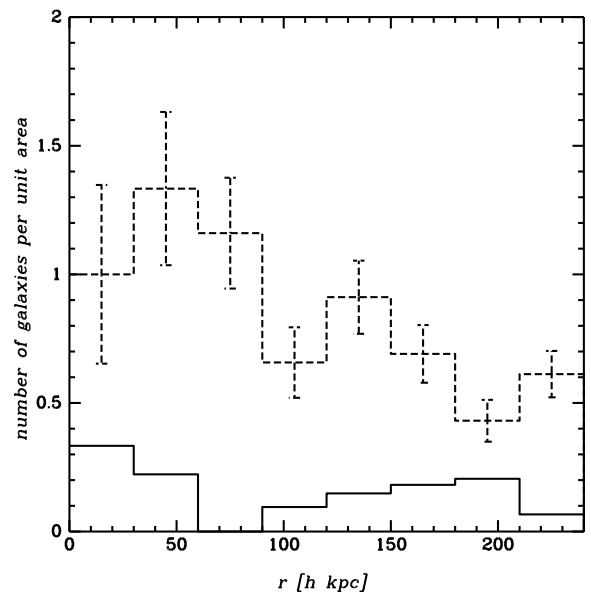


Figure 3.17: The same as Figure 3.13 for the azimuthally averaged density distribution of all galaxies found in HCG 42

is calculated and finally these values are compared with the mean velocity and velocity dispersions of the whole group. This method requires velocity information for all galaxies, thus it cannot be used to determine any substructure in the HCG sample. As no velocity information of the dwarf galaxy candidates exist, the idea goes back to “Streifenzählungen” (galaxy counts) in order to find any substructure.

This method goes back to the model of “star counts” as described in Pahlen & Gondolatsch (1937). The spacial density $\rho(r)$ follows directly from the surface density $S(x)$ at $x = r$.

$$\rho(x) = -\frac{1}{2\pi x} \frac{dS(x)}{dx} \quad (3.5)$$

Each mosaic image was overlaid by a grid with a mesh size of $30 h^{-1}$ kpc in α and δ direction. In these meshes the number counts of the dE and dIrr galaxies were determined. A slight concentration of approximately 10% can be found in the group center of all CGs. In the case of HCG 16 a concentration of dEs north of the CG center was detected. The other CGs do not show any further concentrations despite the slight concentration in the group center.

3.6 The Luminosity Function of HCGs

With the dwarf galaxy population of the HCG sample it is now possible to determine the LF of HCGs to relate quantitatively the galaxy content with the environment they are embedded in. The LF is defined as the number density of galaxies per unit luminosity L . Therefore an accurate object detection is essential to determine the LF correctly. Based on the deep observations used in this work a much fainter luminosity brightness is reached which is the main improvement to the LFs of HCGs published in the literature. The resulting LF is compared to LFs given in the literature for the field and galaxy clusters.

The general LF $\phi(M)$ for galaxies is needed to calculate the distribution of galaxies of each type in various apparent magnitude intervals. It’s measurement generally proves to be difficult due to the different observational selection criteria in samples (e.g. magnitude limited or volume limited such as galaxy groups and clusters). For low-density and high-density regions a clear qualitative distinction between the resulting $\phi(M)$ can be made. In addition to the general LF Sandage et al. (1985) defined a differential LF $\phi(M)dM$ as the number of galaxies in a complete volume limited sample in the absolute magnitude interval dM , which is centered on M and summed over all galaxy types. $\phi(M)$ was determined in their study for the central 6° radius core of the Virgo Cluster to a total magnitude ($B_T \simeq 20 \approx B = -11$) estimating that the completeness limit was two magnitudes brighter ($B_T \geq 18$).

In order to fit their data points the authors considered a gaussian distribution and an exponential distribution. The gaussian has the form

$$\phi(M) \sim e^{-\frac{(M-\mu)^2}{2\sigma^2}} \quad (3.6)$$

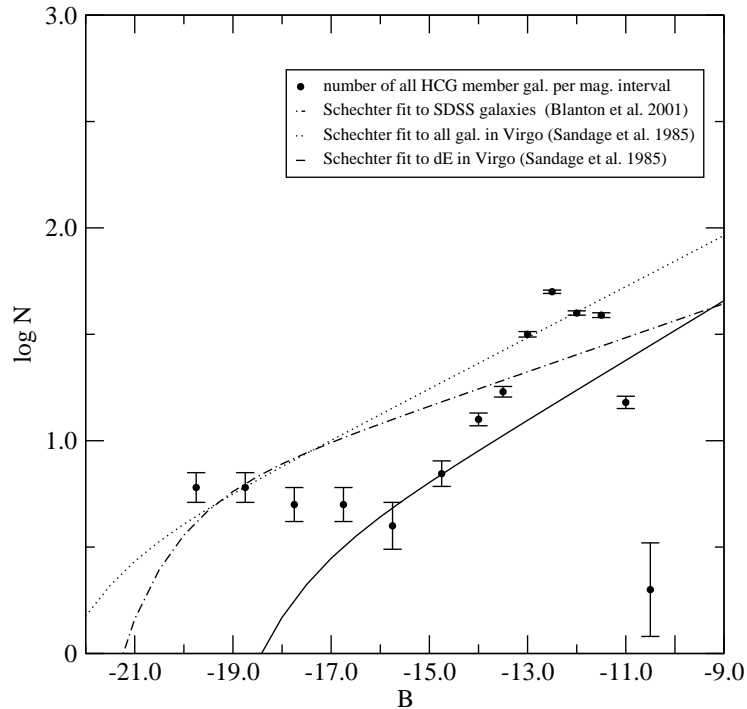


Figure 3.18: The diagram relates the number of galaxies per total magnitude interval. On the y-axis a logarithmic scale is used. The data points represent the number of all HCG member galaxies. Galaxies lying in the interval $-20.25 \leq B \leq -16.25$ were binned in 1 mag steps and the faint galaxies lying in the interval $-16.25 \leq B \leq -10.25$ were binned in 0.5 mag steps. The dashed-dotted line represents the Schechter fit to SDSS galaxies with the parameters $M = -20.83$ and $\alpha = -1.2$ (Blanton et al. 2001); the dotted line represents the Schechter fit to all galaxies identified in the Virgo Cluster core with $M_B = 10.3$ mag and $\alpha = -1.3$ and the solid line represents the Schechter fit to all dE galaxies found in the Virgo Cluster with the parameters $M_B = 14.3$ mag ($M = -17.4$) and $\alpha = -1.35$ calculated by Sandage et al. (1985).

with μ the mean magnitude and σ as the dispersion. For the exponential distribution a Schechter function (Schechter 1976) was considered:

$$\phi(M) \sim (10^{0.4(M^* - M)})^\beta e^{-10^{0.4(M^* - M)}} \quad (3.7)$$

with α , (or $\beta = \alpha + 1$) and M^* as the fitting parameters. $\alpha = -2$ describes a divergent total luminosity case, $\alpha = -1$ produces a flat differential LF and $\alpha \geq -1$ describes a

declining differential LF at the faint end. In both approaches the fixed normalization, which is known from the total number of galaxies of a given type, has to be taken into account.

In this thesis it was possible to determine the LF for all sample HCG member galaxies down to a magnitude of $B = -12.5$ which is near to the maximal depth of the mosaic images lying approximately at -12 mag in the B band. Fringe corrections and the diffuse light correction, which were performed during the reduction of the mosaic data, prevented to determine a precise value for the completeness limit. Nevertheless the limiting magnitude of $B = -12.5$ allows to analyze the faint end of the distribution in more detail. The data points in Figure 3.18 represent all HCG group members. This comprises members discovered and confirmed photometrically by this thesis and also members investigated spectroscopically by other studies. Galaxy members lying in the interval $-20.25 \leq B \leq -16.25$ for the absolute luminosity were binned in 1 mag steps and reflect the number of giant galaxies per interval. They are subject to small number statistics, which is expected due to the definition of HCGs. Faint galaxies, lying in the interval $-16.25 \leq B \leq -10.25$, were binned in 0.5 mag steps, which proves to be adequate because the intervals are still larger than the largest estimated magnitude error per galaxy. The distribution is compared to three different fits, see Figure 3.18. The dashed-dotted line represents the fit to SDSS⁵-field galaxies (data set with 11,275 local galaxies, Blanton et al. 2001), obtained by fitting a Schechter function to the distribution. The dotted line represents the fit to all galaxies identified in the Virgo Cluster core and the solid line represents the fit to dE galaxies found in the Virgo Cluster, both calculated by Sandage et al. (1985) using also a Schechter function. The distribution of all sample HCG member galaxies shown in Fig 3.18 can be divided in two qualitatively distinct parts. At the bright end, from ≈ -20 to -16 mag, the distribution can be described by a plateau, which is slightly declining towards fainter magnitude intervals. Beginning at the magnitude interval of ≈ -15 the number of galaxies per interval unit rises steeply reaching a maximum at ≈ -12 mag. Thereafter a steep drop can be observed which coincides with the limiting magnitude for the depth of the observations in the B band. Compared to the fits calculated by Blanton et al. (2001) and Sandage et al. (1985) a qualitative similarity is found since, the data of this work as well as the fits rise at the faint end of the distribution. The largest similarity between the distribution of HCG member galaxies and the comparison distributions seems to be in the distribution describing the dE content of the Virgo Cluster calculated by Sandage et al. (1985). However, in the thesis data set the increase is more steeper than in any of the three fits shown. An extensive discussion of this result will be given in section 4.2.

3.7 Zero-velocity surface R_0

This section describes the estimation of the dynamical mass of the group and the radius of the zero-velocity surface, R_0 , beyond which galaxies participate in the Hubble expansion. From results of the spatial and density distribution of HCGs (section 3.3 and 3.4) it was

⁵ Sloan Digital Sky Survey

found that HCGs might extend far beyond the centers of cataloged CGs. Thus the question arose to determine their masses and extensions. Groups of galaxies after clusters of galaxies are the second largest virialized systems. Thus they are important to investigate the large-scale structure of the Universe while providing estimates on the dynamical mass density parameter on ~ 1 Mpc scales.

The common mass estimators, which use the position of the objects and the velocity dispersions are the virial mass estimator and the projected mass estimator. The projected mass estimator and the virial mass estimator are adequate for an isotropic and spherically symmetric gravitational system (Perea et al. 1990, Heisler et al. 1985).

Heisler et al. (1985) concluded that the projected mass estimator is the best option to determine the mass of clusters from galaxy motions. In contrast to that result Perea et al. (1990) suggested, that the virial mass estimator is the more suited since the presence of substructure and anisotropy can lead to an overestimation of the mass, if they are not taken into account. However, Aceves & Perea (1999a, 1999b) objected that one physical reason for the overestimation of mass by using the virial mass estimator is an incompleteness concerning the consideration of the potential energy of the subsystem. Aceves & Perea (1999a, 1999b) tested the two mass estimators using N-body experiments assuming spherical, isolated, and isotropic velocity dispersion systems. They found that the projected mass estimator overestimates masses by 20%, if it is only applied to regions around the total system's effective radius. The virial mass estimator can yield to a correct mass at different radii, if the potential energy term is correctly taken into account and furthermore the system is completely sampled. If not it will lead to similar errors as for the projected mass estimator. They do not consider rotation in clusters.

A problem in determining the mass of a group using the projected or the virial mass estimator is the unknown physical boundaries of the groups, which are affected by the sensitivity of the instruments and the criteria defining a cluster or group. Furthermore the analysis of the structural parameters in clusters of galaxies showed that they appear to be triaxial and not spherically symmetric (Plionis et al. 1991) and the velocity distribution of clusters and groups may not be isotropic, because of the infall of galaxies and material.

Due to the assumptions of N-body simulations they cannot represent the reality. For the projected mass estimator and the virial mass estimator the errors lie in the worst cases at 20%. There are a lot of assumptions and theories in determining the dynamical mass of virialized systems. In order to get an idea of the mass the projected mass estimator was used.

To determine the extension of the whole CG first velocity information of group members are necessary in order to determine their dynamical masses. For some CGs some literature data were available. Tables C.1 to C.5 list all galaxies lying at a projected distance of 2 Mpc around the center of the CGs. Further all these galaxies have velocities smaller than 1000 km/s in regard to the velocity of the group center. The line-of-sight velocity difference of galaxies in a gravitationally bound system is a measure of their relative peculiar velocity. Hickson et al. (1992) investigated that the median radial velocity dispersion in HCGs amounts only to ≈ 200 km/s. Thus choosing 500 km/s for the HCG sample is large

HCG	N_m	M_{dyn} [$h^{-1}M_\odot$]	ΔM_{dyn} [$h^{-1}M_\odot$]	R_0 [$h^{-1/3}$ kpc]	ΔR_0 [$h^{-1/3}$ kpc]
16	15	6.251099×10^{12}	5.16011×10^9	1646	0.94
19	11	1.107464×10^{14}	2.93573×10^{10}	4292	0.79
30	12	4.270217×10^{13}	1.55039×10^{10}	3124	0.78
31	10	1.511684×10^{14}	3.526×10^{10}	4760	0.77
42	37	6.9842×10^{13}	9.778×10^9	3680	0.36

Table 3.1: Dynamical mass (M_{dyn}), the error (ΔM_{dyn}), the radius of the zero-velocity surface (R_0), and the statistical error (ΔR_0) for the sample HCGs (with member galaxies (N_m) in an area of 2 Mpc around the center and a velocity dispersion smaller than 500 km/s)

enough to include a large fraction of physically associated galaxies.

The radius of the zero velocity surface (equation 3.9) was calculated via Sandage (1986).

$$M_{dyn} = M_{PM} = \frac{32/\pi \sum_i v_i R_i}{G(N_m - 1.5)} \quad (3.8)$$

with:

M_{PM} : projected mass estimator

N_m : number of galaxies used

v_i : radial velocity of the galaxy

R_i : radial projected distance from the group center

$$R_0 = \left(\frac{8GT^2}{\pi^2} M_{dyn} \right)^{\frac{1}{3}} \quad (3.9)$$

with:

G : gravitational constant

$T = 14$ Gyr

M_{dyn} = dynamical mass of the group

For the calculation of the dynamical mass (equation 3.8) and the radius of the CGs (equation 3.9) galaxies, which are listed in Tables C.1 to C.5 were used. Galaxies were chosen, which lie in an interval of $v_c \pm 500$ km/s, where v_c is the velocity of the group center, determined by Hickson (1982). These galaxies were pre-selected in NED lying less than 2 Mpc around the HCG's centers. For the five sample HCGs Figure 3.19 shows the velocity dispersion of galaxies with respect to the median velocity of the original HCG galaxies identified by Hickson (1982). For HCG 16 88 % of the spectroscopically identified member galaxies do not only lie in an interval smaller than ± 500 km/s they also lie in an interval smaller than ± 300 km/s. 84 % of the spectroscopically identified galaxies of

HCG 19 lie in the ± 500 km/s interval, 100 % of the galaxies identified in HCG 30 lie within ± 300 km/s. 91 % of the galaxies in HCG 31 lie within the ± 500 km/s interval and 81 % of the galaxies of HCG 42 lie within ± 500 km/s.

Table 3.1 shows the dynamical mass M_{dyn} (column 3) and the radius R_0 (column 5) of the CGs for galaxies with velocity dispersions of maximum ± 500 km/s. As more than 80 % of the spectroscopically identified member galaxies show velocity dispersions smaller than 500 km/s, the dynamical mass and the radius of the zero velocity surface are more likely using velocity dispersions smaller than 500 km/s than including galaxies with velocity dispersions smaller than 1000 km/s. Column (4) and (6) show the statistical errors of the mass ΔM_{dyn} and the radius ΔR_0 . If few galaxies are available like in this case the error can be determined with $\Delta M_{dyn} \sim M_{PM}/\sqrt{N_m}$ (Heisler et al. 1985). In all cases the radius is much larger than ~ 2 Mpc and the dynamical mass differs by more than two orders of magnitude.

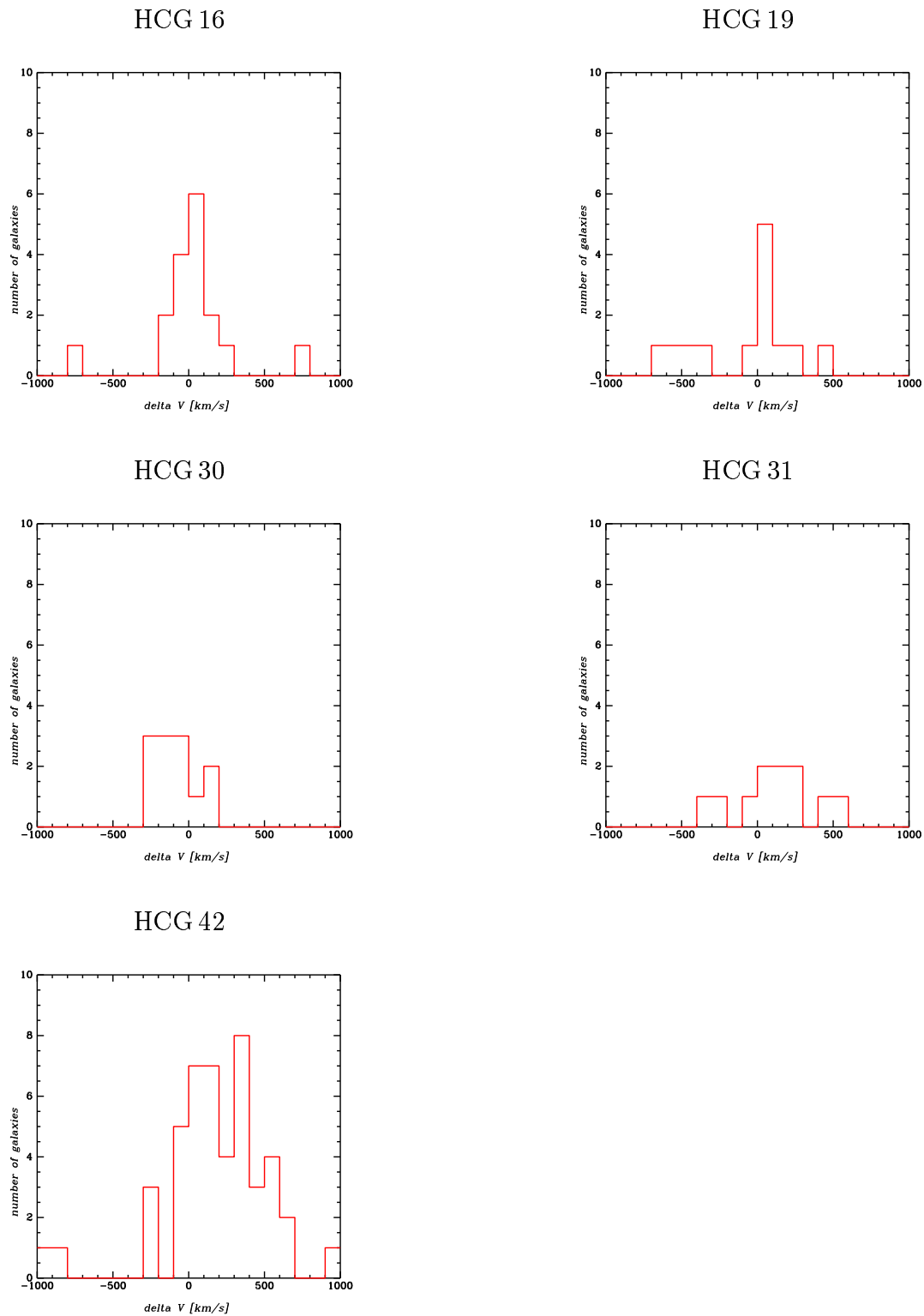


Figure 3.19: Distribution of galaxy velocities with respect to the median velocity of all cataloged group members (Hickson 1982)

Chapter 4

Discussion and conclusions

Dwarf galaxies in HCGs, especially in the outer regions, are rarely studied. Studies mostly concentrate on the few large galaxies in the group center. The main goal of this work was the identification of dwarf galaxy group members in the centers and in the outer regions of HCG 16, 19, 30, 31, and 42 for two reasons. First the nature of HCGs was determined using dwarf galaxies, because they are a good tracer of their environment and they are fairly abundant. Second the extension of HCGs could be determined in regard to the distribution of dwarf galaxies, if they are concentrated to the group centers or if they are distributed throughout the observed field.

Wide field mosaic data for the identification and examination of group member dwarf galaxies were used. The object detection and extraction was performed using the Source Extractor program. Approximately 300 – 5000 galaxy candidates in the mosaic images of the sample HCGs were identified. In order to select the dwarf galaxy candidates Source Extractor is limited to find objects larger than the physical size of the smallest Local Group dwarf galaxy. After this selection more than 200 dwarf galaxy candidates in each HCG were identified.

Since for only a few candidate galaxies radial velocities exist in the literature, the group membership was determined using selection criteria from both CMDs and structural parameters of the galaxies.

This classification made use of the fact, that dE galaxies form a distinct structure (red-sequence) in the CMD. The selection was finalized by examining morphology, surface brightness, and radial light profile of the candidate target galaxies lying in the red-sequence (section 3.1.2), allowing to exclude most background objects from the sample. The distribution of the selected dwarf galaxies in the central and in the outer regions was examined. Their colors, types, and sizes were studied to see if the high density environment of the CGs influences the morphology, luminosity, and brightness profiles of the dwarf galaxy population. With this population for the first time the LF for the HCG sample was determined including faint galaxies. Finally the mass and extension was calculated for the sample HCGs using literature data.

4.1 Dwarf galaxies in CGs

Results from the literature (see section 1.2.2 for more detail) suggest, that the number of member galaxies is larger than the number of the originally defined 3 to 5 HCG member galaxies. Contrary to the general assumption that CGs lack faint galaxies in this work a significant number of new high probability dEs (59 in HCG 16, 20 in HCG 19, 44 in HCG 30, 34 in HCG 31 and 25 in HCG 42) and high probability dIrr (9 in HCG 16, 4 in HCG 19, 6 in HCG 30, 11 in HCG 31 and 9 in HCG 42) galaxies in the HCG sample was found in addition to the few bright member galaxies. **More than 75 % of the total amount of the identified galaxies in each of the sample HCG are dEs** (87 % of the identified galaxies in HCG 16 are dEs , 83 % in HCG 19, 88 % in HCG 30, 75 % in HCG 31 and 86 % in HCG 42).

The membership of the high probability dwarf galaxies was determined using the CMD and structural parameters of the dwarf galaxies. It is known from galaxy clusters, that dE cluster member galaxies form a distinct structure – the red–sequence in the CMD (Conselice et al. 2002, 2001, Secker et al. 1997). This feature was used in order to identify HCG members. If HCGs are physically bound it is expected to find dE galaxies in the red–sequence. The CMD in Figure 4.1 shows the sum of all HCG CMDs (Figure 3.2– 3.6). The dashed lines represent the red–sequence and its 1σ error. The galaxies in this area were investigated concerning their membership (morphology, surface brightness, and radial light profile) as described in detail in section 3.1.2. Indeed a large number of member dwarf galaxies were found in HCGs. The red filled squares in Figure 4.1 represent all member galaxies and the blue squares represent all HCG field galaxies. The question is how the large fraction of dE galaxies may have evolved in a high density region like CGs? Examinations of dwarf galaxies showed, that dIrrs are mainly found in regions of low galaxy density - at the outer part of clusters, in LGs and in the field. dEs are predominantly found in areas of high galaxy density - in cluster centers (Cote et al. 1997, Thompson & Gregory 1993, Binggeli et al. 1990, 1987). Therefore it is assumed that the dense environment influenced the evolution of these galaxies, thus dwarf galaxies are a good indicator for their environment.

A large fraction of investigations of CGs show that group evolution affects galaxy evolution. It is known, as discussed in the introduction (1.1.2), how a group’s environment can influence a variety of galaxy properties for example the morphology. In physically bound systems like clusters, merging is very likely. The merging of two spiral galaxies of similar size leads to fluctuations in the potential well and to strong tidal forces, which destroy the stellar disc of the spiral galaxies. This leads to the formation of an elliptical galaxy where the regular motion of stars on radial orbits is destroyed. Galaxy clusters are therefore dominated by elliptical galaxies. Studies of CGs also showed, that the number of elliptical galaxies is larger than the number of spiral galaxies indicating that CGs are physically bound systems. Prandoni et al. (1994), Rood & Williams (1989), Hickson et al. (1988a), and Sulentic (1987) examined the morphology of galaxies in CGs and their environments and found that these groups contain fewer spiral and irregular galaxies than their neighborhood (see section 1.1.2). The formation scenario for elliptical galaxies is influenced by

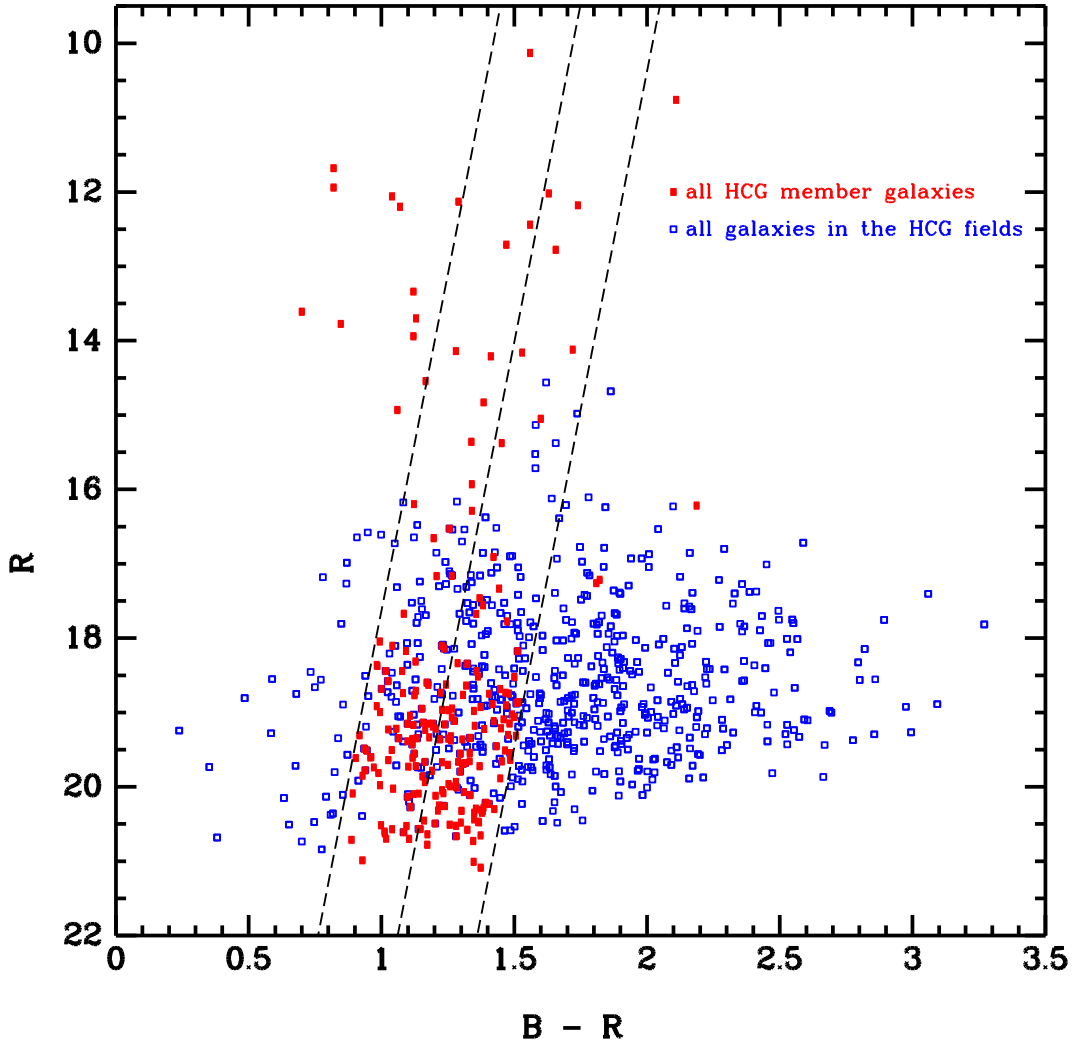


Figure 4.1: CMD of all HCG galaxies (HCG 16, 19, 30, 31, 42) divided into group member galaxies (red filled squares) and non member galaxies (blue squares). The dashed line represents the red sequence and its 1σ error

merging, but a different formation scenario is assumed for dEs in dense environments like clusters.

Grebel et al. (2003) explored the gas deficit of dE galaxies in the Local Group. It is surprising that these galaxies do not show detectable interstellar material, although they experienced star formation. They suggested that the bigger part of interstellar material from dSphs was removed by ram pressure stripping by gas in the galaxy halos and an inter group medium. Therefore X-ray gas is required in galaxy clusters and groups. Galaxy clusters contain a large fraction of X-ray-emitting gas (see section 1.1) within the gravi-

tational potential well. The requirements for the formation of dE galaxies, which exist in galaxy clusters are also found in HCGs.

Schwartz et al. (1980) first investigated X-ray emission from CGs. He found that the X-ray properties are similar to X-ray properties of rich galaxy clusters. Bahcall et al. (1984) were the first, who investigated Stephan's quintet concerning X-ray emission. The detected X-ray map revealed a diffuse emission and no concentration of the hot gas to the galaxies. Sulentic et al. (1995) showed that a large fraction of the emission can be associated with shock fronts and less with gas, which is concentrated in the group center. X-ray observations by Saracco & Ciliegi (1995), Sulentic et al. (1995), Pildis et al. (1995) and Ebeling et al. (1994) revealed hot gas in more than a dozen additional CGs .

Ponman et al. (1996) investigated X-ray properties of 85 HCGs and detected diffuse X-ray emission from 22 groups (also from HCG 16 and HCG 42, belonging to the HCG sample). Mulchaey & Zabludoff (1998) found the existence of diffuse X-ray emission from hot intra group gas in 75 % of HCGs.

Mulchaey et al. (2003) searched for diffuse X-ray emission in 109 nearby galaxy groups and found evidence for hot intra group medium in about half of them. Three of the sample HCGs (16, 31, 42) were detected in X-ray. However, the nearby groups were only detected to a fraction of the virial radius, thus a significant amount of the gas mass may be found beyond the radius of the X-ray detection.

All requirements like in galaxy clusters are given, thus it can be assumed as one possibility that the identified dE candidates in the HCG sample were formed due to ram pressure stripping. Other results strengthen this assumption. With observations of HI at 21 cm it is possible to reveal the mass distribution of cool galactic and intergalactic gas. Williams & Rood (1987) concluded from their results (median HI mass $\approx 2.2 \times 10^{10} M_{\odot}$), that CGs have a deficit of HI compared to LGs. The result is consistent with a deficit concerning the radio emission, which was found in the disks of spiral galaxies of CGs as mentioned by Menon (1995). This result suggests that the interactions taking place in CGs have removed a huge fraction of the gas from the galaxies. It also points to ram pressure stripping, where the gas is removed from dIrr galaxies and dEs were formed.

4.2 The Luminosity Function

The analysis of the LF of HCGs in section 3.6 shows that there is a steep increase towards the low-luminosity end (Fig 3.18) discarding all data points beyond the limiting magnitude of -12.5 mag. Further the distribution followed roughly the fits calculated by Sandage et al. (1985) for the galaxy content of the Virgo Cluster. In the case of the fit to SDSS galaxies calculated by Blanton et al. (2001) also a rise towards the faint end of the distribution can be observed (dashed-dotted line in Fig 3.18) but with a clearly smaller slope than the fits (dotted line and solid line in Fig 3.18) published by Sandage et al. (1985). In the latter case it can be seen that the LF, fitting the dwarf galaxy population in the Virgo Cluster (dotted line), is steeper than the LF comprising all galaxies.

Apart from the fact that the LF of HCGs determined in this thesis has the steepest slope

(Fig 3.18) it is in good agreement with the result of Sandage et al. (1985), who showed that the faint end of the LF is dominated by dE galaxies. In fact the slope of the LF fitting the dE population in the Virgo Cluster ($\alpha = -1.35$) is the largest one of the three comparison distributions used and approximates best the slope of the observed distribution. This fact shows that the faint end of LFs in dense environments is dominated by faint galaxies (namely dwarf galaxies) and that low-luminosity galaxies are much more numerous in dense environments than in diffuse ones. Furthermore this implies that HCGs have a much higher number density of dwarf galaxies per giant galaxies than galaxy clusters. Sandage et al. (1985) concluded that giant galaxies and dEs are separate families with no continuity between them. Flint et al. (2001) investigated the Leo I and Coma I Groups at ~ 10 Mpc in order to study the galaxy LF at $z = 0$. Unfortunately their membership assignment of the galaxies to the groups is still preliminary. They presented a histogram of detected objects versus absolute total magnitudes of galaxies identified in the Leo I Group. These data are used in order to compare the number of dwarf galaxies per magnitude interval of the Leo I Group with the distribution of the HCG galaxies (Figure 4.2).

Although it is not a robust measurement of the distribution of galaxies versus magnitude, as remarked by the authors, it shows strong similarities with the thesis result having nearly the same slope at the faint end for $B \geq -15$ mag. As can be seen in the diagram (Figure 4.2) the distribution of the data points rises steeply up to a total magnitude of -10 mag reaching their completeness limit at that magnitude.

The investigation of Flint et al. (2001) also shows that the steep increase in the study of the distribution at faint magnitudes is not biased by mis-identifications of background galaxies since in both cases a similar distribution is detected independently. Furthermore the fact that the data points of the HCGs and the Leo I Group show nearly the same increase implies that these groups have nearly the same population and further the dE galaxies have the same formation history. Another study of the Virgo Cluster was done by Trentham & Hodgkin (2002). In that work the LF for the Virgo Cluster was measured between $B = -22$ and -11 improving the detection of faint galaxies. They found that the LF rises only gradually for $-22 \leq B \leq -16$ and that it rises steeply for $-16 \leq B \leq -14$ with $\alpha \sim -1.6$. This LF is similar to the LF determined for the Virgo Cluster by Sandage et al. (1985). In this work LFs determined by Sandage et al. (1985) are used, because Trentham & Hodgkin (2002) did not determine a LF explicitly for dwarf galaxies like Sandage et al. (1985) did. The studies focusing directly on CGs (and not on clusters) are not numerous and suffer from the fact that their observations are not deep enough. This is the reason for the different fits.

Heiligman & Turner (1980) were the first who determined the LF of CGs. Investigating a sample consisting of Stephan's Quintet, Seyfert's Sextet and further eight CGs from the Arp and Vorontsov-Vel'Yaminov (Arp 1966, Vorontsov-Vel'Yaminov 1977) catalogs they found that CGs contain fewer faint galaxies than a field galaxy sample does. Hickson (1982) determined the LF in HCGs and Kodaira et al. (1991) determined the LF in some Shakhbazian groups and they found similar results as well as Ribeiro et al. (1994). These results are in contrast to the ones of this thesis which show that CGs contain more faint galaxies than a field galaxy sample does. Their conclusion can be explained by the fact,

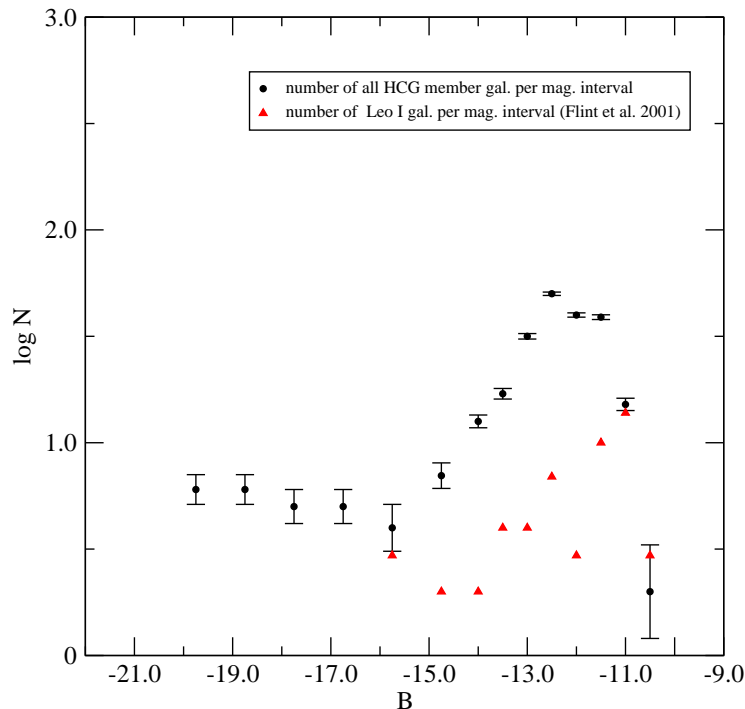


Figure 4.2: The diagram represents the number of detected galaxies per magnitude interval in the HCG sample (see Figure 3.18) and the Leo I group investigated by Flint et al. (2001). They applied a preliminary morphological membership classification for the data. The circles represent the HCG galaxies and the triangles represent the galaxies identified in the Leo I Group.

that their selection is limited by the 3 mag range of the selection criterion defining HCGs. Further Prandoni et al. (1994) pointed out that CGs are biased by their small magnitude range. Thus faint galaxies are not included in their sample of HCGs like also in the study of Zepf et al. (1997) who derived the LF of galaxies in CGs down to only a magnitude $B = -15$. A study confirming the thesis results has been done by Barton et al. (1996) who estimated the LF for the RSCGs and found that the derived LF is inconsistent with the LF of field galaxies.

Most of the LFs for CGs described in the literature are similar to LFs of a field galaxy population. The thesis results reveal that this has to be handled with care since in the preceding studies of CGs little attention was paid to the importance of the faint galaxy population. The comparison of the sample LF with the ones of Sandage et al. (1985)

and Flint et al. (2001) showed the clear relation between the rise of the LF towards faint magnitudes and the number of dwarf galaxies in the analyzed area.

The above discussed LF of HCGs, especially the result detecting a high number of dwarf galaxies, can give important clues to the understanding of the hierarchical model. In the CDM theory it is predicted that there should be many low-mass halos (Klypin et al. 1999). The small systems form earlier and collapse occurs at progressively large scales with small halos merging into larger units. During that process many of the low mass halos survive. Thus there should be much more dwarf galaxies than giant galaxies (Klypin et al. 1999, Moore et al. 1999). Tully et al. (2002) have suggested, that the dark halos in dense environments formed early in the history of the Universe, but that the dark halos in diffuse and unevolved environments assembled much later. Hence the dark halos in evolved environments, such as the Virgo Cluster, could collect gas that could later be turned into stars, but dark halos in unevolved environments could not. As a result more dwarf galaxies per unit total mass in evolved environments could be found than in unevolved environments. Further Trentham & Tully (2002) determined the galaxy LF in five different local environments. They found, that in all cases fewer dwarfs were detected than the numbers of low-mass halos anticipated by CDM theory. The steep rise of the HCG member galaxies data points (Figure 3.18 and 4.2), which is due to the large number of identified dwarf galaxies, strengthens the predicted value of $\alpha = -1.8$ by CDM models as they are steeper than the data points of the LF of the Virgo Cluster.

In fact the logarithmic slope of the analytically derived low-mass end of the CDM mass function, which is equivalent to the LF derived in section 3.6, is close to $\alpha = -1.8$. Determining this slope is very important in verifying cosmological models that make predictions about the number of galaxies of various types at the current epoch. From this theoretical point of view, it is highly interesting to study the amount of dwarfs versus large galaxies in the dense environment of CGs since the tidal field and galaxy mergers are expected to modify in particular the faint end of the galaxy LF (Benson et al. 2003).

From the presented investigation of the LF of HCGs it is confirmed, that HCGs are more similar to galaxy clusters than to the field in regard to the distribution of galaxies at the faint end of the LF. This represents a further argument for HCGs being physically bound systems rather than chance configurations of (field) individual galaxies.

4.3 Density and spatial distribution

Through the investigation of the density distribution and the spatial distribution of the HCG member galaxies it is possible to get information about the extension of the HCG and substructure within it and thereby to achieve deeper insight in their formation mechanism. The study of the azimuthally averaged density distribution for all member galaxies (spectroscopically identified ones, dEs, and dIrrs, Figure 4.3) showed, that for all sample HCGs a distinct density peak exists in the center decreasing towards the limit of the mosaic images. There is only one case (HCG 16) in the sample, where the density peak is slightly

offset from the region marked by the originally detected member galaxies. Results for each of the five sample HCGs are shown in Figure 4.3, where on the horizontal axis the radial distance from the group center and on the vertical axis the number of galaxies per unit area is plotted. To allow a comparison with previous results the number of galaxies per unit area was normalized to the number of the originally identified HCG member galaxies (Hickson 1982).

In the case of HCG 16, 19, and HCG 31 the central area is dominated by the original HCG galaxies, because there is no change in density to the value preceding the study. The diagrams for HCG 30 and 42 show, that additionally further galaxies, namely dE and dIrr galaxies, were found in the central area of these HCGs. Three HCGs (16, 30, and 42) can be grouped together as they have a slow decrease in the density distribution towards the outer parts of the HCG. In contrast HCG 19 and 31 exhibit a nearly constant density distribution apart from the strong peak in the center. However, the density distributions give evidence that HCG member galaxies show indeed a concentration towards the group centers.

Due to the lack of radial velocities, the membership of the galaxy candidates of the HCGs could not be confirmed definitely. For HCG 42 a minimum number of 12 ± 3 additional group members is determined using the flat density distribution of background galaxies. Comparing the results of the density distribution of HCGs with the results obtained for galaxy clusters, it is found that the density distributions of HCG 16, 30, and 42 best fit with the result of galaxy clusters. In both cases dwarf galaxies are more numerous in the group centers than in outer regions. As discussed in section 4.1 almost 80% of the dwarf galaxies in all analyzed HCGs can be classified as dEs confirming strongly the assumption that HCGs are physically bound systems. Examining the distribution of dwarf galaxies in the Coma Cluster (Thompson & Gregory 1993) and the Virgo Cluster (Ferguson & Binggeli 1994, Binggeli et al. 1993, 1987) it was found that dEs also compose the largest number fraction of galaxies in the cluster core.

From the spatial distribution of dEs and dIrrs it is possible to draw conclusions for the process responsible for their formation. The study of the spatial distribution of galaxies in the HCG sample showed, that in two CGs (HCG 16, 42) dEs and dIrrs have an elongated distribution throughout the field. This result is a confirmation of the observation showing that the spatial distribution of the giant galaxy members in the HCG show an elongated, chain like shape (Tovmassian et al. 1999). Tovmassian et al. (1999) revealed further that radial velocity dispersions of HCGs correlate with the elongation of groups. The higher the elongation of the group, the smaller the radial velocity dispersions are. The dependence of the radial velocity dispersions of HCGs on their elongation proofs that HCGs are real, physical bound systems with their members rotating around the gravitational center of the group. The elongation found in HCG 16 and 42 also correlates with the distribution of X-ray emitting gas where an accordance between the position of dwarf galaxies and X-ray emission was found. For the remaining sample CGs no X-ray measurements are available. Mulchaey et al. (2003) found that the morphology of the X-ray emission of HCG 16 is irregular and not centered on a particular galaxy, but shows a slight alignment in diagonal

direction across the CG center. This covers roughly 50% of the dwarf galaxy candidates. The X-ray emitting region found in HCG 42 has a nearly symmetrical morphology and is almost concentrated to the group center implying that the group is virialized. A fraction of $\approx 40\%$ of the dwarf galaxy candidates of HCG 42 lie in the region of the detected emission.

Independently from the detection of X-ray emission Tovmassian & Chavushyan (2000) showed that the accordant redshift galaxies in the environment of a dozen studied HCGs and poor groups of galaxies are distributed in narrow strips of a few hundred kiloparsec in width. The dependence of the radial velocity dispersion of faint galaxies in the environment of HCGs on the elongation of the group is a clear hint that members of the surrounding structure are gravitationally bound to the corresponding HCGs.

In galaxy clusters, as explained in section 1.2.1, most of dEs are found in the group centers while dIrrs are found in the outer regions. The spatial distribution of dwarf galaxies in the sample HCGs argues in contrast for a uniform distribution of these galaxies.

Investigating substructures in groups, like concentrations of dwarf galaxies in a spatially restricted area, it is possible to provide constraints to the evolution of galaxy groups. Therefore the sample CGs were analyzed in regard to possible substructures within the area covered by it. Further the surrounding regions of the five HCGs were studied to determine if they form themselves a substructure inside a larger structure like e.g. a LG.

As described in section 3.5, galaxy count methods were used in order to find any substructure in the CGs. Apart from the concentration of galaxies in the group center substructure was detected in HCG 16, 31, and 42 (60% of the sample). The remaining groups do not show any concentration expect from the central one.

A comparable study was done by Zabludoff and Mulchaey (1998b) analyzing six nearby poor groups of galaxies with more than 30 spectroscopically confirmed members and X-ray halos extending out to radii of $\sim 200 - 300 h^{-1}\text{kpc}$. They could detect substructures in two cases ($\approx 33\%$ of their sample). These structures lie $\sim 0.3 - 0.4 h^{-1}\text{Mpc}$ outside of the center of the group.

The present study of the density and the spatial distribution of member galaxies in HCGs revealed that dEs and dIrrs are found still in a large number at the edges of the mosaic images. In these parts even some of the spectroscopically identified member galaxies were found. Hence it is very likely that the sample HCGs are more extended than the limits of the mosaic images. The five used HCGs were observed only up to a limit of $\sim 0.2 - 0.25 h^{-1}\text{Mpc}$ according to their definition establishing a concrete value for their extension (see 1.1.1.). Comparing the observed region of the sample HCGs with that one of Zabludoff and Mulchaey (1998b) it is therefore not surprising that no clear separation between the distribution of dEs and dIrrs could be detected. However, it is quite remarkable that despite the small observed region of the sample HCGs, a detection of substructure could be shown for 60% of the investigated HCGs. The fact that not in all of the analyzed HCGs and that not in all poor groups investigated by Zabludoff and Mulchaey (1998b) substructures were detected, strengthens the notion of Diaferio et al. (1994), Rampazzo & Sulentic (1992), Cavaliere et al. (1991), White (1990) and Barnes (1989). In their point of

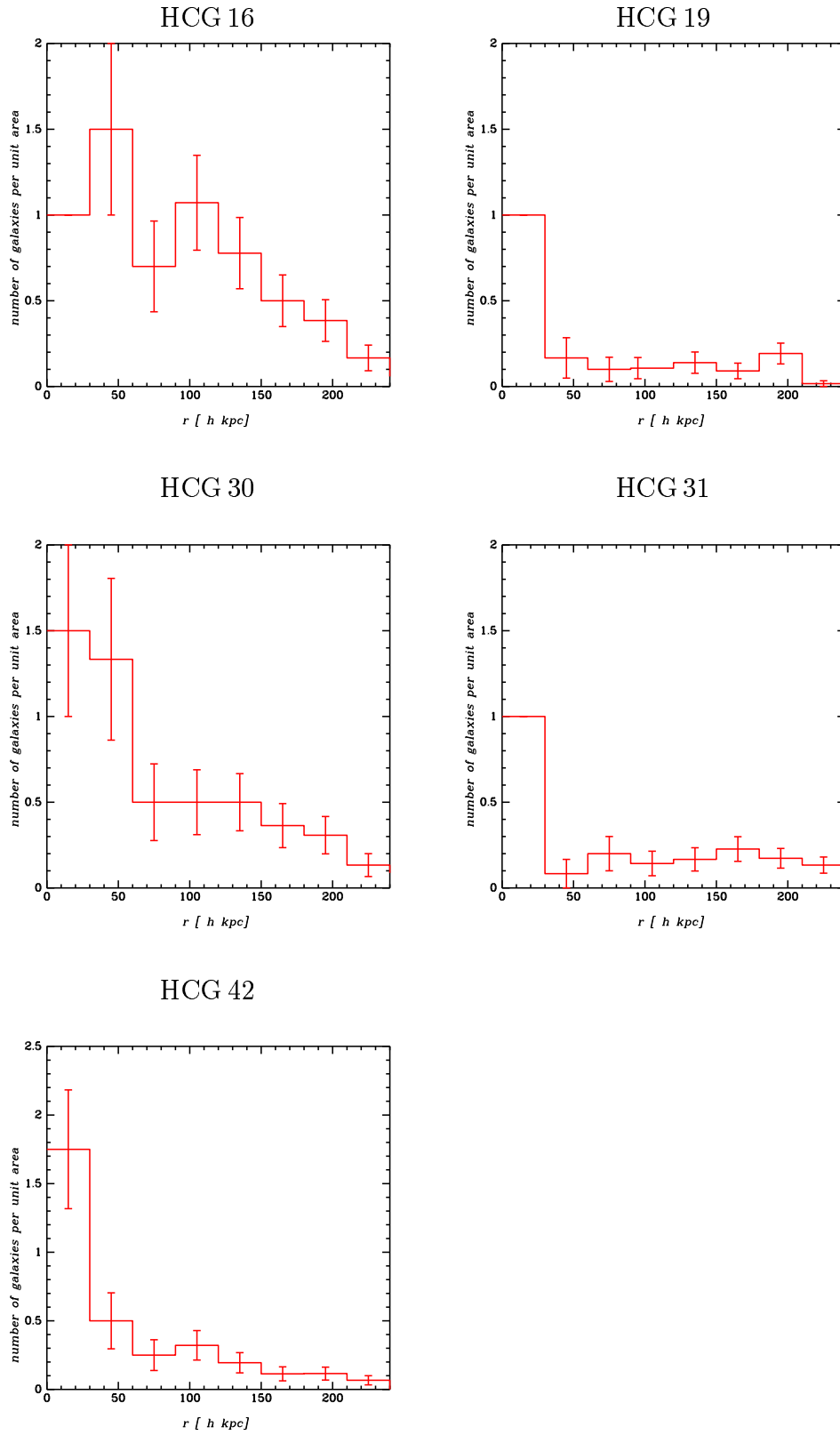


Figure 4.3: Density distribution of all member galaxies in the sample HCGs

view CGs represent a transient position between individual galaxies, pairs of galaxies and LGs rather than forming a distinct class of objects as mentioned by Sulentic (1987).

The detection of substructure inside HCGs suggests that HCGs could as well be a substructure within a larger one. In fact the large (unexpected) extension of the HCGs and the observation, that at the limits of the fields dEs and dIrrs were found, points to HCGs being embedded in larger structures.

Analyzing this question Rood & Struble (1994) determined that roughly 70% of HCGs could be found in the boundaries of LGs and clusters and Vennik et al. (1993), who compared the spatial distribution of the nearest compact and LGs, claimed, that all CGs are not isolated but are condensations within LGs. A similar statement is given by Barton et al. (1996), Garcia (1995), Sakai et al. (1994), Ramella et al. (1994) and Vennik et al. (1993) investigating the distribution of galaxies in redshift space. They suggest that CGs are condensations within LGs or filaments. Further Barton et al. (1996) studied the velocities of galaxies surrounding the RSCGs in order to explore the embedding of these groups and they found that most RSCGs are included in dense environments and that their distribution follows the large scale structure. Another approach was used by Montoya et al. (1996). They investigated light profiles of 42 HCGs containing four group members and found a core radius of $6 h^{-1}$ kpc for a King model. If CGs would be chance alignments within LGs no King model could be fitted to the light profile at all. The detection of galaxy associations within the context of larger structures (as substructure in HCGs and HCGs inside LGs) matches quite well the scenario developed in the hierarchical model, that smaller objects reassemble to groups or merger to larger ones. It shows how the hierarchical model works also in the context of dense environment as in a common potential well (Ramella et al. 1994, Barnes 1989). This formation mechanism is also predicted by N-body simulations of rich groups of galaxies (Diaferio et al. 1994). The results showing that the dwarf galaxy content of the HCGs does not fall off completely fits into this scenario so that HCGs can be described as physically bound systems in larger ones like LGs. Further the dominating fraction of dEs ($\approx 80\%$) among the detected dwarf galaxies is a confirmation of the existing models describing the influence of dense environments on galaxy evolution.

4.4 Mass and radius

From the results of the spatial density distribution of the sample HCGs it was found, that HCGs extend far beyond the centers of cataloged HCGs and that their limits were not reached yet. Thus the next step is to determine their masses and extensions. In order to estimate the mass of the groups the projected mass estimator was used, which is discussed by Heisler et al. (1985) (section 3.7). To determine the extension of the whole CG first the dynamical mass had to be estimated using velocity information of member galaxies. For the sample HCGs literature data were available for few galaxies lying at a projected distance of 2 Mpc around the center of the HCGs and with velocities within 500 km/s of the median group velocity. The radius of the zero-velocity surface (R_0 , see section 3.7)

HCG	N_m	M_{dyn} [$h^{-1}M_\odot$]	R_0 [$h^{-1/3}$ Mpc]
16	15	$\sim 6 \times 10^{12}$	~ 1.6
19	11	$\sim 1 \times 10^{14}$	~ 4
30	12	$\sim 4 \times 10^{13}$	~ 3
31	10	$\sim 1.5 \times 10^{14}$	~ 4.7
42	37	$\sim 7 \times 10^{13}$	~ 3.6

Table 4.1: Dynamical mass (M_{dyn}) and the radius of the zero-velocity surface (R_0) for the sample HCGs (with spectroscopically identified member galaxies (N_m) in an area of 2 Mpc around the center and a velocity dispersion smaller than 500 km/s to the group median velocity)

was calculated using the method described in Sandage (1986). The result is that in all sample HCGs the calculated radius for each individual CG is apart from HCG 16 larger than 2 Mpc, ranging from 3 to 4.7 Mpc. The values for the dynamical mass range from $M_{dyn} \approx 10^{12}$ to $10^{14} h^{-1}M_\odot$ differing in their minimum and maximum by two orders of magnitude, see Table 4.1.

It is remarkable that the HCGs (HCG 19 and HCG 31) with the highest calculated mass and hence the highest R_0 radii, are the HCGs which show a flat galaxy density distribution within the CG (section 3.6). Nevertheless, the high mass of HCGs reveals, that these systems are DM dominated. The first hint to the existence of DM in galaxy systems was given by Limber & Mathews (1960). They found that the velocity dispersion of CGs is higher than it would be expected concerning their visible mass and showed that the virial theorem could be satisfied for Stephan’s Quintet, if the galaxy masses were larger than the masses of isolated galaxies and would exist in a non-visible form.

Numerical simulations strengthen the existence of a DM halo. As mentioned in the introduction a CG would collapse on a timescale much smaller than the Hubble time and the member galaxies would merge and form a large elliptical galaxy (e.g. Diaferio et al. 1994, Barnes 1989) due to the small velocity dispersion of the galaxies. This problem can be solved by varying the fraction of DM distributed in the groups assuming a massive, not excessively concentrated DM halo (Athanasoula et al. 1997). Further Diaferio et al. (1994) and Barnes (1989) showed that the small crossing times of HCGs produce no problem if the groups are formed in dense environments (e.g. LGs). This can be supported observationally as in section 4.3 it was evidenced (by the distribution of dwarf galaxies) that the sample HCG seem to be embedded in a larger structure (LGs).

With the observation of the regions between the HCGs’ member galaxies in different wavelength regimes further confirmations for a DM halo can be achieved. Ponman & Bertram (1993) found common envelope material from X-ray observations and Verdes-Montenegro et al. (2001, 1997) observed atomic hydrogen. They showed in HCG 49 that the HI com-

mon envelope is rotating with a high symmetric pattern, following a large-scale potential that is not due to any particular galaxy member, whereas Puche & Carignan (1991) found, studying the dynamic of LGs, that the DM corresponds to the individual member galaxies. However, X-ray observations show that gas and DM is more extended and not implicitly related to the galaxies in a large number of CGs. The presented results (Table 4.1) support explicitly that the sample HCGs are embedded in large common halos.

Clues to the overall structure of the Universe may be derived by the investigation of small galaxy groups. Groups of galaxies after clusters of galaxies are the second largest virialized systems. One of the outstanding questions in cosmology is the evolution of structure on different mass scales. It is almost clear, that galaxy clusters evolve from the accretion of smaller groups (Zabludoff & Zaritsky 1995, Böhringer et al. 1994, Binggeli et al. 1993, White et al. 1993, and Briel et al. 1992,). Concerning galaxy groups Zabludoff & Mulchaey (1998a) concluded from their study that at least some galaxy groups accrete smaller structures.

The results of this work strengthen this view of structure formation. From the analysis of the spatial and density distribution in section 4.3 it was proven that dwarf galaxies are the most abundant type of galaxies in HCGs. In particular dEs are the most representative type. The distribution of the dwarf galaxy population shows in the majority (60%) of the analyzed HCG sample a decrease towards the limits of the CG. Hence it is concluded that HCGs are bound systems revealing also the similarity with galaxy clusters harboring smaller objects which surround the giant galaxies. The high number of dEs, representing the majority of the HCG' member galaxies, corroborates the previous statement since they are known to form and evolve in dense environments. Further the density distribution revealed a much more extended region covered by the HCG than known before, detecting at their limits still a high number of dwarf galaxies. In this thesis also indications were found pointing to the formation of substructures in HCGs which further strengthen the view of a HCG as a physically bound system.

As shown in section 3.6 and discussed in section 4.2 the observed LF of all sample HCG galaxies evidences a steep rise at the faint end of the LF. This is due to the dominating fraction of dwarf galaxies among all HCG member galaxies. The comparison with LFs of a field environment and of a cluster indicates that the LF of the HCG has a large similarity to that one of a cluster environment. Moreover, the slope of the faint end exceeds that one of the comparison cluster LF and is in good concordance with values obtained from Cold Dark Matter (CDM) theory (low-mass end of the CDM mass function). Further similarities between HCGs and clusters were revealed analyzing the mass content of the CGs and deriving their probable extension. All derived masses for the sample HCGs are noticeably higher than the galaxy members total mass would suggest and indicating to a large common halo for the HCGs. This observation is a strong evidence that HCGs are physically bound systems being quite similar in their nature to galaxy clusters.

All the presented results of this work show that a large part of the analyzed HCGs is formed by evolution of small structures to larger and physically bound systems according to the hierarchical model.

Chapter 5

Outlook

The analysis of the number of dwarf galaxies in groups is a key question of the present investigation of galaxy formation in CDM models in comparison with observations. With a spectroscopic study of the high probability dwarf galaxy candidates (20 to 59 in each sample HCG) their membership can be proven definitely. Furthermore the spatial density distribution and the LF can be verified, especially if the observed region is extended beyond the limits applied before. The extension of the observed region in HCGs provides also a more reliable way of searching and defining possible elongated or filamentary structure along the line of sight. With the spectroscopic study of the dwarf galaxy population in the CGs a large variety of data will be available additional to morphological and surface brightness data, projected galaxy positions and radial velocities. Using that database the mechanisms driving dwarf galaxy formation and evolution can be studied in detail as well as the general dependence of galaxy formation in groups and the field (e.g. Gottlöber et al. 2002). Based on the large number of HCG members and their radial velocities it is possible to calculate a more accurate value for the HCG mass and a radius quantifying the spatial extension. In the next step these studies could be completed with simulations estimating the possible dynamical state of HCGs. The data can further be used to verify cosmological N-body simulations of group formation and the probability of kinematic substructure obtained through it (e.g. Knebe & Müller 2000, 1999). A detailed kinematical study of the giant member galaxies would also offer the possibility to investigate interactions and mergers and the frequency of their occurrence. Merger rates can give then an estimation about the timescale on which HCGs evolve (in their centers).

In order to analyze the frequency of conglomerations like HCGs a study using random distributions of galaxies in a dense environment can be done. Such kind of investigation would simulate the circumstances for galaxies in LGs and therefore give clues to the frequency of the occurrence of HCGs in LGs. Some authors suggest that CGs are continuously formed within LGs (e.g. Diaferio et al. 1994) but no clear scenario is available yet. Closely related to the problem of the formation of HCGs in larger structures as LGs is the issue of the dwarf galaxy content in LGs. This thesis showed the predominance of dEs in HCGs but it is interesting if all or only a part of the dEs observable in CGs were formed inside the HCG structure. A comparison between the dwarf galaxy population of the HCGs and the

LGs would give more insight into this question.

Another interesting point is the examination of the FIR emission of HCGs using ISO¹–data to estimate the amount of star formation activity in the sample HCGs. The star formation activity can give clues to possible interaction between member galaxies of the group and to the evolution of galaxies within dense environments in general. Up to now the data are mainly based on data derived from the IRAS satellite. From a search of the Point Source Catalog Hickson et al. (1989b) identified IR sources in 40 HCGs finding that the FIR to optical luminosity ratio is greater in CGs than in isolated galaxies. However, these data have only a low resolution and therefore the assignment of the IR flux to the individual galaxies is very difficult (as argued e.g. by Venugopal 1995).

Hence a detailed study of the FIR emission would bring progress in understanding the differences between star formation of galaxies evolving in a dense environment in contrast to field galaxies.

¹ Infrared Space Observatory

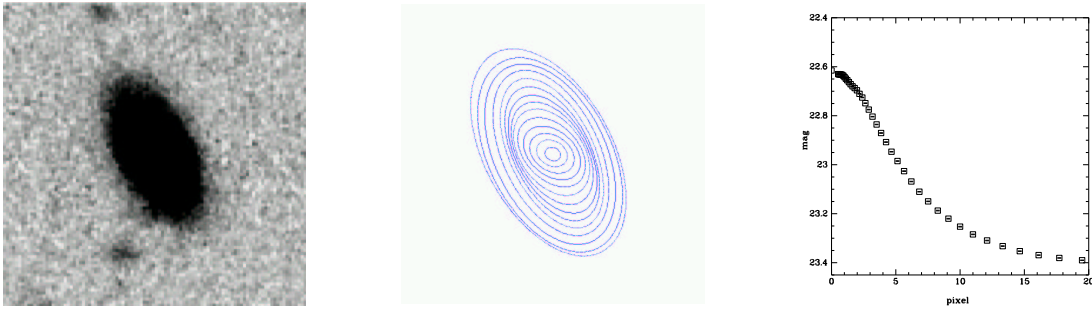
Appendix A

Selection examples for dwarf galaxies

Figures A.1 to A.5 illustrate the selection of galaxies in the sample HCGs with the example of HCG 16. Each high probability dwarf galaxy candidate of the red sequence of the CMD was investigated, because only few spectroscopically identified background galaxies lie in this area. The dwarf galaxy candidates were investigated concerning their morphology, isophotes, and radial light profiles. The first column of Figure A.1 to Figure A.5 illustrates the morphology of the galaxies in the R band. The second column illustrates the isophotes, which are in one to one correspondence with the images in column one (100×100 pixel, $23.3'' \times 23.3''$), and the third column illustrates the radial light profile (section 3.1.2 and 2.5.3).

Figure A.1 to Figure A.3 represent the **non-member galaxies**. Figure A.1 shows examples for background elliptical galaxies, Figure A.2 shows background edge-on spiral galaxies and Figure A.3 shows background spiral face-on galaxies. Figure A.4 and Figure A.5 show examples for identified **member galaxies**.

HCG 16–85947; (HCG 16–17, $v = 42493 \pm 18\text{km/s}$, de Carvalho et al. (1997))



HCG 16–15736

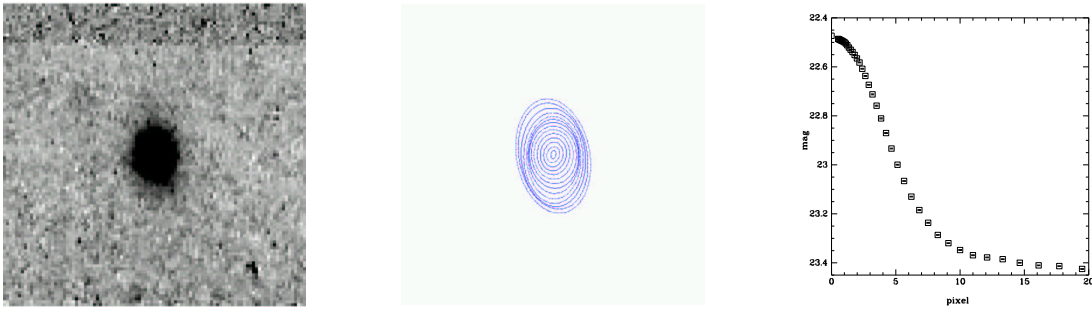
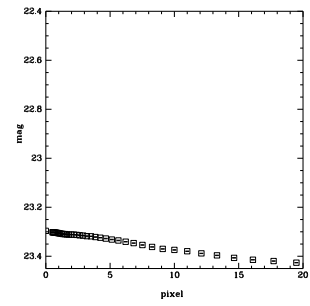
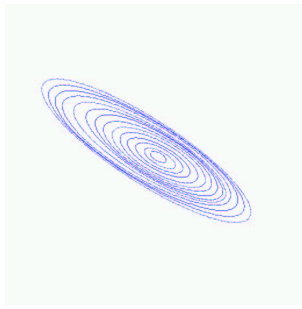
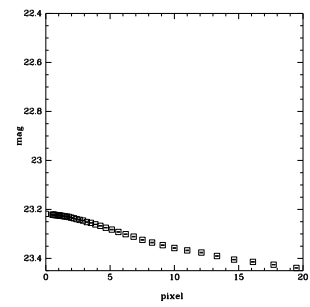
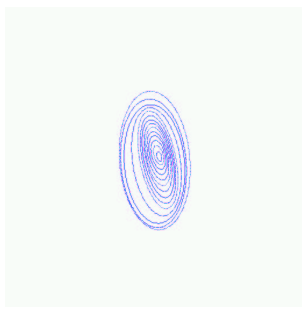
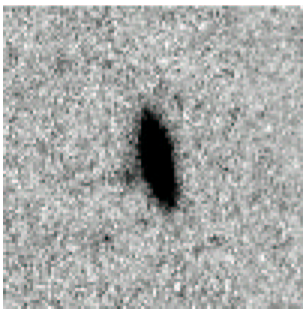


Figure A.1: Background elliptical galaxies - The elliptical galaxy in the first row was identified by de Carvalho et al. (1997). The galaxy in the second row was identified in the red sequence of the CMD of HCG 16. The first column shows the galaxy images in the R band, the second column shows the elliptical isophotes and the third column shows the radial light profile of the galaxies.

HCG 16–33914



HCG 16–37511



HCG 16–95513

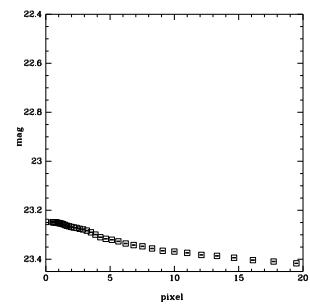
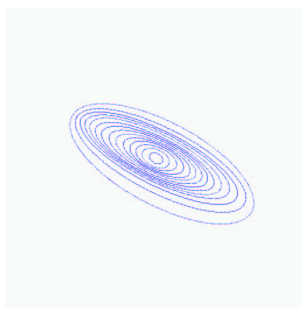
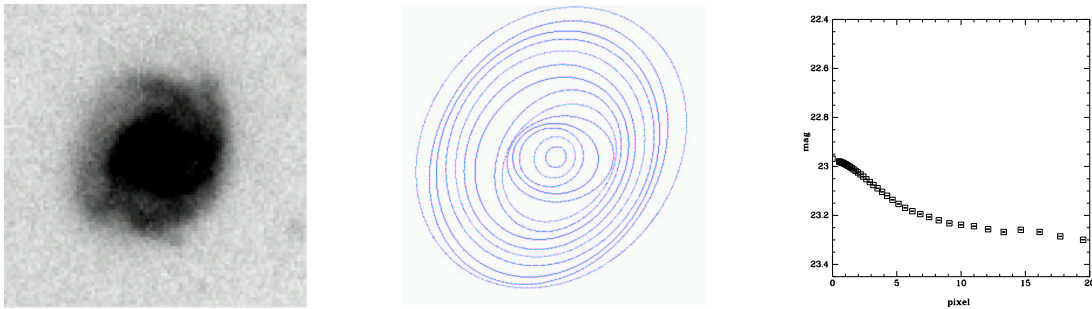
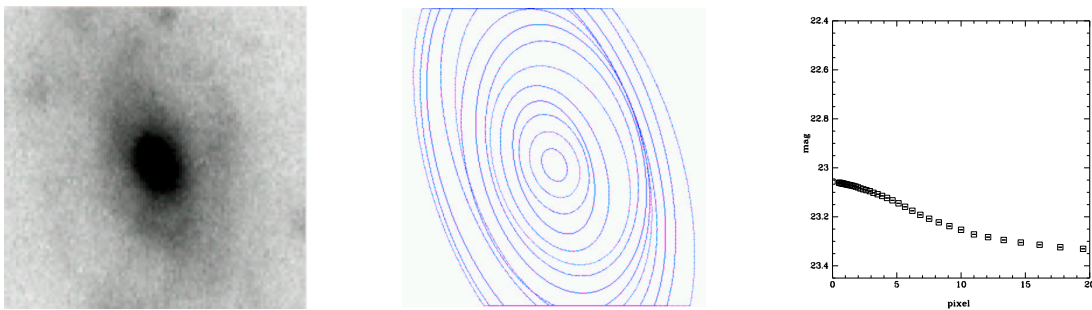


Figure A.2: Spiral galaxies seen edge-on identified in the red sequence of the CMD of HCG 16.

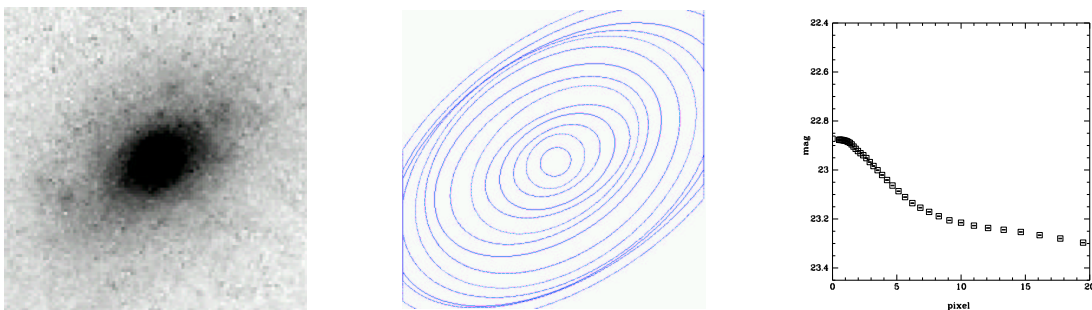
HCG 16-84426; (HCG 16-08, $v = 26165 \pm 39\text{km/s}$, de Carvalho et al. (1997))



HCG 16-44454; (HCG 16-07, $v = 10542 \pm 25\text{km/s}$, de Carvalho et al. (1997))



HCG 16-176718



HCG 16-114109

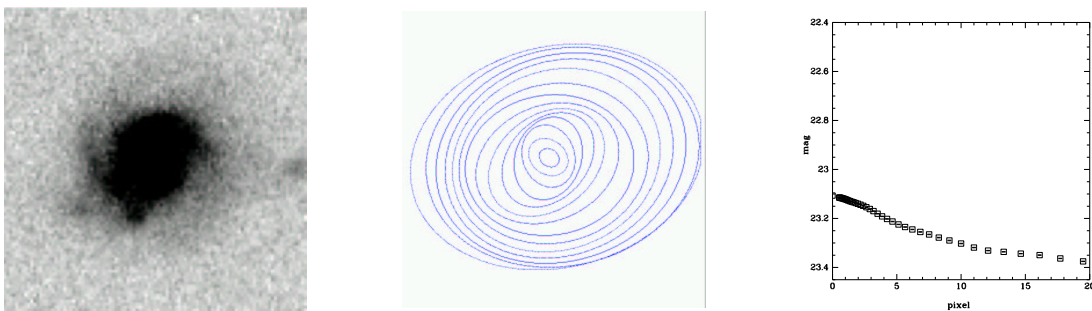
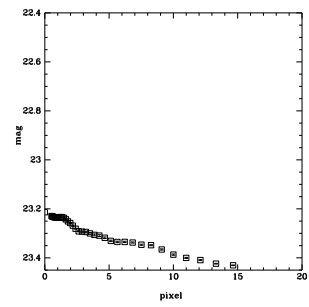
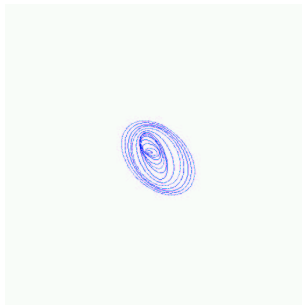
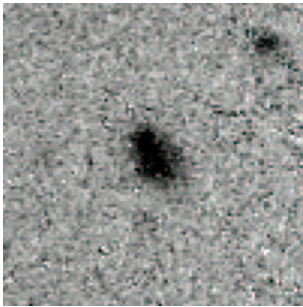


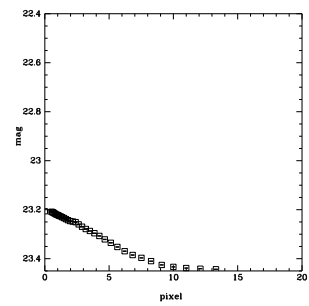
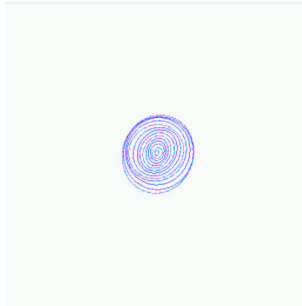
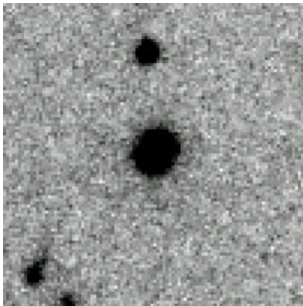
Figure A.3: Spiral galaxies seen face on - The first two rows show spiral galaxies, which were identified spectroscopically by de Carvalho et al. (1997). The last two rows show spiral galaxies, which were identified in the red sequence of the CMD of HCG 16.

SELECTION EXAMPLES FOR DWARF GALAXIES

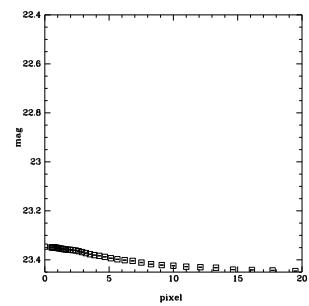
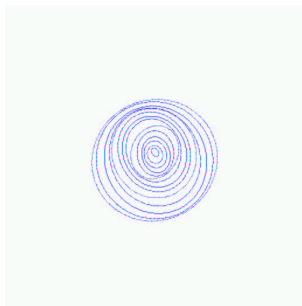
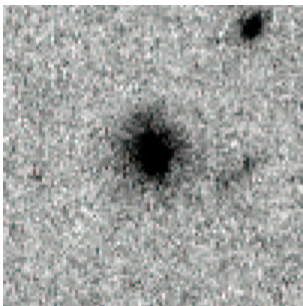
HCG 16–23573



HCG 16–31260



HCG 16–32239



HCG 16–49855

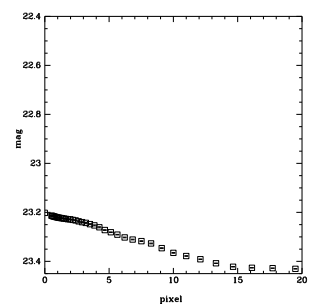
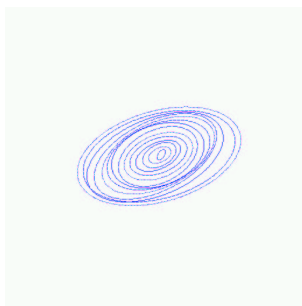
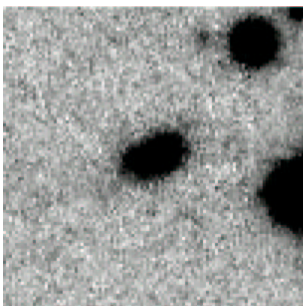
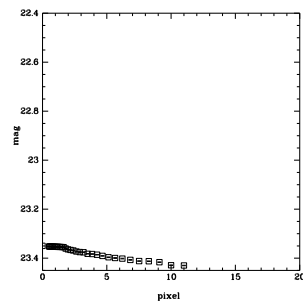
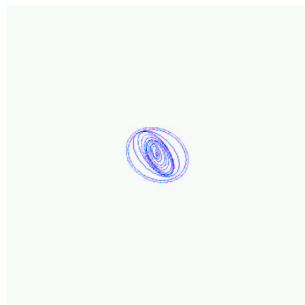
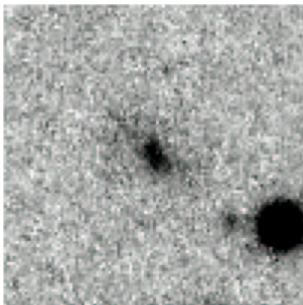
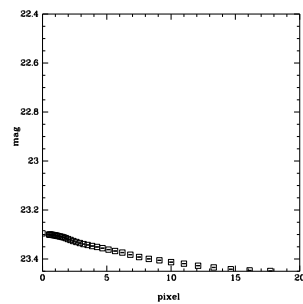
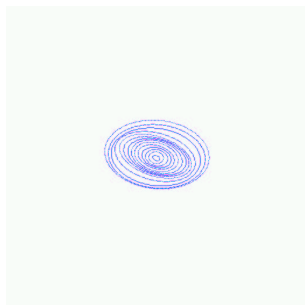
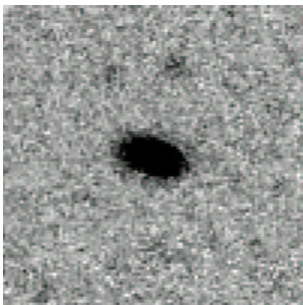


Figure A.4: Typical examples of high probability member galaxies of HCG 16 selected from the red sequence

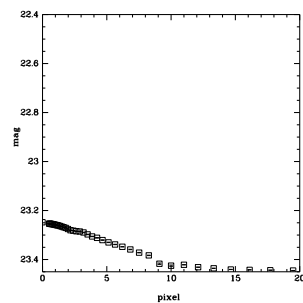
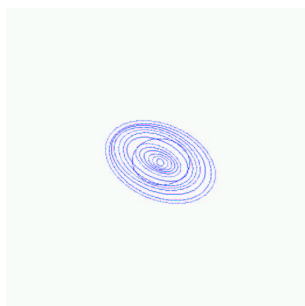
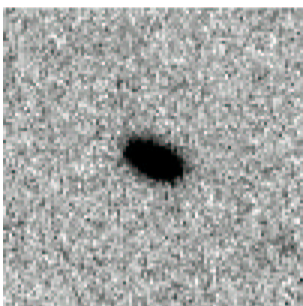
HCG 16-50506



HCG 16-70093



HCG 16-94489



HCG 16-150825

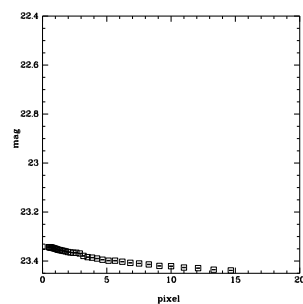
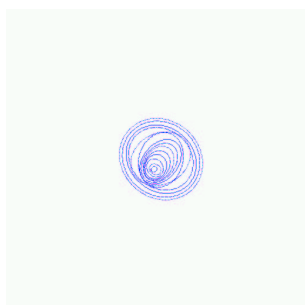
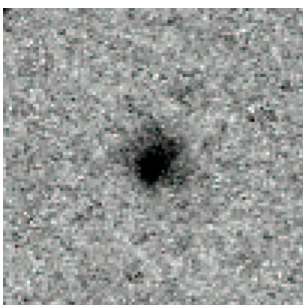


Figure A.5: Figure A.4 continued

Appendix B

Selected dwarf galaxies

Tables B.1 – B.10 list all identified dwarf galaxy members due to the selection criteria described in section 3.1.2. The dwarf elliptical member galaxies, which were determined in the red sequence of the appropriate HCG–CMD and the dwarf irregular member galaxies, which were identified bluewards of the red sequence of the CMD, are listed separately for each HCG.

The first column of each Table presents the numbers of the dwarf galaxies, which were given by Source Extractor (section 2.5.1). The second and third column gives the coordinates α_{2000} and δ_{2000} of the galaxies. Columns (4) to (7) present the B and R magnitudes of the galaxies and their errors. Column (8) presents all found literature data of these galaxies, which were derived from NED (APM; Maddox et al. 1990).

SELECTED DWARF GALAXIES

no.	α_{2000}	δ_{2000}	M_B	ΔM_B	M_R	ΔM_R	APM (BJ)
(1)	[hh mm ss]	[$^{\circ}$ ' '']	[mag]	[mag]	[mag]	[mag]	[mag]
	(2)	(3)	(4)	(5)	(6)	(7)	(8)
HCG 16-23573	2 8 25.81	-10 25 12.36	19.8802	0.0071	18.5172	0.0063	20.37
HCG 16-31260	2 9 7.92	-10 23 7.04	20.3739	0.0093	18.9045	0.0133	
HCG 16-32239	2 10 0.14	-10 22 59.92	20.3058	0.0208	18.8881	0.0114	
HCG 16-40727	2 8 45.88	-10 20 2.8	19.8666	0.007	18.6239	0.0081	20.30
HCG 16-49855	2 8 52.63	-10 16 41.48	19.0379	0.004	18.0446	0.0059	19.59
HCG 16-57081	2 9 57.92	-10 14 10.82	19.4429	0.0079	18.3144	0.0086	19.79
HCG 16-66737	2 9 54.73	-10 11 1.14	20.2005	0.0083	18.7336	0.0083	
HCG 16-69250	2 9 28.43	-10 11 30.98	19.1437	0.0051	18.1023	0.0059	19.78
HCG 16-71631	2 9 8.23	-10 9 45.86	19.803	0.0066	18.4448	0.0058	20.23
HCG 16-2724	2 8 40.26	-10 9 41.58	18.9411	0.0068	17.558	0.0061	19.34
HCG 16-78608	2 8 26.81	-10 8 32.71	19.8915	0.0085	18.767	0.0086	20.49
HCG 16-101772	2 8 43.05	-10 3 7.6	19.6235	0.0094	18.3369	0.0091	20.00
HCG 16-108615	2 9 36.03	-10 2 6.86	19.8974	0.0163	18.9153	0.0117	20.15
HCG 16-115465	2 9 59.77	-10 0 27.07	20.132	0.015	18.6852	0.0125	
HCG 16-120270	2 9 15.36	-9 59 36.13	19.9888	0.0108	18.994	0.0136	20.40
HCG 16-123390	2 9 27.20	-9 59 12.91	19.8198	0.009	18.7387	0.0105	20.45
HCG 16-123512	2 9 31.22	-9 59 2.38	20.22	0.0078	18.9683	0.0091	
HCG 16-134831	2 9 1.08	-9 57 26.24	20.1536	0.0155	18.7481	0.0129	
HCG 16-144630	2 10 19.14	-9 56 11.36	20.0715	0.0076	18.7642	0.0075	
HCG 16-147635	2 8 25.96	-9 55 48.98	19.957	0.008	18.638	0.0094	20.31
HCG 16-46263	2 8 53.02	-10 17 57.44	21.8105	0.026	20.6373	0.0266	
HCG 16-46667	2 8 38.79	-10 17 39.26	21.4988	0.0267	20.2594	0.0262	
HCG 16-48633	2 9 40.92	-10 17 8.27	20.8188	0.0141	19.312	0.0204	
HCG 16-50497	2 9 22.67	-10 16 14.63	21.7148	0.0335	20.6973	0.0417	
HCG 16-50506	2 8 52.77	-10 16 26.62	20.2732	0.0123	19.2173	0.0144	
HCG 16-55790	2 9 55.65	-10 14 30.44	21.2518	0.0348	19.9932	0.0218	
HCG 16-58863	2 8 48.54	-10 13 8.26	22.3544	0.0397	21.0075	0.0413	
HCG 16-66043	2 8 41.92	-10 11 11.15	20.5296	0.021	19.1784	0.0134	
HCG 16-66889	2 10 21.30	-10 11 0.13	21.213	0.0174	19.933	0.0331	
HCG 16-70093	2 9 16.06	-10 10 2.1	20.4013	0.0155	19.2362	0.017	
HCG 16-75847	2 9 43.01	-10 8 54.46	22.0268	0.0399	20.6535	0.0372	
HCG 16-76921	2 9 11.36	-10 8 46.25	20.2238	0.0112	19.3063	0.026	
HCG 16-77822	2 9 49.58	-10 8 33.61	20.973	0.0301	19.9785	0.0363	
HCG 16-94489	2 9 46.52	-10 4 36.05	20.608	0.0168	19.2213	0.015	
HCG 16-95082	2 9 23.25	-10 4 26.69	22.4612	0.0874	21.0872	0.075	
HCG 16-95238	2 8 56.70	-10 4 25.32	20.6295	0.0139	19.1469	0.0172	
HCG 16-96032	2 8 59.39	-10 4 18.48	21.6138	0.03	20.6018	0.0317	
HCG 16-97586	2 10 13.66	-10 4 8.11	20.6752	0.0119	19.343	0.0138	
HCG 16-98087	2 10 29.78	-10 3 52.81	21.2295	0.0185	20.0902	0.0199	
HCG 16-101314	2 8 27.54	-10 3 25.81	20.3258	0.0101	19.1495	0.0115	
HCG 16-103874	2 9 47.13	-10 2 39.84	21.0921	0.0264	19.7225	0.0239	
HCG 16-104020	2 8 50.92	-10 2 31.99	21.3188	0.019	20.0854	0.031	
HCG 16-105587	2 9 25.19	-10 2 17.84	21.0686	0.0263	20.0246	0.033	
HCG 16-107469	2 8 54.92	-10 2 4.74	20.667	0.0127	19.641	0.0151	
HCG 16-109273	2 9 49.43	-10 1 24.2	21.8438	0.0274	20.4762	0.0268	
HCG 16-109659	2 9 18.78	-10 1 23.23	21.8046	0.0589	20.7001	0.0607	
HCG 16-112406	2 8 38.82	-10 0 55.69	20.639	0.0114	19.377	0.0125	
HCG 16-114757	2 9 35.28	-10 0 47.81	20.3816	0.0162	19.1885	0.0191	
HCG 16-124637	2 8 24.97	-9 58 43.01	21.3796	0.0198	20.0696	0.0192	
HCG 16-126054	2 8 27.37	-9 58 35.68	20.8973	0.0171	19.6699	0.0162	
HCG 16-126163	2 8 59.37	-9 58 33.24	21.6138	0.025	20.4531	0.0284	
HCG 16-128045	2 10 24.79	-9 58 17.2	20.8499	0.0156	19.7204	0.0169	
HCG 16-132484	2 9 26.18	-9 57 42.32	20.2879	0.0098	19.1674	0.0187	
HCG 16-135654	2 8 46.44	-9 57 8.76	21.6961	0.0237	20.3465	0.042	
HCG 16-138140	2 9 6.53	-9 56 49.53	20.9767	0.0163	19.5117	0.0215	
HCG 16-141283	2 9 27.96	-9 56 27.25	20.8761	0.0172	19.5438	0.0144	
HCG 16-147436	2 8 38.02	-9 55 45.23	20.7791	0.0148	19.8504	0.0189	
HCG 16-149345	2 9 27.29	-9 55 41.65	20.9879	0.0178	19.6561	0.0151	
HCG 16-150825	2 8 42.54	-9 55 37.61	20.1507	0.0105	19.0438	0.0134	

Table B.1: High probability dwarf elliptical member galaxies of HCG 16

SELECTED DWARF GALAXIES

no.	α_{2000} [hh mm ss]	δ_{2000} [$^{\circ}$ ' '']	M_B [mag]	ΔM_B [mag]	M_R [mag]	ΔM_R [mag]	APM (BJ) [mag]
(1)	(2)	(3)	(4)	(5)	(6)	(7)	(8)
HCG 16-31563	2 10 22.75	-10 23 46.14	18.7832	0.0061	17.9534	0.0149	19.71
HCG 16-37906	2 10 4.77	-10 21 11.34	20.1435	0.0128	19.7528	0.0205	
HCG 16-72709	2 8 59.88	-10 9 42.16	20.0756	0.0121	19.4659	0.0142	
HCG 16-99096	2 10 13.13	-10 4 34.25	19.4816	0.0103	18.8106	0.0139	
HCG 16-94013	2 9 1.03	-10 5 18.1	20.1322	0.0106	19.2746	0.0266	
HCG 16-126732	2 10 18.49	-9 58 39.25	20.0906	0.0111	19.2656	0.0148	
HCG 16-83544	2 10 8.77	-10 7 2.78	20.7861	0.0152	20.0066	0.037	
HCG 16-91064	2 9 37.92	-10 5 33.47	21.0433	0.0331	20.6102	0.0308	
HCG 16-102419	2 8 58.49	-10 3 19.87	20.9508	0.0186	20.3169	0.0492	

Table B.2: High probability dwarf irregular member galaxies of HCG 16

no.	α_{2000} [hh mm ss]	δ_{2000} [$^{\circ}$ ' '']	M_B [mag]	ΔM_B [mag]	M_R [mag]	ΔM_R [mag]	APM (BJ) [mag]
(1)	(2)	(3)	(4)	(5)	(6)	(7)	(8)
HCG 19-39278	2 43 0.93	-12 33 50.69	20.0237	0.0236	18.5236	0.012	19.74
HCG 19-52784	2 43 1.98	-12 29 15.72	19.249	0.0175	17.7753	0.0057	19.31
HCG 19-77935	2 41 44.57	-12 23 23.35	18.7774	0.008	17.3346	0.0045	18.97
HCG 19-104186	2 43 33.90	-12 18 8.93	20.545	0.0178	19.5058	0.018	
HCG 19-21557	2 43 4.41	-12 38 49.06	20.378	0.0168	18.87	0.0087	19.99
HCG 19-34829	2 43 2.81	-12 35 5.17	20.7104	0.0253	19.7393	0.015	20.47
HCG 19-38519	2 43 36.48	-12 33 38.63	21.6365	0.068	20.6244	0.0548	
HCG 19-40837	2 43 14.20	-12 32 54.49	20.6047	0.0227	19.3524	0.0141	
HCG 19-44593	2 43 29.02	-12 31 38.82	20.7779	0.0234	19.3014	0.0111	
HCG 19-52425	2 43 18.06	-12 29 7.51	20.8037	0.0421	19.8149	0.0299	
HCG 19-84590	2 41 45.69	-12 21 40.21	19.8383	0.0116	18.7086	0.0123	20.07
HCG 19-85950	2 43 13.97	-12 21 39.56	18.7577	0.008	17.6733	0.0064	18.94
HCG 19-89770	2 42 38.51	-12 20 24.43	21.219	0.0326	20.0981	0.0195	
HCG 19-100720	2 41 44.63	-12 18 57.1	20.3318	0.0166	19.0673	0.0098	
HCG 19-125789	2 43 44.32	-12 15 7.52	20.5377	0.0183	19.1152	0.0116	
HCG 19-127980	2 41 59.51	-12 14 46.79	20.6664	0.0205	19.3617	0.0191	
HCG 19-130462	2 42 35.72	-12 14 26.45	20.2129	0.017	18.9467	0.0166	
HCG 19-140509	2 42 18.99	-12 13 16.03	20.5175	0.0192	19.0261	0.0167	
HCG 19-148093	2 43 16.96	-12 12 25.81	20.3266	0.0141	18.9784	0.011	
HCG 19-172886	2 43 8.19	-12 10 26.83	20.5147	0.0218	19.3345	0.0115	

Table B.3: High probability dwarf elliptical member galaxies of HCG 19

no.	α_{2000} [hh mm ss]	δ_{2000} [$^{\circ}$ ' '']	M_B [mag]	ΔM_B [mag]	M_R [mag]	ΔM_R [mag]	APM (BJ) [mag]
(1)	(2)	(3)	(4)	(5)	(6)	(7)	(8)
HCG 19-53888	2 43 40.19	-12 28 45.19	21.2196	0.0319	20.4728	0.0447	
HCG 19-88209	2 42 43.34	-12 20 52.26	20.7833	0.0245	20.1505	0.0387	
HCG 19-89349	2 42 6.45	-12 21 17.6	19.2922	0.0114	18.8072	0.0124	18.10
HCG 19-115081	2 43 0.04	-12 16 27.98	20.9601	0.0253	20.1057	0.0385	

Table B.4: High probability dwarf irregular galaxies of HCG 19

SELECTED DWARF GALAXIES

no.	α_{2000}	δ_{2000}	M_B	ΔM_B	M_R	ΔM_R	APM (BJ)
(1)	[hh mm ss]	[$^{\circ}$ ' "]	[mag]	[mag]	[mag]	[mag]	[mag]
HCG 30-102844	4 35 46.15	-2 44 42.24	21.6933	0.0368	20.6102	0.0311	
HCG 30-103324	4 35 58.34	-2 45 0.72	17.784	0.0038	16.5277	0.0027	
HCG 30-111915	4 36 0.85	-2 43 18.95	20.9964	0.0232	19.6814	0.0227	
HCG 30-113098	4 36 55.49	-2 43 25.6	19.6013	0.0104	18.5778	0.0074	
HCG 30-117419	4 36 5.04	-2 42 51.92	19.6668	0.0171	18.3437	0.0098	
HCG 30-119018	4 37 4.41	-2 42 21.55	21.3825	0.0327	20.2745	0.0255	
HCG 30-127051	4 36 4.53	-2 41 40.07	19.4573	0.0104	18.4418	0.0142	
HCG 30-129095	4 35 45.08	-2 41 7.84	20.7175	0.0379	19.7778	0.0311	
HCG 30-141925	4 36 45.67	-2 39 29.31	21.3786	0.05	20.268	0.0385	
HCG 30-151006	4 36 26.94	-2 38 26.49	20.8501	0.0206	19.5546	0.0225	
HCG 30-162304	4 37 14.81	-2 37 13.45	20.5782	0.0142	19.3591	0.0117	
HCG 30-177373	4 35 47.14	-2 35 54.18	19.6884	0.0113	18.1756	0.0076	
HCG 30-181336	4 36 32.54	-2 35 40.61	19.3307	0.0086	18.1039	0.0058	
HCG 30-187371	4 36 8.69	-2 35 5.54	20.3456	0.0156	19.1511	0.0121	
HCG 30-194269	4 35 38.97	-2 34 38.65	20.376	0.0125	18.8613	0.0082	
HCG 30-199292	4 37 3.54	-2 34 22.5	19.6826	0.0081	18.6824	0.0085	
HCG 30-21638	4 36 52.38	-3 3 45.42	20.411	0.0161	19.3472	0.012	
HCG 30-27976	4 36 29.12	-3 2 32.01	20.5424	0.0199	19.4275	0.0163	
HCG 30-35025	4 37 12.10	-3 0 36.93	20.4571	0.0192	19.5115	0.016	
HCG 30-37487	4 37 28.51	-2 59 55.1	20.8862	0.02	19.4545	0.0121	
HCG 30-38578	4 36 37.69	-3 0 11.34	20.3878	0.0382	19.1143	0.0242	
HCG 30-39892	4 36 49.60	-2 59 24.07	21.7105	0.0395	20.5659	0.0538	
HCG 30-41558	4 36 48.79	-2 58 51.52	20.4199	0.0145	19.4853	0.0123	
HCG 30-42216	4 37 17.07	-2 58 52.42	21.0288	0.0376	19.5444	0.0219	
HCG 30-42330	4 37 23.34	-2 58 35.89	20.3996	0.0151	19.1605	0.0159	
HCG 30-43255	4 36 19.88	-2 58 15.63	21.2919	0.041	20.0081	0.0183	
HCG 30-45108	4 36 14.23	-2 58 13.33	21.0161	0.0281	19.859	0.039	
HCG 30-50394	4 36 25.64	-2 56 13.58	21.6056	0.0333	20.2134	0.0226	
HCG 30-52519	4 36 31.32	-2 55 38.22	20.2934	0.0238	19.1359	0.0188	
HCG 30-57160	4 36 7.25	-2 54 14.89	21.6336	0.054	20.2286	0.0365	
HCG 30-59095	4 37 14.00	-2 53 39.98	21.2335	0.0501	20.1355	0.0427	
HCG 30-61976	4 36 32.22	-2 52 55.58	21.0902	0.0276	19.7943	0.0321	
HCG 30-62791	4 35 56.79	-2 52 59.43	21.7073	0.0351	20.5677	0.0522	
HCG 30-63366	4 36 0.34	-2 52 59.61	19.9564	0.0237	18.7329	0.0194	
HCG 30-68005	4 36 53.10	-2 51 20.43	20.8276	0.0213	19.6637	0.0268	
HCG 30-68618	4 36 38.69	-2 51 12.13	20.9971	0.0251	19.69	0.0272	
HCG 30-70667	4 36 40.95	-2 50 45.87	21.4432	0.0348	20.1111	0.0369	
HCG 30-71447	4 36 32.39	-2 50 32.52	20.1002	0.0132	18.9486	0.0106	
HCG 30-75546	4 35 42.62	-2 49 37.84	20.2486	0.0207	19.151	0.01	
HCG 30-76164	4 36 42.15	-2 49 36.1	20.4803	0.0264	19.3453	0.02	
HCG 30-87323	4 36 13.60	-2 47 23.18	21.6956	0.0539	20.4926	0.0409	
HCG 30-87644	4 36 26.69	-2 47 20.8	20.676	0.0347	19.5531	0.0192	
HCG 30-93649	4 37 0.03	-2 46 33.89	19.3727	0.01	18.1381	0.008	
HCG 30-99604	4 36 2.85	-2 45 9.1	21.9447	0.0447	20.6646	0.0478	

Table B.5: High probability dwarf elliptical member galaxies of HCG 30

SELECTED DWARF GALAXIES

no.	α_{2000} [hh mm ss]	δ_{2000} [$^{\circ}$ ' '']	M_B [mag]	ΔM_B [mag]	M_R [mag]	ΔM_R [mag]	APM (BJ) [mag]
(1)	(2)	(3)	(4)	(5)	(6)	(7)	(8)
HCG 30-102127	4 35 37.39	-2 45 18.53	19.3311	0.0102	18.5593	0.0097	
HCG 30-109529	4 35 34.66	-2 43 45.51	21.1849	0.0249	20.3762	0.0387	
HCG 30-136236	4 35 57.68	-2 40 1.57	20.626	0.0184	19.8025	0.0184	
HCG 30-22088	4 36 41.17	-3 3 36.04	21.4353	0.0342	20.7357	0.058	
HCG 30-51684	4 36 25.02	-2 56 28.81	19.409	0.0111	18.6597	0.0099	
HCG 30-54956	4 36 6.00	-2 54 56.71	20.1818	0.0195	19.3449	0.0199	

Table B.6: High probability dwarf irregular member galaxies of HCG 30

no.	α_{2000} [hh mm ss]	δ_{2000} [$^{\circ}$ ' '']	M_B [mag]	ΔM_B [mag]	M_R [mag]	ΔM_R [mag]	APM (BJ) [mag]
(1)	(2)	(3)	(4)	(5)	(6)	(7)	(8)
HCG 31-110215	5 2 16.29	-4 3 41.01	21.531	0.023	20.3187	0.0186	
HCG 31-110329	5 2 29.78	-4 4 2.1	20.2983	0.0101	18.9247	0.0083	
HCG 31-114143	5 1 39.37	-4 3 2.12	21.6495	0.0227	20.2937	0.0167	
HCG 31-125162	5 0 34.18	-4 1 2.31	19.8036	0.0053	18.6268	0.0052	
HCG 31-128782	5 1 15.71	-4 0 26.09	21.3341	0.0162	19.8864	0.0267	
HCG 31-13551	5 0 56.34	-4 30 24.09	20.4201	0.0119	19.2154	0.0096	
HCG 31-138449	5 1 4.57	-3 59 47.01	20.4847	0.0085	19.3866	0.0096	
HCG 31-139232	5 1 42.98	-3 59 50.88	20.5601	0.0084	19.0598	0.0123	
HCG 31-14209	5 1 15.45	-4 30 19.73	20.9816	0.0146	20.0899	0.0171	
HCG 31-19437	5 0 42.17	-4 28 34.71	21.7273	0.0211	20.3482	0.0215	
HCG 31-25548	5 0 39.93	-4 27 26	20.9751	0.0141	19.7848	0.0159	
HCG 31-26591	5 0 31.42	-4 26 56.05	19.3428	0.005	18.3607	0.0064	
HCG 31-29478	5 1 12.14	-4 26 3.61	18.8317	0.0039	17.4618	0.0031	
HCG 31-37727	5 2 31.22	-4 23 34.71	21.467	0.0301	20.2504	0.0288	
HCG 31-40983	5 2 27.06	-4 22 35.91	20.4725	0.0121	19.3568	0.0125	
HCG 31-42431	5 2 11.44	-4 22 17.26	20.5605	0.0102	19.5984	0.0175	
HCG 31-43685	5 2 29.82	-4 21 40.06	20.5817	0.0157	19.3204	0.0157	
HCG 31-44430	5 0 30.55	-4 21 24.48	21.1102	0.0149	19.6573	0.0129	
HCG 31-45741	5 0 45.18	-4 20 51.62	21.7854	0.0231	20.4364	0.0375	
HCG 31-53307	5 0 29.18	-4 18 43.6	21.3223	0.0161	20.1189	0.0171	
HCG 31-53678	5 0 28.88	-4 18 25.97	21.0974	0.0134	19.9345	0.015	
HCG 31-54698	5 1 4.55	-4 18 41.32	20.1928	0.0078	18.9641	0.0063	
HCG 31-63696	5 2 35.49	-4 15 41.9	20.9551	0.0157	19.705	0.0145	
HCG 31-66862	5 2 2.77	-4 15 8.99	21.7241	0.0189	20.2989	0.0157	
HCG 31-67857	5 2 15.45	-4 14 56.68	22.0742	0.0531	20.7286	0.0465	
HCG 31-67955	5 2 24.96	-4 14 59.08	20.6621	0.0109	19.2121	0.011	
HCG 31-73171	5 1 0.36	-4 13 35.25	20.9535	0.0111	19.6642	0.0109	
HCG 31-75216	5 1 19.10	-4 12 47.05	21.9502	0.0311	20.7777	0.057	
HCG 31-7744	5 2 33.13	-4 31 10.51	21.621	0.0366	20.5268	0.0402	
HCG 31-81249	5 2 22.18	-4 10 57.82	21.8336	0.0217	20.47	0.0345	
HCG 31-83348	5 1 2.47	-4 10 40.9	20.5629	0.0099	19.6047	0.0114	
HCG 31-84649	5 2 12.84	-4 9 57.33	21.9164	0.0263	20.9879	0.0273	
HCG 31-86449	5 1 53.41	-4 9 56.68	21.9005	0.0251	20.5771	0.0232	
HCG 31-92808	5 2 33.54	-4 8 4.24	19.7687	0.0056	18.5981	0.0058	

Table B.7: High probability dwarf elliptical member galaxies of HCG 31

SELECTED DWARF GALAXIES

no.	α_{2000}	δ_{2000}	M_B	ΔM_B	M_R	ΔM_R	APM (BJ)
(1)	[hh mm ss]	[$^{\circ}$ ' '']	[mag]	[mag]	[mag]	[mag]	[mag]
HCG 31-12218	5 1 40.17	-4 30 34.01	21.4669	0.0192	20.8742	0.0559	
HCG 31-125639	5 1 51.36	-4 0 49.62	20.8351	0.0121	20.4314	0.0351	
HCG 31-50389	5 0 30.01	-4 20 17.46	18.1938	0.0029	17.3678	0.0042	
HCG 31-58819	5 0 30.36	-4 17 19.41	19.4105	0.0051	18.5041	0.0068	
HCG 31-62800	5 2 34.21	-4 15 53.62	20.4384	0.0102	19.8387	0.0289	
HCG 31-71718	5 1 26.48	-4 13 52.6	21.2965	0.0199	20.7637	0.027	
HCG 31-72659	5 2 15.94	-4 13 46.59	20.855	0.0158	20.3709	0.0204	
HCG 31-83587	5 1 37.83	-4 10 23.7	21.2152	0.0283	20.478	0.0391	
HCG 31-9242	5 1 51.60	-4 30 54.58	21.0985	0.014	20.3235	0.0187	
HCG 31-92606	5 0 57.90	-4 7 52.85	21.8347	0.0288	21.0096	0.0621	
HCG 31-98094	5 2 27.48	-4 6 37.31	21.2938	0.0145	20.4619	0.0198	

Table B.8: High probability dwarf irregular galaxies of HCG 31

no.	α_{2000}	δ_{2000}	M_B	ΔM_B	M_R	ΔM_R	APM (BJ)
(1)	[hh mm ss]	[$^{\circ}$ ' '']	[mag]	[mag]	[mag]	[mag]	[mag]
HCG 42-131910	9 59 33.84	-19 27 14.08	21.2138	0.0278	19.9613	0.0132	
HCG 42-143920	9 59 59.95	-19 25 35.98	21.8035	0.037	20.5225	0.0265	
HCG 42-152538	10 0 58.63	-19 25 11.57	18.4267	0.0041	17.1621	0.0026	
HCG 42-156447	9 59 26.11	-19 24 21.28	20.8296	0.0213	19.7282	0.0095	
HCG 42-30991	9 59 20.11	-19 50 12.23	20.5172	0.0161	19.6138	0.0101	
HCG 42-42518	10 1 14.69	-19 47 20.51	20.7258	0.0202	19.6086	0.0097	
HCG 42-42580	9 59 45.48	-19 47 7.44	21.5144	0.0529	20.5155	0.0291	
HCG 42-44802	10 0 37.37	-19 46 32.92	21.5994	0.04	20.712	0.0375	
HCG 42-45048	10 1 5.04	-19 46 40.84	20.2544	0.028	19.2283	0.0086	
HCG 42-51261	10 1 15.41	-19 44 39.88	21.7801	0.0385	20.4814	0.0266	
HCG 42-55943	10 0 29.52	-19 43 25.03	21.6098	0.0371	20.5693	0.0307	
HCG 42-55946	10 0 39.60	-19 44 10.72	19.5211	0.0094	18.443	0.0072	
HCG 42-62888	10 1 5.57	-19 41 25.01	20.4091	0.0143	19.3433	0.0073	
HCG 42-64257	10 0 47.76	-19 41 3.98	20.2274	0.0162	18.7466	0.0089	
HCG 42-65670	10 0 21.22	-19 40 34.03	20.5521	0.0167	19.0919	0.0061	
HCG 42-67004	10 0 45.48	-19 40 40.62	19.2649	0.0107	18.1731	0.0093	
HCG 42-67934	10 0 42.07	-19 39 47.7	21.665	0.0379	20.2808	0.0133	
HCG 42-68537	10 0 36.10	-19 39 37.15	21.7072	0.036	20.3256	0.0265	
HCG 42-70009	9 59 29.18	-19 39 10.37	21.6244	0.0357	20.3232	0.0295	
HCG 42-71184	10 0 22.66	-19 38 57.23	21.7669	0.0398	20.5099	0.0166	
HCG 42-74918	9 59 44.59	-19 37 39.54	21.2735	0.0516	20.0451	0.0227	
HCG 42-79143	10 0 40.49	-19 36 34.92	21.1208	0.0429	19.6358	0.014	
HCG 42-81248	10 0 13.78	-19 36 42.8	18.3731	0.0063	17.1652	0.0029	
HCG 42-87395	10 0 52.70	-19 34 50.48	21.6895	0.0416	20.313	0.0153	
HCG 42-94407	9 59 37.68	-19 33 33.59	19.3583	0.0097	18.3738	0.0057	

Table B.9: High probability dwarf elliptical member galaxies of HCG 42

no.	α_{2000}	δ_{2000}	M_B	ΔM_B	M_R	ΔM_R	APM (BJ)
(1)	[hh mm ss]	[$^{\circ}$ ' '']	[mag]	[mag]	[mag]	[mag]	[mag]
HCG 42-101364	10 0 52.68	-19 32 17.3	21.1591	0.0281	20.5072	0.0309	
HCG 42-162028	10 0 3.24	-19 24 15.91	19.1383	0.0075	18.5499	0.0065	
HCG 42-169805	10 0 16.85	-19 24 24.8	21.0638	0.0258	20.6826	0.0175	
HCG 42-72228	9 59 11.40	-19 38 51.72	19.8631	0.0115	19.2789	0.0154	

Table B.10: High probability dwarf irregular galaxies of HCG 42

Appendix C

Velocities of HCG member galaxies

Tables C.1 to C.5 list all galaxies, which were used to calculate the dynamical mass and the radius R_0 of the sample HCGs. All galaxies lie inside a radius of 2 Mpc around the group center and their velocities lie in a 1000 km/s velocity interval corresponding to the mean velocity of the original HCG galaxies, which define the HCG center (Table 2.1).

Column (1) contains the galaxy names, which were extracted from NED. Their coordinates are listed in columns (2) and (3) and the galaxies' radial velocities are listed in column (4).

gal. name	α_{2000} [hh mm ss]	δ_{2000} [° ' '']	v [km/s]
(1)	(2)	(3)	(4)
ARP318	2 9 31.30	-10 9 31	3957
NGC0838	2 9 38.50	-10 8 49	3859
NGC0835	2 9 24.70	-10 8 11	4073
PCM200021	2 9 22.60	-10 8 3	4143
NGC0833	2 9 20.90	-10 7 60	3864
RASSCALSSS2b075	2 9 40.80	-10 11 2	3699
NGC0839	2 9 42.90	-10 11 3	3934
KUG0206-105	2 9 6.00	-10 19 13	3972
NGC0848	2 10 17.60	-10 19 17	3989
HCG016-dRC97-15	2 8 57.90	-10 23 19	3163
RdC96-10	2 8 36.80	-9 56 17	4000
KUG0206-099A	2 9 5.10	-9 42 3	3828
NGC0806	2 3 31.10	-9 55 60	3944
KUG0200-101	2 3 16.60	-9 53 27	3887
UGCA023	2 3 2.20	-9 39 17	3864
MCG-02-06-017	2 1 51.20	-10 28 1	4719
NGC0873	2 16 32.40	-11 20 56	4036

Table C.1: Galaxies used for the determination of R_0 of HCG 16

VELOCITIES OF HCG MEMBER GALAXIES

galaxy	α_{2000} [hh mm ss]	δ_{2000} [$^{\circ}$ ' '']	v [km/s]
(1)	(2)	(3)	(4)
MCG-02-07-075	2 42 46.80	-12 23 51	4253
MCG-02-07-074	2 42 42.10	-12 25 40	4210
MCG-02-07-073	2 42 38.40	-12 25 17	4254
APMUKS(BJ)B024009.04-123637.5	2 42 33.20	-12 23 53	3849
NPM1G-12.0100	2 42 18.80	-12 14 33	4152
HCG019:[dRC97]24	2 43 10.00	-12 11 39	4027
MCG-02-07-069	2 41 38.90	-12 21 34	4244
MCG-02-08-004	2 45 7.90	-13 14 12	4312
NGC1045	2 40 29.10	-11 16 39	4619
MCG-02-07-038	2 35 35.80	-12 16 34	4838
NGC1118	2 49 58.70	-12 9 49	4161
NGC1006	2 37 34.70	-11 1 34	4715
NGC1011	2 37 38.90	-11 0 20	4922

Table C.2: Galaxies used for the determination of R_0 of HCG 19

galaxy	α_{2000} [hh mm ss]	δ_{2000} [$^{\circ}$ ' '']	v [km/s]
(1)	(2)	(3)	(4)
HCG030	4 36 28.60	-2 49 57	4617
CGCG393-045	4 36 30.20	-2 51 59	4625
HCG030D	4 36 36.60	-2 50 35	4666
HCG030C	4 36 23.30	-2 47 59	4508
CGCG393-044	4 36 18.50	-2 49 53	4697
MCG-01-12-037	4 36 50.20	-3 2 39	4797
NGC1618	4 36 6.60	-3 8 56	4893
*NGC1622	4 36 36.60	-3 11 20	4852
FGC0495	4 37 31.30	-3 6 15	4424
*NGC1625	4 37 6.20	-3 18 13	4759
MCG-01-12-028	4 33 1.00	-4 11 19	4905
MCG-01-12-015	4 31 23.80	-3 55 32	4752

Table C.3: Galaxies used for the determination of R_0 of HCG 30

VELOCITIES OF HCG MEMBER GALAXIES

galaxy	α_{2000} [hh mm ss]	δ_{2000} [$^{\circ}$ ' '']	v [km/s]
(1)	(2)	(3)	(4)
NGC1741NED03	5 1 37.80	-4 15 28	4019
NGC1741NED04	5 1 38.70	-4 15 33	4074
NGC1741NED01	5 1 35.30	-4 15 51	4136
IC0399	5 1 44.10	-4 17 19	3991
NGC1729	5 0 15.70	-3 21 7	3632
NGC1700	4 56 56.30	-4 51 55	3895
*MCG+00-13-066	5 3 17.40	-2 56 9	4329
MCG-01-13-035	4 55 3.20	-4 6 7	3914
FGC0519	5 2 47.30	-2 17 4	4456
2MASXJ0453180-042220	4 53 18.00	-4 22 21	3568
2MASXJ0453162-042141	4 53 16.20	-4 21 42	3854

Table C.4: Galaxies used for the determination of R_0 of HCG 31

VELOCITIES OF HCG MEMBER GALAXIES

galaxy	α_{2000} [hh mm ss]	δ_{2000} [$^{\circ}$ ' "]	v [km/s]
(1)	(2)	(3)	(4)
NGC3091	10 0 14.30	-19 38 13	3964
2MASXiJ1000282-194016	10 0 28.20	-19 40 16	3828
HCG042[ZM98]	10 0 13.10	-19 38 24	3828
HCG042D	10 0 13.00	-19 40 23	4074
NGC3096	10 0 33.20	-19 39 45	4228
MCG-03-26-006	10 0 10.50	-19 37 21	4005
2MASXiJ1000251-193459	10 0 25.10	-19 34 60	3675
HCG042[d RC97]31	10 0 15.20	-19 34 57	4959
HCG042[dRC97]22	10 0 4.80	-19 36 58	3892
HCG042[ZM98]0059	10 0 37.70	-19 32 54	3647
2MASXiJ1000382-194540	10 0 38.10	-19 45 40	3766
HCG042[dRC97]16	10 0 44.40	-19 45 18	3376
HCG042[dRC97]41	10 0 3.30	-19 47 10	3379
HCG042[dRC97]12	9 59 37.00	-19 40 45	3891
HCG042[dRC97]11	10 1 0.50	-19 45 15	3848
HCG042[ZM98]0085	9 59 26.50	-19 38 57	3402
NGC3085	9 59 29.10	-19 29 32	3980
ESO567-G005	10 1 31.20	-19 32 22	3538
2MASXiJ0959187-192823	9 59 18.70	-19 28 23	3621
2MASXiJ0959139-195108	9 59 13.90	-19 51 8	3636
HCG042[ZM2000]0021	9 58 53.10	-19 42 19	3675
NGC3091GROUP	9 59 41.40	-19 17 3	3837
ESO567-G007	10 1 48.50	-19 56 30	4287
HCG042[ZM2000]0154	10 1 49.90	-19 56 32	4212
2MASXiJ1000315-191131	10 0 31.50	-19 11 31	3424
HCG042[ZM2000]0143	9 58 23.10	-19 42 19	4081
2MASXiJ1001314-200235	10 1 31.50	-20 2 35	3613
HCG042[ZM98]0065	10 1 55.80	-20 8 5	3938
ESO566-G035	9 57 38.80	-19 30 14	3661
HCG042[ZM2000]0058	9 58 54.40	-20 12 34	3853
CSRG0577	9 57 51.80	-19 20 19	3442
NPM1G-18.0322	9 58 6.40	-19 13 50	3977
ESO566-G043	10 0 43.40	-20 22 5	3879
HCG042[ZM98]0057	10 2 54.70	-20 4 52	3846
NGC3072	9 57 23.90	-19 21 16	3616
ESO567-G006	10 1 32.40	-20 22 58	3727
HCG042[ZM98]0033	10 2 4.80	-18 57 22	3908
HCG042[ZM2000]0166	9 57 53.70	-19 3 45	4049
HCG042[ZM98]0041	9 57 16.10	-19 7 56	4020
NGC3124[ZSF97]a	10 4 31.10	-19 27 39	3763
NGC3124	10 6 39.60	-19 13 22	3562
ESO566-G024	9 53 33.40	-19 34 59	3501
NPM1G-18.0330	10 7 11.00	-19 4 5	3476
NGC3052	9 54 27.90	-18 38 20	3778
ESO567-G013	10 5 48.20	-18 14 50	4941
UGCA195	10 3 18.90	-21 25 51	3069
ESO567-G015	10 6 25.20	-18 16 33	4876

Table C.5: Galaxies used for the determination of R_0 of HCG 42

List of Figures

1.1	HCG 79 and 87 observed with the Hubble Space Telescope (HST)	3
1.2	Two dwarf galaxies of the Local Group (NGC 6822 and M32)	10
2.1	Design of the detector head of the WFI	18
2.2	Transmission curves of the WFI broad band filter set	18
2.3	Transmission data for the broad band filter B/99	19
2.4	Transmission data for the broad band filter R/162	20
2.5	Flatfield corrected image of HCG 31	24
2.6	Result of the flatfield corrected mosaic image	26
2.7	Difference between the flat field corrected image and the fitted sky	27
2.8	Super Flat in the B -band created out of all object images	28
2.9	Flatfield corrected object image corrected with Super Flat	29
2.10	Final mosaic image of HCG 16 in the B band	32
2.11	Final mosaic image of HCG 19 in the R band	33
2.12	Final mosaic image of HCG 30 in the B band	33
2.13	Final mosaic image of HCG 31 in the B band	34
2.14	Final mosaic image of HCG 42 in the R band	35
2.15	Comparison between literature and mosaic data	38
3.1	CMD for the Coma Cluster	46
3.2	CMD of galaxies in HCG 16	50
3.3	CMD of galaxies in HCG 19	50
3.4	CMD of galaxies in HCG 30	51
3.5	CMD of galaxies in HCG 31	51
3.6	CMD of galaxies in HCG 42	52
3.7	Distribution of galaxies within HCG 16	56
3.8	Distribution of galaxies within HCG 19	56
3.9	Distribution of galaxies within HCG 30	57
3.10	Distribution of galaxies within HCG 31	57
3.11	Distribution of galaxies within HCG 42	58
3.12	Density Distribution of galaxies in HCG 16, 42 and 62	60
3.13	Density Distribution in HCG 16	61
3.14	Density Distribution in HCG 19	62

3.15	Density Distribution in HCG 30	63
3.16	Density Distribution in HCG 31	64
3.17	Density Distribution in HCG 42	65
3.18	The luminosity function of the HCG sample	67
3.19	Distribution of galaxy velocities with respect to the median group velocity	72
4.1	CMD of all HCG galaxies	75
4.2	Number of detected objects per mag interval in HCGs and the Leo I group	78
4.3	Density distribution of all member galaxies in the sample HCGs	82
A.1	Background elliptical galaxies	ii
A.2	Spiral galaxies seen edge-on	iii
A.3	Spiral galaxies seen face on	iv
A.4	Typical examples of high probability member galaxies of HCG 16	v
A.5	Figure A.4 continued	vi

List of Tables

1.1	Compact galaxy group catalogs	5
2.1	Sample of HCGs observed in this project	16
2.2	Observing log for the WFI observations	17
2.3	Read Out Noise and Gain values of each CCD Chip	22
2.4	Solution of the transformation equations	36
2.5	Magzero _{B,R} and magzero _{totalB,R} for each mosaic image	37
2.6	Radius of the smallest Local Group galaxy at the distance of the HCGs . .	41
2.7	Number of identified objects in the mosaic images	42
3.1	Dynamical mass and radius of the sample HCGs	70
4.1	Dynamical mass (M_{dyn}) and radius of the zero-velocity surface (R_0)	84
B.1	dE galaxies in the red sequence of HCG 16	viii
B.2	dIrr on the left side of the red sequence of HCG 16	ix
B.3	dE galaxies in the red sequence of HCG 19	ix
B.4	dIrr on the left side of the red sequence of HCG 19	ix
B.5	dE galaxies in the red sequence of HCG 30	x
B.6	dIrr on the left side of the red sequence of HCG 30	xi
B.7	dE galaxies in the red sequence of HCG 31	xi
B.8	dIrr on the left side of the red sequence of HCG 31	xii
B.9	dE galaxies in the red sequence of HCG 42	xii
B.10	dIrr on the left side of the red sequence of HCG 42	xii
C.1	Galaxies used for the determination of R_0 of HCG 16	xiii
C.2	Galaxies used for the determination of R_0 of HCG 19	xiv
C.3	Galaxies used for the determination of R_0 of HCG 30	xiv
C.4	Galaxies used for the determination of R_0 of HCG 31	xv
C.5	Galaxies used for the determination of R_0 of HCG 42	xvi

Bibliography

- Abraham, R. G., Valdes, F., Yee, H. K. C., & van den Bergh, S., 1994, *The morphologies of distant galaxies. 1: an automated classification system*, ApJ, 432, 75–90
- Aceves, H. & Perea, J., 1999a, *Estimating Masses in Clusters of Galaxies*, ASP, 176, 198–205
- Aceves, H. & Perea, J., 1999b, *On two mass estimators for clusters of galaxies*, A&A, 345, 439–447
- Allen, R.J. & Shu, F.H., 1979, *The extrapolated central surface brightness of galaxies*, ApJ, 227:67–72
- Arp, H., 1966, *Atlas of Peculiar Galaxies*, ApJ Suppl., 14, 1–20
- Athanassoula, E., Makino, J., & Bosma, A., 1997, *Evolution of compact groups of galaxies - I. Merging rates*, MNRAS, 286, 825
- Baade D., 2002, *La Silla Instrumentation Wide Field Imager (WFI) user manual*, Doc. No. LSO–MAN–ESO–22100–00001, Issue 1.0.7
- Baade D., 1999, *La Silla Instrumentation Wide Field Imager (WFI) user manual*, Doc. No. LSO–MAN–ESO–22100–00001, Issue 1.0.4
- Bahcall, N. A., Harris, D. E., & Rood, H. J., 1984, *X-ray emission from Stephan's Quintet and other compact groups*, ApJ, 284, L29–L33
- Barnes, J., 1989, *Evolution of compact groups and the formation of elliptical galaxies*, Nature, 338, 123
- Barnes, J., 1985, *The dynamical state of groups of galaxies*, MNRAS, 215, 517–536
- Barton, E., Geller, M., Ramella, M., Marzke, R. O., & da Costa, L. N., 1996, *Compact Group selection From Redshift Surveys*, AJ, 112, 871–886
- Benson, A. J., Bower, R. G., Frenk, C. S., Lacey, C. G., Baugh, C. M., & Cole, S., 2003, *What Shapes the Luminosity Function of Galaxies?*, ApJ, 599, 38–49

- Bertin E., 2001, *SExtractor v2.1.3 User's guide*, Institut d'Astrophysique & Observatoire de Paris, http://www.eso.org/science/eis/eis_doc/doc_index.html
- Bertin E., Arnouts S., 1996, *SExtractor: Software for source extraction*, A&AS, 117, 393
- Binggeli, B., Popescu, C. C., & Tammann, G. A., 1993, *The kinematics of the Virgo cluster revisited*, A&AS, 98, 275–196
- Binggeli, B., Tarenghi, M. & Sandage, A., 1990, *The abundance and morphological segregation of dwarf galaxies in the field*, A&A 228, 42–60
- Binggeli, B., Tammann, G.A. & Sandage, A., 1987, *Studies of the Virgo cluster. VI - Morphological and kinematical structure of the Virgo cluster*, AJ, 94, 251–277
- Blanton, M. R. , Dalcanton, J., Eisenstein, D., et al. 2001, *The Luminosity Function of Galaxies in SDSS Commissioning Data*, AJ, 121, 2358–2380
- Bode, P. W., Cohn, H. N., & Lugger, P. M., 1993, *Simulations of Compact Groups of Galaxies: The Effect of the Dark Matter Distribution*, ApJ 416, 17–25
- Böhringer, H., Briel, U. G., Schwarz, R. A., Voges, W., Hartner, G., & Trumper, J., 1994, *The Structure of the Virgo Cluster of Galaxies from ROSAT X-Ray Images*, Nature 368, 828
- Bower, R. G., Lucey, J. R., & Ellis, R. S., 1992, *Precision Photometry of Early Type Galaxies in the Coma and Virgo Clusters - a Test of the Universality of the Colour / Magnitude Relation - Part Two - Analysis*, MNRAS, 254, 601
- Briel, U. G., Henry, J. P., & Böhringer, H. 1992, *Observation of the Coma cluster of galaxies with ROSAT during the all-sky survey*, A&A, 259, L31–L34
- Busko, I. C., 1996, *Error Estimation in Elliptical Isophote Fitting*, ASP 101, p. 139–142
- Campos-Aguilar, A. & Moles, M., 1991, *Environmental properties of violently star-forming galaxies*, A&A, 241, 358–364
- Carlberg, R. G., Yee, H. K. C., Ellingson, E., Abraham, R., Gravel, P., Morris, S., & Pritchet, C. J., 1996, *Galaxy Cluster Virial Masses and Omega*, ApJ, 462, 32
- Cavaliere, A., Colafrancesco, S., & Scaramella, R., 1991, *The mass distribution of groups and clusters of galaxies*, ApJ, 380, 15–23
- Cellone, S. A., Forte, J. C., & Geisler, D., 1994, *A morphological and color study of Fornax low surface brightness galaxies in the Washington system*, ApJ, 93, 397–424
- Conselice, C. J., 1997, *The Symmetry, Color, and Morphology of Galaxies*, PASP, 109, 1251–1255

- Conselice, C. J., Gallagher, J. S., & Wyse, R. F. G., 2003, *Galaxy Populations and Evolution in Clusters. III. The Origin of Low-Mass Galaxies in Clusters: Constraints from Stellar Populations*, AJ, 125, 66–85
- Conselice, C. J., Gallagher, J. S., & Wyse, R. F. G., 2002, *Galaxy Populations and Evolution in Clusters. II. Defining Cluster Populations*, AJ, 123, 2246–2260
- Conselice, C. J., Gallagher, J. S., & Wyse, R. F. G., 2001, *Galaxy Populations and Evolution in Clusters. I. Dynamics and the Origin of Low-Mass Galaxies in the Virgo Cluster*, ApJ, 559, 791–811
- Cote, S., Freeman, K. C., Carignan, C., & Quinn, P. J., 1997, *Discovery of Numerous Dwarf Galaxies in the Two Nearest Groups of Galaxies*, AJ, 114, 1313
- Cousins, A. W. J., 1976, *Standard Stars for VRI Photometry with S25 Response Photocathodes* Mon. Not. of the Astron. Soc. of South Africa, 35, 70–
- Couture, J., Harris, W. E., & Allwright, J. W. B., 1991, *Multicolor CCD photometry of globular clusters in two Virgo elliptical galaxies*, ApJ, 372, 97–110
- Couture, J., Harris, W. E., & Allwright, J. W. B., 1990, *BVI photometry of globular clusters in M87*, ApJS, 73, 671–683
- Cox, A.N. ed., 2000, *Allens's Astrophysical Quantities*, Springer Verlag, ISBN 0–387–98746–0
- de Carvalho, R.R., Ribeiro, A.L.B., Capelato, H., Zepf, S.E., 1997, *Redshift Survey of Galaxies around a Selected Sample of Compact Groups*, ApJ 110, 1
- de Carvalho, R. R., Ribeiro, A. L. B., Zepf, S. E., 1994, *Structural properties of compact groups*, ApJS, 93, 47–63
- Diaferio, A., Geller, M. J., & Ramella, M., 1995, *The Formation of Compact Groups of Galaxies. II. X-Ray Properties*, AJ, 109, 2293–2304
- Diaferio, A., Geller, M. J., & Ramella, M., 1994, *The formation of compact groups of galaxies. I: Optical properties*, AJ, 107, 868–879
- Dressler, A., 1980, *Galaxy morphology in rich clusters - Implications for the formation and evolution of galaxies*, ApJ, 236, 351–365
- Dressler, A. & Shectman, S. A., 1988, *Evidence for substructure in rich clusters of galaxies from radial-velocity measurements*, AJ, 95, 985–995
- Drinkwater, M. J. , Phillipps, S., Jones, J. B., et al. 2000, *The Fornax spectroscopic survey. I. Survey strategy and preliminary results on the redshift distribution of a complete sample of stars and galaxies*, A&A, 355, 900

- Ebeling, H., Voges, W., & Boehringer, H., 1994, *X-ray emission from Hickson's compact groups of galaxies: Results from the ROSAT All-Sky Survey*, ApJ, 436, 44–55
- Falco, E. E., Kurtz, M. J., Geller, M. J., et al. 1999, *The Updated Zwicky Catalog (UZC)*, PASP, 111, 438–452
- Ferguson, H. C. & Binggeli, B., 1994, *Dwarf elliptical galaxies*, A&A Rev., 6, 67–122
- Ferguson, H.C. & Sandage A., 1991, *Population studies in groups and clusters of galaxies. IV - Comparison of the luminosity functions and morphological-type distributions in seven nearby groups*, AJ, 101, 765
- Flint, K., Metevier, A. J., Bolte, M., & Mendes de Oliveira, C., 2001, *The Z=0 Galaxy Luminosity Function. I. Techniques for Identification of Dwarf Galaxies at 10 MPC*, ApJ, 134, 53–75
- Focardi, P. & Kelm, B., 2002, *Compact groups in the UZC galaxy sample*, A&A, 391, 35–46
- Gallagher, J. S. & Wyse, R. F. G., 1994, *Dwarf spheroidal galaxies: Keystones of galaxy evolution*, PASP, 106, 1225–1238
- Garcia, A. M., 1995, *Compact groups of galaxies in the nearby universe*, A&A, 297, 56–60
- Geisler, D. & Forte, J. C., 1990, *The abundance distribution and luminosity function of globular clusters in NGC 1399* ApJ, 350, L5–L8
- Gottlöber, Kerscher, Klypin, Kravtsov, Faltenbacher, Müller, 2002, *Spatial distribution of galactic halos and their merger histories*, A&A 387, 778
- Governato, F., Bhatia, R., & Chincarini, G., 1991, *A long-lasting compact group*, ApJ, 371, L15–L18
- Grebel, E. K., Gallagher, J. S., & Harbeck, D., 2003, *The Progenitors of Dwarf Spheroidal Galaxies*, AJ, 125, 1926–1939
- Heiligman, G. M. & Turner, E. L., 1980, *The anomalous luminosity function of galaxies in compact groups*, ApJ, 236, 745–749
- Heisler, J., Tremaine, S., Bahcall, J.N., 1985, *Estimating the mass of galaxy groups: alternatives to the virial theorem*, AJ, 298:8–17
- Held, E. V. & Mould, J. R. 1994, *Spectroscopy of dwarf elliptical galaxies in the Fornax cluster*, AJ, 107, 1307–1319
- Helsdon, S. F. & Ponman, T. J., 2000, *Are X-ray properties of loose groups different from those of compact groups?*, MNRAS, 319, 933–938

- Hickson, P., 1994, *Atlas of Compact Groups of Galaxies*, Basel: Gordon & Breach, ISBN 2-88449-116-3
- Hickson, P., 1982, *Systematic properties of compact groups of galaxies*, ApJ 255, 382–391
- Hickson, P., Mendes de Oliveira, C., Huchra, J.P., Palumbo, G.G. C., 1992, *Dynamical properties of compact groups of galaxies*, ApJ, 399,353–367
- Hickson, P., Kindl, E., & Auman, J. R., 1989a, *A photometric catalog of compact groups of galaxies*, ApJ, 70, 687–698
- Hickson, P., Menon, T. K., Palumbo, G. G. C., & Persic, M., 1989b, *Infrared emission from compact groups of galaxies*, ApJ, 341, 679–684
- Hickson, P., Kindl, E. & Huchra, J.P. 1988a, *Morphology of galaxies in compact groups*, ApJ 331, 64–70
- Hickson P. & Rood, H. J.1988b, *The nature of compact groups of galaxies*, ApJ, 331, L69–L72
- Hopp, U., Wagner, S. J., & Richtler, T., 1995, *The globular cluster system of NGC 5813*, A&A, 296, 633–642
- Hunsberger, S. D., Charlton, J. C., & Zaritsky, D., 1996, *The Formation of Dwarf Galaxies in Tidal Debris: A Study of the Compact Group Environment*, ApJ, 462, 50–56
- Iovino A., 2002, *Detecting Fainter Compact Groups: Results from a New Automated Algorithm*, AJ 124, 2471–2489
- Iovino A., 2000, *A new compact group sample in the southern sky*, ASP, 209, 25–30
- Jedrzejewski, R. I., 1987, *CCD surface photometry of elliptical galaxies. I - Observations, reduction and results*, MNRAS, 226, 747–768
- Jerjen, H. & Binggeli, B., 1997, *Are "Dwarf" Ellipticals Genuine Ellipticals?*, ASP Conf. Ser. 116: The Nature of Elliptical Galaxies; 2nd Stromlo Symposium, 239
- Johnson, H. L. & Morgan, W. W., 1953, *Fundamental stellar photometry for standards of spectral type on the revised system of the Yerkes spectral atlas*, ApJ, 117, 313
- Kauffmann, G. & Charlot, S., 1998, *Chemical enrichment and the origin of the colour-magnitude relation of elliptical galaxies in a hierarchical merger model*, MNRAS, 294, 705
- Klypin, A., Kravtsov, A. V., Valenzuela, O., & Prada, F., 1999, *Where Are the Missing Galactic Satellites?*, ApJ, 522, 82–92
- Knebe & Müller, 2000, *Quantifying substructure in galaxy clusters*, A&A, 354, 761

- Knebe & Müller, 1999, *Formation of groups and clusters of galaxies*, A&A, 341 1
- Kodaira, K., Sekiguchi, M., Sugai, H., & Doi, M., 1991, *Redshift observation of Shakhbazyan's compact groups of galaxies and their number-diameter relation*, Publ. Astron. Soc. Jpn., 43, 169–176
- Kormendy, J. 1977, *rightness distributions in compact and normal galaxies. II - Structure parameters of the spheroidal component*, ApJ, 218, 333–346
- Kormendy, J. & Sanders, D. B., 1992, *Ultraluminous IRAS galaxies - Formation of elliptical galaxies by merger-induced dissipative collapse*, ApJ, 390, L53–L56
- Kron, R.G., 1980, *Photometry of a complete sample of faint galaxies*, ApJS 43, 305
- Landolt, A. U., 1992, *UBVRI Photometric standard stars in the magnitude range $11.5 \leq V \leq 16.0$ around the celestial equator*, AJ, 104, 1
- Larson, R. B., 1974, *Effects of supernovae on the early evolution of galaxies*, MNRAS, 169, 229–246
- Limber, D. N. & Mathews, W. G., 1960, *The Dynamical Stability of Stephan's Quintet*, ApJ, 132, 286–305
- Maccagni, D., Gioia, I. M., Henry, J. P., Maccacaro, T., Vettolani, G. P., & Wolter, A., 1990, *MS 0129.2 - 2237 - Interacting galaxies at $Z = 0.11$* , AJ, 100, 1461–1467
- Maddox, S. J., Efstathiou, G., Sutherland, W. J., & Loveday, J., 1990, *The APM galaxy survey. I - APM measurements and star-galaxy separation*, MNRAS, 243, 692–712
- Mamon, G. A., 1986, *Are compact groups of galaxies physically dense?*, ApJ, 307, 426–430
- Massey P., 1997, *A User's Guide to CCD Reduction with IRAF*, <http://iraf.noao.edu/>
- Massey P. & Davis L.E., 1992, *A User's Guide to Stellar CCD Photometry with IRAF*, <http://iraf.noao.edu/>
- Mateo, M. L., 1998, *Dwarf Galaxies of the Local Group*, ARA&A, 36, 435
- Mellier, Y., Mathez, G., Mazure, A., Chauvineau, B., & Proust, D., 1988, *Subclustering and evolution of the Coma cluster*, A&A, 199, 67–72
- Mendes de Oliveira, C. & Hickson, P., 1994, *Morphology of galaxies in compact groups*, ApJ, 427, 684–695
- Menon, T. K., 1995, *Radio properties of spiral galaxies in high-density groups*, MNRAS, 274, 845–852
- Menon, T. K., 1992, *Galaxy interactions and the origin of radio sources in high-density groups*, MNRAS, 255, 41–47

- Menon, T. K., 1991, *The influence of high-density environment on the radio-far-infrared correlation of spiral galaxies*, ApJ, 372, 419–423
- Moles, M., del Olmo, A., Perea, J., Masegosa, J., Marquez, I., & Costa, V., 1994, *Star formation and merging in compact groups of galaxies*, A&A, 285, 404–414
- Montoya, M. L., Dominguez-Tenreiro, R., Gonzalez-Casado, G., Mamon, G. A., & Salvador-Sole, E. 1996, *The Surface Density Profiles and Lensing Characteristics of Hickson Compact Groups of Galaxies*, ApJ, 473, L83
- Moore, B., Ghigna, S., Governato, F., Lake, G., Quinn, T., Stadel, J., & Tozzi, P., 1999, *Dark Matter Substructure within Galactic Halos*, ApJ, 524, L19–L22
- Moore, B., Frenk, C. S., & White, S. D. M., 1993, *Galaxy Groups - Abundance by Luminosity and by Velocity Dispersion*, MNRAS, 261, 827
- Mulchaey, J. S. 2000, *X-ray Properties of Groups of Galaxies*, ARA&A, 38, 289–335
- Mulchaey, J. S., Davis, D. S., Mushotzky, R. F., & Burstein, D., 2003, *An X-Ray Atlas of Groups of Galaxies*, ApJS, 145, 39–64
- Mulchaey, J. S. & Zabludoff, A. I. 1998, *The Properties of Poor Groups of Galaxies. II. X-Ray and Optical Comparisons*, ApJ, 496, 73
- Navarro, J. F., Mosconi, M. B., & Lambas, D. G., 1987, *Merging instability in groups of galaxies with dark matter*, MNRAS, 228, 501–511
- Ostriker, J. P. & Tremaine, S. D., 1975, *Another evolutionary correction to the luminosity of giant galaxies*, ApJ, 202, L113–L117
- Pahlen, E.V.D. & Gondolatsch, F., 1937, *Lehrbuch der Stellarstatistik*, Johann Ambrosius Barth, Leipzig
- Perea, J., del Olmo, A., & Moles, M., 1990, *Mass estimation for systems of galaxies*, A&A, 237, 319
- Pildis, R. A., 1995, *The Destruction of a Compact Group of Galaxies*, ApJ, 455, 492–496
- Pildis, R. A., Bregman, J. N., & Evrard, A. E., 1995, *ROSAT observations of compact groups of galaxies*, ApJ, 443, 514–526
- Plionis, M., Barrow, J. D., & Frenk, C. S., 1991, *Projected and intrinsic shapes of galaxy clusters*, MNRAS, 249, 662–677
- Ponman, T. J., Bourner, P. D. J., Ebeling, H., & Böhringer, H., 1996, *A ROSAT survey of Hickson's compact galaxy groups.*, MNRAS, 283, 690–708

- Ponman, T. J. & Bertram, D., 1993, *Hot gas and dark matter in a compact galaxy group*, Nature, 363, 51–54
- Prandoni, I., Iovino, A., MacGillivray, H. T., 1994, *Automated search for compact groups of galaxies in the southern sky*, AJ, 107, 1235–1244
- Press, W. H. & Schechter, P., 1974, *Formation of Galaxies and Clusters of Galaxies by Self-Similar Gravitational Condensation*, ApJ, 187, 425–438
- Puche, D. & Carignan, C., 1991, *H I studies of the Sculptor group galaxies. VII - Implications on the distribution and nature of dark matter in groups*, ApJ, 378, 487–495
- Ramella, M., Diaferio, A., Geller, M. J., & Huchra, J. P., 1994, *The birthplace of compact groups of galaxies*, AJ, 107, 1623–1628
- Rampazzo, R. & Sulentic, J. W., 1992, *Quantitative morphology of isolated E/S pairs of galaxies*, A&A, 259, 43–60
- Ribeiro, A. L. B., de Carvalho, R. R., & Zepf, S. E., 1994, *The luminosity function of galaxies in compact groups*, MNRAS, 267, L13–L16
- Rood, H. J. & Struble, M. F., 1994, *Spatial coincidence between a number of Hickson compact groups and loose groups or clusters*, PASP, 106, 413–416
- Rood, H. J. & Williams, B. A., 1989, *The neighborhood of a compact group of galaxies*, ApJ, 339, 772–782
- Rose, J. A., 1977, *A survey of compact groups of galaxies*, ApJ, 211, 311–318
- Rubin, V. C., Hunter, D. A., & Ford, W. K. J., 1991, *Optical properties and dynamics of galaxies in the Hickson compact groups*, ApJS, 76, 153–183
- Sakai, S., Giovanelli, R., & Wegner, G. 1994, *Distribution of galaxies around Abell 262 and the NGC 383 and NGC 507 groups*, AJ, 108, 33–43
- Sandage, A., 1986, *The redshift distance relation. IX. Perturbation of the very nearby velocity field by the mass of the local group*, ApJ, 307, 1–19
- Sandage, A., Binggeli, B., & Tammann, G. A., 1985, *Studies of the Virgo Cluster - Part Five - Luminosity Functions of Virgo Cluster Galaxies*, AJ, 90, 1759–1771
- Sandage, A. & Binggeli, B., 1984, *“Studies of the Virgo cluster. III - A classification system and an illustrated atlas of Virgo cluster dwarf galaxies”*, AJ, 89, 919–931
- Sanders, D. B. & Mirabel, I. F., 1996, *Luminous Infrared Galaxies*, Annu. Rev. A&A, 34, 749–792

- Saracco, P. & Ciliegi, P., 1995, *ROSAT observations of compact groups of galaxies*, A&A, 301, 348–358
- Schechter, P., 1976, *An analytic expression for the luminosity function for galaxies*, ApJ, 203, 297–306
- Schombert, J. M., Pildis, R. A., Eder, J., Oemler, A. J., 1995, *Dwarf Spirals*, AJ, 110, 2067–2074
- Schwartz, D. A., Schwarz, J., & Tucker, W. 1980, *X-ray emission from compact groups of galaxies*, ApJ, 238, L59–L62
- Secker, J. & Harris, W. E. 1997, *Dwarf Galaxies in the Coma Cluster. I. Detection, Measurement and Classification Techniques*, PASP, 109, 1364–1376
- Secker, J., Harris, W. E., Plummer, J. D., 1997, *Dwarf Galaxies in the Coma Cluster. II. Photometry and Analysis*, PASP, 109, 1377–1393
- Shakhbazian, R. K., 1973, *Compact groups of compact galaxies*, Astrofizika, 9, 495
- Smith, R. J., Lucey, J. R., Hudson, M. J., Schlegel, D. J., & Davies, R. L., 2000, *Streaming motions of galaxy clusters within 12000kms-1 - I. New spectroscopic data*, MNRAS, 313, 469–490
- Stetson, P. B., 1987, *DAOPHOT - A computer program for crowded-field stellar photometry*, PASP, 99, 191–222
- Sulentic, J. W., 1987, *Properties of dense galaxy groups and the implications of their existence*, ApJ, 322, 605–617
- Sulentic, J. W., Pietsch, W., & Arp, H., 1995, *Diffuse X-ray emission from Stephan's Quintet.*, A&A, 298, 420–426
- Sulentic, J. W. & de Mello Rabaca, D. F., 1993, *Searching for a far-infrared enhancement in compact groups of galaxies*, ApJ, 410, 520–525
- Thompson, L. A. & Gregory, S. A., 1993, *Dwarf galaxies in the Coma cluster*, AJ, 106, 2197–2212
- Tovmassian, H. M. & Chavushyan, V. H., 2000, *Compact Groups: Local Groups?*, AJ, 119, 1687
- Tovmassian, H. M., Martinez, O., & Tiersch, H., 1999, *On the reality of compact groups of galaxies*, A&A, 348, 693
- Trentham, N. & Hodgkin, S., 2002, *The luminosity function of the Virgo Cluster from MB=-22 to -11*, MNRAS, 333, 423–442

- Trentham, N. & Tully, R. B., 2002, *The faint end of the galaxy luminosity function*, MNRAS, 335, 712–732
- Tsvetkov, D. Y. & Bartunov, O. S., 1993, *Sternberg Astronomical Institute supernova catalogue*, Bulletin d'Information du Centre de Donnees Stellaires, 42, 17
- Tully, R. B., Somerville, R. S., Trentham, N., & Verheijen, M. A. W., 2002, *Squelched Galaxies and Dark Halos*, ApJ, 569, 573–581
- Valdes F., 1998, *Guide to the NOAO MOSAIC Data handling software MSCGUIDE*, MSCRED Version 2.0
- Vazdekis, A., Kuntschner, H., Davies, R. L., Arimoto, N., Nakamura, O., & Peletier, R., 2001, *On the Origin of the Color-Magnitude Relation in the Virgo Cluster*, ApJ, 551, L127–L130
- Vennik J., Richter G.M., Longo G., 1993, *The neighbourhoods of the nearest Hickson Grpoups*, Astron. Nachr. Vol 314, 393–397
- Venugopal, V. R., 1995, *Hickson's compact groups of galaxies: far-infrared enhancement*, MNRAS, 277, 455–457
- Verdes-Montenegro, L., Yun, M. S., Williams, B. A., Huchtmeier, W. K., Del Olmo, A., & Perea, J., 2001, *Where is the neutral atomic gas in Hickson groups?*, A&A, 377, 812–826
- Verdes-Montenegro, L. et al., 1997, *CO and FIR Emission in Hickson Compact Groups*, ASP 117, 530
- Vorontsov-Vel'Yaminov, B. A., 1977, *Atlas of interacting galaxies, Part. II and the concept of fragmentation of galaxies.*, A&AS, 28, 1–117
- Walke, D. G. & Mamon, G. A., 1989, *The frequency of chance alignments of galaxies in loose groups*, A&A, 225, 291–302
- White, S. D. M., 1990, *Cosmology - Cooling Flows and Dark Matter*, Nature, 348, 111
- White, S. D. M., Briel, U. G., & Henry, J. P., 1993, *X-ray archaeology in the Coma cluster*, MNRAS, 261, L8–L12
- White, S. D. M. & Rees, M. J., 1978, *Core condensation in heavy halos - A two-stage theory for galaxy formation and clustering*, MNRAS, 183, 341
- Williams, B. A., McMahon, P. M., & van Gorkom, J. H., 1991, *VLA neutral hydrogen imaging of compact groups of galaxies. II - HCG 31, 44, and 79*, AJ, 101, 1957–1968
- Williams, B. A. & van Gorkom, J. H., 1988, *VLA observations of hydrogen in HCG 18*, AJ, 95, 352–355

- Williams, B. A. & Rood, H. J., 1987, *Neutral hydrogen in compact groups of galaxies*, ApJ Suppl., 63, 265–294
- Zabludoff A.I. & Mulchaey J.S., 2000, *The Properties of Poor Groups of Galaxies. III. The Galaxy Luminosity Function*, ApJ, 539, 136–148
- Zabludoff A.I. and Mulchaey J.S., 1998a, *Hierarchical evolution in poor groups of galaxies*, ApJ, 498, L5–L8
- Zabludoff A.I. & Mulchaey J.S., 1998b, *The Properties of Poor Groups of Galaxies. I. Spectroscopic Survey and Results*, ApJ, 496, 39
- Zabludoff, A. I. & Zaritsky, D. 1995, *A Collision of Subclusters in Abell 754*, ApJ, 447, L21
- Zepf, S. E., 1993 *The frequency of mergers in compact groups*, ApJ, 407, 448–455
- Zepf, S. E., de Carvalho, R. R., & Ribeiro, A. L. B., 1997, *The Faint End of the Luminosity Function of Galaxies in Hickson Groups*, ApJ, 488, 11
- Zepf, S. E. & Whitmore, B. C., 1993, *The Structure and Dynamics of Elliptical Galaxies in Compact Groups*, ApJ, 418, 72–81
- Zepf, S. E. & Whitmore, B. C., 1991, *Modeling the evolution of galaxies in compact groups*, ApJ, 383, 542–549

Acknowledgements

At this point I would like to thank my supervisor Prof. R.–J. Dettmar who introduced me to this exciting field of compact galaxy groups and his support. Special thanks to my second supervisor Dr. D. J. Bomans for frequent discussions and his valuable remarks. Cordial thanks to Dr. V. Müller for a constructive collaboration and many discussions. Further I would like to thank Prof. W. Schlosser for giving an overview on galaxy statistics. It is a great pleasure to thank Dipl.–Phys. G. Aronica, Dipl.–Phys. T. Elwert and Dr. T. Kranz for reading the draft version of my thesis and for their very useful suggestions and comments. Many thanks to HD Dr. S. Hüttemeister for acting as the second referent of my PhD thesis.

This thesis was provided by the funding of the Graduiertenkolleg (GK) “Das Magellansche System und andere Zwerggalaxien” of the Universities Bochum and Bonn, which gave me a scholarship from the “Deutsche Forschungs Gemeinschaft” (DFG). Especially I enjoyed several discussions with members of the GK and invited speakers sharing the research interest during the frequent GK meetings.

Finally I would like to thank all people at the Astronomical Institute of the Ruhr–Universität Bochum, who contributed with different kinds of support, discussions, and hints to the success of this thesis.

The research has made use of NASA’s Astrophysics Data System Abstract Service (ADS) and the NASA/IPAC Extragalactic Database (NED), which is operated by the Jet Propulsion Laboratory, California Institute of Technology, under contract with the National Aeronautics and Space Administration.

I acknowledge the use of the Lyon–Meudon extragalactic database (LEDA), through the CISM of the Lyon Claude–Bernard University (<http://leda.univ-lyon1.fr>), the astro–ph preprint archive and the SIMBAD database, operated at CDS, Strasbourg, France. Further, I acknowledge the use of the data reduction software package IRAF, which is written and supported by the IRAF programming group at the National Optical Astronomy Observatories (NOAO) in Tucson, Arizona.

Curriculum Vitae

Personal data:

Day of birth : 02. Dec. 1974
Place of birth : Groß Strehlitz, Upper Silesia
Nationality : German

Education:

1982 – 1985 : primary school: Josef-Schule, Essen
1985 – 1994 : secondary school: Carl-Humann-Gymnasium, Essen
May 1994 : university qualification: Abitur
1994 – 2000 : study of physics at the Ruhr-Universität Bochum
Sep. 1996 : intermediate diploma
Nov. 1998 – Feb. 2000 : diploma thesis at the Ruhr-Universität Bochum
with cooperation of the Infrared Space Observatory (ISO)
team at the Max Planck Institut für Astronomie (Heidelberg)
“ISOPHOT-Kartierungen protostellarer Kondensationen”
(“ISOPHOT-maps of protostellar condensations”)
29. Feb. 2000 : diploma in physics
since April 2000 : PhD student at the Astronomisches Institut of the
Ruhr-Universität Bochum

Employment:

Oct. 1998 – Dec. 1999 : research assistant, Ruhr-Universität Bochum
Apr. 2000 – May 2000 : graduate research assistant, Ruhr-Universität Bochum
June 2000 – Dec. 2002 : member of the Graduate School Bonn/Bochum
“The Magellanic Clouds and Other Dwarf Galaxies”
Jan. 2003 – Mar. 2003 : graduate research assistant, Ruhr-Universität Bochum
Apr. 2003 – Jun. 2003 : member of the Graduate School Bonn/Bochum
Jul. 2003 – Dec. 2003 : scientific assistant,
Rheinische Friedrich-Wilhelms-Universität Bonn

Hiermit versichere ich, daß ich die vorliegende Dissertation eigenständig
und ohne andere als die angegebenen Hilfsmittel angefertigt habe.

Elvira Krusch

Bochum, den 20.10.2003